PONTIFÍCIA UNIVERSIDADE CATÓLICA
DO RIO DE JANEIRO

Leyser Pacheco Pires Filho

Nonlinear Buckling and Vibration Analysis of Pultruded Angle Section Columns

Tese de Doutorado

Thesis presented to the Programa de Pós-graduação em Engenharia Civil of PUC-Rio in partial fulfillment of the requirements for the degree of Doutor em Engenharia Civil.

Advisor: Prof. Paulo Batista Gonçalves

Rio de Janeiro
April 2024

PONTIFÍCIA UNIVERSIDADE CATÓLICA
DO RIO DE JANEIRO

Leyser Pacheco Pires Filho

Nonlinear Buckling and Vibration Analysis of Pultruded Angle Section Columns

Thesis presented to the Programa de Pós-graduação em Engenharia Civil of PUC-Rio in partial fulfillment of the requirements for the degree of Doutor em Engenharia Civil. Approved by the Examination Comittee:

Prof. Paulo Batista Gonçalves
Advisor
Departamento de Engenharia Civil e Ambiental – PUC-Rio

Prof. Zenón José Guzmán Nuñez Del Prado
UFG

Prof. Evandro Parente Junior
UFC

Prof. Alexandre Landesmann
UFRJ

Prof. Jerzy Warminski
LUT

Rio de Janeiro, April 5th, 2024.

Leyser Pacheco Pires Filho

Graduated in Civil Engineering from the Federal University of Goiás in 2015, later earning an M.Sc. in Civil Engineering from the same institution in 2019. Served as a substitute professor at the Federal University of Goiás in the field of Transport Phenomena. Certified as a Safety Engineer from Faculdade de Ipatinga in 2020. Expertise lies in Civil Engineering, particularly in Structural Mechanics.

Bibliographic data

Pires Filho, Leyser Pacheco

Nonlinear Buckling and Vibration Analysis of Pultruded Angle Section Columns / Leyser Pacheco Pires Filho; advisor: Paulo Batista Gonçalves. – Rio de Janeiro: PUC-Rio, Departamento de Engenharia Civil e Ambiental, 2024.

179 f.: il. (color); 29,7 cm

1. Tese (doutorado) – Pontifícia Universidade Católica do Rio de Janeiro, Departamento de Engenharia Civil e Ambiental, 2024.

Inclui referências bibliográficas.

1. Engenharia Civil – Dissertações. 2. Dinâmica não linear. 3. Vibrações não lineares. 4. Instabilidade dinâmica. 5. Efeito de excitações harmônicas axiais. 6. Acoplamento flexão-torção. I. Gonçalves, Paulo Batista. II. Pontifícia Universidade Católica do Rio de Janeiro. Departamento de Engenharia Civil. III. Título.

To my parents, Lúcia and Leyser, for their unwavering support
and endless encouragement.

Acknowledgements

To God for empowering me.

To Professor Paulo for his attention, trust, enormous dedication, and availability in teaching, explaining, listening, and advising me. I am eternally grateful.

To my initial mentors, especially Prof. Frederico M. A. da Silva and Zenón J. G. N. del Prado, for introducing me to research.

To the PUC-Rio institution for the opportunity.

To the Brazilian Navy for their assistance.

This study was financed in part by the Coordenação de Aperfeiçoamento de Pessoal de Nível Superior - Brasil (CAPES) - Finance Code 001.

Abstract

Pires Filho, Leyser Pacheco; Gonçalves, Paulo Batista (Advisor). **Nonlinear Buckling and Vibration Analysis of Pultruded Angle Section Columns**. Rio de Janeiro, 2024. 179p. Tese de Doutorado - Departamento de Engenharia Civil e Ambiental, Pontifícia Universidade Católica do Rio de Janeiro.

Thin-walled elements with open cross sections have been widely employed in engineering applications. While conventional applications and design codes predominantly focus on steel members, a growing interest has emerged in exploring alternative materials, particularly composites. Among these, fiber reinforced polymer (FRP) has witnessed increased application owing to its advantageous properties. However, the orthotropic nature of FRP columns, produced through pultrusion, presents a challenge as conventional design prescriptions for structural steel cannot be directly applied. Thus, further research is essential to derive reliable design rules for FRP members. In the realm of traditional open section geometries, angle sections have been commonly employed. Despite their geometric simplicity, angles exhibit a complex structural buckling and dynamic behaviour which arises from the fact that such columns may undergo different deformation modes, according to their geometric and material properties, with modal interaction observed, particularly between flexural and torsional modes. This work focuses on investigating the buckling and vibration characteristics of pultruded FRP angle sections, encompassing both equal and unequal-leg sections, and spanning short to long columns. For this, reduced order models (ROMs) are developed based on the classical von Kármán nonlinear plate theory (CPT). The angle section is modelled as two plates, with continuity constraints considered at the common boundary. Utilizing GBTul software, a comprehensive investigation of modal participation in linear buckling and vibration modes is conducted. Based on this analysis, the plate displacement field for each ROM is approximated by suitable analytically derived interpolating functions, which are used to discretize the continuous system on the basis of the Ritz energy method. By application of Hamilton's principle, the eigenvalue problems and nonlinear equations of motion are derived. Parametric dimensional and nondimensional analyses are carried out, with critical loads and

vibration frequencies compared favorably with GBTul results. Post-buckling paths are explored by solving the systems of nonlinear equilibrium equations for each ROM. The influence of geometric and material parameters on post-buckling stiffness is investigated, along with the sensitivity to initial geometrical imperfections. Finally, the stability of the columns under harmonic axial loading is assessed by numerically solving the nonlinear equations of motion using the fourth-order Runge-Kutta method. Parametric instability regions are determined as a function of the frequency and magnitude of the harmonic excitation force, considering the influence of material, damping, and cross-sectional geometry. Bifurcation diagrams are obtained employing the brute force method and continuation techniques, clarifying the bifurcations associated to the parametric instability boundaries. The evolution of basins of attraction of coexisting solutions is investigated, providing an evaluation of dynamic integrity. The results demonstrate that the column may lose stability at load levels well below the static buckling loads and, therefore, designers must exercise caution when working with these structures subjected to time-varying axial loads.

Keywords

Reduced-order models; buckling; vibration; pultruded FRP; angle section.

Resumo

Pires Filho, Leyser Pacheco; Gonçalves, Paulo Batista. **Análise Não Linear de Flambagem e Vibrações de Perfis Pultrudados de Seção Cantoneira**. Rio de Janeiro, 2024. 179p. Tese de Doutorado - Departamento de Engenharia Civil e Ambiental, Pontifícia Universidade Católica do Rio de Janeiro.

Elementos de paredes finas com seções transversais abertas têm sido amplamente empregados em aplicações de engenharia. Embora as aplicações convencionais e os códigos de projeto se concentrem predominantemente em elementos de aço, observa-se um interesse crescente no uso de materiais alternativos, especialmente compósitos. Entre estes, polímeros reforçados com fibra (FRP) têm sido cada vez mais empregados devido às suas propriedades benéficas. No entanto, a natureza ortotrópica das colunas FRP, produzidas através de pultrusão, apresenta um desafio, uma vez que as prescrições convencionais de projeto para estruturas de aço não podem ser aplicadas diretamente. Assim, mais pesquisas são essenciais para fornecer normas de projeto confiáveis para membros estruturais em FRP. Entre as geometrias tradicionais de seção aberta, seções cantoneira têm sido comumente empregadas. Apesar de sua simplicidade geométrica, colunas com seção cantoneira apresentam uma flambagem estrutural e um comportamento dinâmico complexos, que decorre do fato de tais colunas apresentarem diferentes modos de deformação, função de suas propriedades geométricas e materiais, incluindo interação modal, principalmente entre os modos de flexão e torção. Este trabalho se concentra na investigação das características de flambagem e vibração de colunas pultrudadas FRP com seção cantoneira, abrangendo seções de abas iguais e desiguais, e abrangendo colunas curtas a longas. Para isso, são desenvolvidos modelos de dimensão reduzida (ROMs) baseados na teoria clássica não linear de placas (CPT) proposta por von Kármán. A seção cantoneira é modelada como duas placas, com restrições de continuidade imposta na ligação entre ambas. Utilizando o software GBTul, é conduzida uma investigação abrangente da participação modal nos modos de flambagem e vibração. Com base nesta análise, o campo de deslocamentos de cada placa para todos os ROMs é aproximado por funções de interpolação derivadas analiticamente,

que são usadas para discretizar o sistema contínuo com base no método de Ritz. Pela aplicação do princípio de Hamilton, os problemas de autovalor e equações não lineares de movimento são derivados. São realizadas análises paramétricas dimensionais e adimensionais, com cargas críticas e frequências de vibração comparadas favoravelmente com os resultados do GBTul. Caminhos pós-flambagem são explorados resolvendo-se os sistemas de equações de equilíbrio não lineares para cada ROM. A influência dos parâmetros geométricos e materiais na rigidez pós-flambagem é investigada, juntamente com a sensibilidade às imperfeições geométricas iniciais. Finalmente, a estabilidade de colunas sob carregamento axial harmônico é avaliada resolvendo-se numericamente as equações não lineares de movimento usando-se o método Runge-Kutta de quarta ordem. As regiões de instabilidade paramétrica são determinadas em função da frequência e magnitude da força de excitação harmônica, considerando a influência do material, do amortecimento e da geometria da seção transversal. Os diagramas de bifurcação são obtidos empregando-se o método da força bruta e técnicas de continuação, esclarecendo as bifurcações associadas aos limites de instabilidade paramétrica. A evolução das bacias de atração de soluções coexistentes é investigada, proporcionando uma avaliação da integridade dinâmica. Os resultados demonstram que a coluna pode perder estabilidade sob níveis de carga bem abaixo da carga estática de flambagem e, portanto, os projetistas devem ter cautela ao trabalhar com essas estruturas sujeitas a cargas axiais variáveis no tempo.

Palavras-chave

Modelos de dimensão reduzida; flambagem; vibração; colunas pultrudadas FRP; seção cantoneira.

Table of contents

List of figures

List of tables

List of symbols

ROMAN SYMBOLS

A_{ij}	Plate membrane stiffness coefficients related to force resultants
b	Plate's width in equal-leg angle sections
b_1	Plate's width of the longer leg in unequal-leg angle sections
b_2	Plate's width of the shorter leg in unequal-leg angle sections
c	Cosine of α
$\bar{c}$	Damping coefficient
C_i	Modal amplitude
C_1	Axial modal amplitude due to minor-axis bending
C_2	Flexural modal amplitude due to minor-axis bending
C_3	Axial modal amplitude due to major-axis bending
C_4	Flexural modal amplitude due to major-axis bending
C_5	Torsional modal amplitude
C_6	Axial modal amplitude due to torsion
C_7	In-plane modal amplitude in the y direction due to torsion
$\mathbf{C}$	Displacement vector
d_y	Distance between the geometric and shear centers on the $\bar{y}$ axis
d_z	Distance between the geometric and shear centers on the $\bar{z}$ axis
D_{ij}	Plate bending stiffness coefficients related to moment resultants
E_f	Young's modulus of the fiber
E_m	Young's modulus of the matrix
E_1	Young's modulus of the composite in the fiber direction
E_2	Young's modulus of the composite transversal to the fiber direction
$f(y)$	Shape function in the y direction
$g(x)$	Shape function in the x direction
G_f	Shear modulus of the fiber

G_m	Shear modulus of the matrix
G_{12}	Shear modulus in the 1-2 plane
I_y	Moment of inertia about the *Y* global axis
I_z	Moment of inertia about the *Z* global axis
I_{yz}	Product of inertia
K_t	Torsional stiffness coefficient
K_{Gt}	Torsional geometric coefficient
$\mathbf{K}$	Stiffness matrix
$\mathbf{K_G}$	Geometric matrix
L	Angle section
L	Column length
L_g	Lagragian of the system
L_t	Modal participation transition length
m	Number of half-waves in the longitudinal direction
mb	Minor-axis bending
Mb	Major-axis bending
M_x	Flexural moment resultant per unit length in *x* direction
M_y	Flexural moment resultant per unit length in *y* direction
M_{xy}	Torsional moment resultant per unit length in *xy* direction
M_t	Torsional mass coefficient
$\mathbf{M}$	Mass matrix
n_d	Number of deformation modes
N_x	Distributed load per unit length
$\bar{N}$	Harmonic axial excitation
N_{cr}	Critical load per unit length
N_x	Normal in-plane force resultant per unit length in *x* direction
N_y	Normal in-plane force resultant per unit length in *y* direction
N_{xy}	Shear in-plane force resultant per unit length in *xy* direction
P_k	Modal participation factor

P_{cr} Critical load

$\bar{Q}$ Nondimensional axial excitation

Q_{ij} Stiffness coefficient in the direction *ij*

Q_x Shear force resultant per unit length in *x* direction

Q_y Shear force resultant per unit length in *y* direction

s Sine of α

t Plate's thickness

t_1 Plate's thickness of the longer leg

t_2 Plate's thickness of the shorter leg

$\bar{t}$ Time

T Periodicity of solution

T Kinetic energy of the plate

T_s Solution period

$\bar{u}$ In-plane displacement component in the *x* direction of an arbitrary point

u In-plane displacement component in the *x* direction of the middle surface

$u_{mb}^{(i)}$ Axial displacement of plate *i* due to minor-axis bending

$u_{Mb}^{(i)}$ Axial displacement of plate *i* due to major-axis bending

$u_t^{(i)}$ Axial displacement of plate *i* due to torsion

U Strain energy of the plate

U_0 Fundamental displacement field

U_1 Incremental displacement field

$\bar{v}$ In-plane displacement component in the *y* direction of an arbitrary point

v In-plane displacement component in the *y* direction of the middle surface

$v_{mb}^{(i)}$ In-plane displacement in the *y* direction of plate *i* due to minor-axis bending

$v_{Mb}^{(i)}$ In-plane displacement in the *y* direction of plate *i* due to major-axis bending

$v_t^{(i)}$ In-plane displacement in the *y* direction of plate *i* due to torsion

V Potential energy of the applied loads

$\bar{w}$	Transversal displacement component in the *z* direction of an arbitrary point
w	Transversal displacement component in the *z* direction of the mid-surface
w_0	Transversal imperfection function
$w_{,x}$	Rotation of the section about the *x*-axis
$w_{,y}$	Rotation of the section about the *y*-axis
$w_{mb}^{(i)}$	Transversal displacement of plate *i* due to minor-axis bending
$w_{Mb}^{(i)}$	Transversal displacement of plate *i* due to major-axis bending
$w_t^{(i)}$	Transversal displacement of plate *i* due to torsion
W_{nc}	Non-conservative work done by a frictional force
V_f	Volumetric fractions of fibers
V_m	Volumetric fractions of matrix
x	Coordinate in the longitudinal direction of the plate
y	Coordinate in the transversal direction of the plate
y'	Coordinate in the minor principal axis of the cross-section
$\bar{y}$	Auxiliary axis parallel to the minor principal axis
y_{cg}	Geometric center coordinate in the *y* direction
y_1	Local coordinate axis along the width of plate 1
y_2	Local coordinate axis along the width of plate 2
z	Coordinate in the normal direction of the plate
z'	Coordinate in the major principal axis of the cross-section
$\bar{z}$	Auxiliary axis parallel to the major principal axis
z_{cg}	Geometric center coordinate in the *z* direction

GREEK SYMBOLS

α	Orientation angle of the principal axes of the cross section
β	Aspect ratio for the angle section legs
γ_{ij}	Shear strain in the direction *ij*

γ_{xy}	Shear strain component in the plate middle-surface and *xy* direction
Γ	Nondimensional applied load
Γ_{cr}	Nondimensional critical load
δ	Nondimensional frequency load ratio
δ_n	Free vibration frequency ratio
ε_{ii}	Longitudinal strain in the direction *i*
ε_x	Normal strain component in the plate middle-surface and *x* direction
ε_y	Normal strain component in the plate middle-surface and *y* direction
ζ_k	Admissible function for displacement components
$\zeta_{mb}^{(i)}$	Displacement field for plate *i* due to minor axis bending
$\zeta_{Mb}^{(i)}$	Displacement field for plate *i* due to major axis bending
$\zeta_t^{(i)}$	Displacement field for plate *i* due to torsion
η	Transversal to longitudinal Young's moduli ratio
θ	Section rotation about the shear center
κ_x	Curvature in *x* direction
κ_y	Curvature in *y* direction
κ_{xy}	Section twist
λ	Nondimensional axial load parameter
ν	Poisson's ratio for isotropic material
ν_f	Poisson's ratios of the fiber material
ν_m	Poisson's ratios of the matrix material
ν_{12}	Poisson's ratio in the 1-2 direction of the composite
ν_{21}	Poisson's ratio in the 2-1 direction of the composite
ξ	Thickness to shorter leg width ratio
Ξ	Linear viscous damping parameter
Π	Total potential energy of the system
ρ	Material density
σ_{ii}	Normal stress in the *i* direction

$\bar{\sigma}_x$	Normal stress component in the *x* direction
$\bar{\sigma}_y$	Normal stress component in the *y* direction
τ_{ii}	Shear stress in the direction *ij*
$\bar{\tau}_{xy}$	Shear stress component in the *xy* direction
τ	Dimensionless time
υ_{Xn}	Admissible functions for plates in the *x* direction
υ_{Yn}	Admissible functions for plates in the *y* direction
φ	Wider plate aspect ratio
φ_t	Modal transition aspect ratio
φ_k	Longitudinal function in the *x* direction
ψ	Nondimensional material parameter
ω	Forcing frequency
ω_0	Lowest natural frequency
ω_n	Nonlinear amplitude dependent frequency
Ω	Nondimensional forcing frequency parameter
Ω_0	Fundamental frequency parameter

Persistence is the road to accomplishment.

Charlie Chaplin

1
Introduction

In this chapter, a concise literature review covering topics of interest for the development of this research is provided. Additionally, the general and specific objectives are outlined, along with the contents of the subsequent chapters.

1.1
Initial considerations

The essential role of a sound engineering design conception is to obtain an economically viable and at the same time safe structure. With the evolution of construction technology, engineers are designing structures that are progressively lighter, requiring increasingly accurate studies of their static and dynamic behavior to ensure stability and acceptable vibration levels. Within this context, the static and dynamic analysis of slender structures become indispensable for the development of viable structures. However, the behavior of these slender structures has becoming increasingly complex due to the increasing role played by geometric nonlinearities.

Among these structures are metal (usually steel) bars with open thin-walled cross-sections, leading to lighter structures. In addition, due to advances in material sciences, some new materials have shown to be an economically viable alternative to steel, such as composites. The use of composites in engineering applications, as an increasingly favored alternative to metal structures, has shown significant growth in recent years (Maji et al., 1997; Kar, 2016). Among composite materials, fiber-reinforced polymer (FRP) thin-walled members have gained widespread acceptance across various sectors, including civil, aeronautical, naval, mechanical, and offshore engineering (Vedernikov et al., 2020). They offer several advantageous properties such as a high load-capacity to weight ratio, corrosion resistance, durability even in harsh environments, nonconductive attributes, extended fatigue life, design flexibility, and reasonable cost. They can thus be used

as substitutes to conventional materials, particularly in the construction industry. Apart from their use as secondary components such as handrails, floor gratings, cable trays, FRP profiles can also be employed in building structures, pedestrian bridges, communication towers, mining towers and cooling towers, as illustrated in Figure 1.1. Despite their advantages, FRP thin-walled members present certain limitations such as brittle and non-ductile behavior, poor long-term temperature resistance, aging phenomena, and low interlaminar shear strength. Efforts to address these limitations have been made in recent years, including the development of more resistant resins and coupling agents.

(a) Eyecatcher building, Basel, 1998 (Source: Correia et al., 2015).

(b) Counterflow Cooling Tower (Source: ipfonline.com, accessed on Feb 16, 2024).

Figure 1.1 - Applications of FRP profiles.

Although FRP can be manufactured using different methods, pultrusion is the preferred method for manufacturing FRP due to its cost-effectiveness, energy efficiency, and minimal waste production (Volk et al., 2022; Minchenkov et al., 2021). It is obtained by pulling resin-impregnated fibers through a heated die for continuous shape fabrication (Clarke, 2014). Pultruded FRP profiles exhibit orthotropic properties, with superior material characteristics along the fiber direction. Most thin-walled FRP columns have open cross-sections, offering versatility in shape due to ease of manufacturing and application. The pultrusion process will be explained in more detail in the following chapter.

A drawback of open sections is their reduced torsional stiffness compared to closed sections, making them more prone to torsional buckling failure (Allen &

Bulson, 1980; Pignataro et al., 1991; Trahair, 1993; Alam et al., 2019). These structural members may exhibit qualitatively different buckling and vibration modes depending on their geometry and material. These modes can interact due to nonlinear modal coupling, resulting in complex nonlinear behavior, including interactive buckling, sensitivity to imperfections, and reduced load capacity (Gioncu, 1994; Hancock, 2018; Dubina & Ungureanu, 2023). Therefore, understanding the behavior of thin-walled open cross-section columns in response to potential failure modes and unwanted vibrations is essential for optimizing their use.

Various theories have been employed to analyze the buckling behavior of thin-walled members. While many studies rely on classical Vlasov theory (Vlasov, 1963) or its modified versions (Attard, 1986; Ambrosini et al., 2000; Piccardo at al., 2017; Mohri et al., 2001) to investigate global behavior, consistent results are also obtained by modeling profiles as assemblies of plates. This approach allows for the study of both local and global buckling modes using appropriate plate theories (Qiao et al., 2001; Coaquira et al., 2021). A powerful numerical tool for analyzing the structural behavior of thin-walled members is the Generalized Beam Theory (GBT) proposed by Schardt (1994). Building upon this theory, researchers at IST-Lisbon developed the GBTul software (Bebiano et al., 2018; Gonçalves et al., 2010; Bebiano et al., 2015; Gonçalves et al., 2023), which expresses cross-section displacements as a combination of significant local and global deformation modes. The software conducts elastic buckling and vibration analyses, facilitating the identification of meaningful cross-section deformation modes through a modal participation analysis (Bebiano et al., 2018). Silvestre and Camotim (2002a, b) applied the GBT to analyze the structural behavior of thin-walled composite members, including FRP profiles. GBTul serves as an efficient alternative to other numerical methods like finite strip and shell finite element methods, and it is employed here as a benchmark for the proposed reduced-order models (ROM).

Among open section profiles, angle sections are notable for their geometric simplicity and ease of fabrication, making them a common choice in many systems in the building industry. However, despite their simplicity, angles can exhibit complex structural behavior under compression forces. Slender cross-sections, in particular, are highly susceptible to various buckling modes, ranging from local to

global. Additionally, their behavior is influenced by the width of each leg, with current research typically focusing on the more common equal-leg sections. Although unequal-leg angles may offer greater efficiency in certain cases, their behavior has received considerably less attention compared to equal-leg angles (Liu & Chantel, 2011; Bai et al., 2018). Figure 1.2 shows angle section profiles made of pultruded FRP material applied as lateral bracing.

Figure 1.2 - Application of pultruded FRP angle section profiles as lateral bracing (Source: fiberline.com/design-manual, accessed on Feb 20, 2024).

1.2 Brief literature review

The linear and nonlinear buckling behavior of angle columns has been extensively studied, with research spanning numerical, experimental, and design aspects. Recent works provide comprehensive literature reviews on this topic (Zhang et al., 2021; Diniz et al., 2023; Laracuente, 2024). These contributions show that the buckling (or vibration) modes of angle columns can generally be described by a combination of local, flexural, and torsional modes. They underscore the significant role of torsional modes in members spanning from very short to intermediate lengths, while minor axis bending predominates for longer profiles.

Equal-leg and unequal-leg sections exhibit distinct buckling behaviors, as shown hereafter. In the case of an unequal-leg angle member, the torsional component is characterized by the cross-section rotation about the shear center, which does not coincide with either of the principal bending axes (Ádány & Dávid, 2012). Allen and Bulson (1980) demonstrated that weak and strong-axis flexural displacements may occur simultaneously with torsional displacements, resulting in

a flexural-torsional buckling mode with biaxial bending. Both scenarios are examined here, and the impact of the width ratio on the buckling and vibration behavior is investigated.

While many of the aforementioned contributions focus on steel structures, recent years have seen increased attention given to the study of stainless-steel angle sections. This heightened interest is attributed to their superior corrosion resistance, durability, high material strength, and exceptional ductility (Gardner, 2019; Sun et al., 2019; Sarquis et al., 2020; Behzadi-Sofiani (2023). Additionally, investigations into the buckling behavior of aluminum alloy columns have been undertaken (Zhang et al., 2021; Pham et al., 2021). One key aspect in these cases is the inherent material nonlinearity. However, comparatively less research has been conducted on composite elements, including FRP angle profiles. Silva et al. (2010) developed a GBT formulation for the buckling analysis of FRP composite open-section thin-walled columns. In the realm of experimental studies, recent research on the buckling of pultruded FRP angle section profiles has shed light on significant aspects of their buckling behavior. Cardoso & Togashi (2018) conducted a detailed experimental investigation into the flexural-torsional buckling of pultruded GFRP angle columns. Their findings revealed that, for short to intermediate lengths, flexural-torsional buckling governs the behavior, with torsional participation decreasing and flexural participation about the major axis increasing as length increases. For longer members, buckling is primarily governed by flexure about the minor axis, with negligible transversal wall bending within the studied length range. Additionally, they observed the predominance of torsion about the shear center in the buckling behavior and noted a significant post-buckling reserve of strength, similar to that observed in a plate. Thumrongvut et al. (2020) studied experimentally the flexural-torsional buckling of pultruded angle beams under eccentric loading. Sirajudeen & Sekar (2020) also explored the vulnerability of pultruded GFRP angle sections to torsion-related buckling experimentally. Recently, Diniz et al. (2023) applied the direct strength approach to predict the strength of pultruded GFRP angle columns.

A literature survey reveals a shortage of information on the post-buckling behavior of angle sections, particularly FRP pultruded profiles. Although linear analyses of these profiles have demonstrated complex behavior with coupled

flexural-torsional modes and abrupt changes in modal participation, there remains a gap in understanding their post-buckling characteristics. Dinis et al. (2012) conducted a comprehensive numerical investigation into the mechanics underlying the buckling and, predominantly, the post-buckling behavior of short-to-intermediate equal-leg thin-walled angle steel columns with clamped and pinned ends, employing ABAQUS (Simulia, 2024) shell finite element analyses. Their findings revealed a variation in post-buckling strength reserve from relatively high (for shorter lengths) to considerably low (for longer lengths), with the magnitude of corner flexural displacements playing a pivotal role in distinguishing between different post-buckling behaviors. Later, Mesacasa et al. (2014) carried out an in-depth numerical investigation on the effects of modal interaction and initial imperfections on the post-buckling behavior, ultimate strength, and failure mode of fixed-ended and pin-ended thin-walled equal-leg angle columns using ANSYS (Ansys, 2024) shell finite element analysis. Shifferaw & Schafer (2014) demonstrated, through a combination of existing experiments and elastic buckling analysis, that plain and lipped angles with fixed ends exhibit stable post-buckling behavior concerning torsional-flexural buckling modes, a phenomenon overlooked, according to the authors, in current design methods for cold-formed steel angles. Banat et al. (2016) explored the buckling and post-buckling behavior of Z-shaped and channel section thin-walled fiber metal laminate profiles subjected to axial loading, both demonstrating stable post-buckling behavior. Landesmann et al. (2017) conducted an experimental investigation and numerical simulations of short-to-intermediate slender pin-ended cold-formed steel equal-leg angle columns. In addition, Sarquis et al. (2020) and Sirqueira et al. (2020), among others, conducted experimental and numerical investigations on hot-rolled stainless-steel equal-leg angles under compression.

No analytical studies were found regarding the post-buckling behavior of FRP angle sections, though reliable experimental findings are available. Monteiro & Malite (2021) investigated the behavior of eccentrically loaded pultruded GFRP angle columns of varying lengths. They observed typical load vs. displacement curves demonstrating either flexural or flexural-torsional buckling modes. Some specimens exhibited loading paths characterized by significant displacements followed by relatively flat post-buckling behavior. Others displayed exceptional post-buckling strength reserve, consistent with findings by Cardoso & Togashi

(2018). Balagopal et al. (2020) experimentally examined concentrically loaded GFRP angle sections with bolted connections in communication towers. They determined material properties through compression and in-plane shear coupon tests and developed a mathematical model to predict buckling characteristics such as torsional-flexural, flexural, and pure torsion. The proposed formulation was validated using experimental tests across various slenderness ratios and numerical simulations with ANSYS finite element software, revealing stable post-buckling behavior. FRP columns with various cross-sections have been the subject of both experimental and numerical investigations. Barbero & Trovillion (1998) examined the post-buckling behavior of fiber-reinforced composite wide-flange I-section columns. Urbaniak et al. (2015) conducted experimental and numerical analyses to assess the influence of boundary conditions on the critical load, post-buckling behavior, and failure load of compressed composite channel-section columns. Rozylo et al. (2017) investigated the critical and post-buckling states of thin-walled carbon/epoxy laminate profiles with top-hat sections under compression, observing limited post-buckling strength. D'Aguiar & Parente Junior investigated the local buckling and post-critical behavior of thin-walled composite channel section columns, including geometric imperfections and material failure, as well as approximate analytical solutions based on the classical lamination theory. Additionally, Cintra et al. (2019) conducted numerical and experimental investigations into the parameters affecting the local buckling response of pultruded GFRP I-columns. These studies underscored the significant influence of material constitutive laws on buckling phenomena. Despite these efforts, the buckling behavior of angle section beams and columns continues to present challenges, with current design provisions in international standards known to have significant limitations, particularly in the case of pultruded FRP profiles (Dinis & Camotim, 2015; Behzadi-Sofiani et al., 2021, 2022, 2023; CEN/TS 19101, 2022; CNR, 2008). This underlines the need for further research in this area.

While angle sections are frequently subjected to dynamic loads in various applications such as transmission towers (Vayas et al., 2021; Hadane et al., 2023), pedestrian bridges (Szak et al., 1999; Wei et al., 2019), trusses, and bracing systems in buildings and bridges, their dynamic properties have received limited attention (Slater, 1969; Hasan & Barr, 1974; Krishnan & Singh, (1991), Bebiano et al., 2008a; Bebiano et al., 2008b, Prokić, 2010), particularly in the case of FRP profiles

(Boscato & Russo, 2009; Gaspar & Cardoso, 2023). Evaluating their natural frequencies and mode shapes represents the initial step in dynamic design or verification procedures. Therefore, this study offers a comprehensive analysis of the natural frequencies and dominant vibration modes of FRP profiles, highlighting the potential coupling of different motions, notably the coupling of bending and torsional motions. In addition, the distinctions and similarities with buckling modes are elucidated.

Numerous studies have investigated the dynamic instability of axially loaded metal and composite thin-walled columns under harmonic or pulse loads (Pavlović et al., 2007; Machado et al., 2007; Teter, 2010; Kubiak, 2011; Yadav et al., 2017). However, the majority of contributions, even in recent years, focus solely on determining critical excitation frequencies/loads that cause parametric instability, while only a few works are found regarding the nonlinear behavior of these structures (Mancilla et al., 2015; Coaquira et al., 2016; Carvalho et al., 2017). The nonlinear dynamic response and parametric instability of short to medium length FRP channel section columns under harmonic axial forcing are investigated by Coaquira et al. (2021). The authors demonstrate that the column can lose stability at load levels well below the static buckling load. Later, a parametric analysis conducted by Coaquira et al. (2022) has shown how the material characteristics and geometric properties of a long FRP column influence its nonlinear vibrations and dynamic instability. These works are among the few found in the literature that deal with nonlinear vibrations and bifurcations of FRP columns and, to the authors' knowledge, no previous study has been conducted on the parametric instability of FRP pultruded angle columns subjected to axial excitation.

In recent years, there has been a growing interest on deriving meaningful reduced-order models (ROMs), also known as low-dimensional models, for the analysis of buckling and vibration of structures (Wang et al., 2017; Liang et al., 2020; Magisano & Garcea, 2022). These models are essential, particularly in nonlinear problems, as they enable the efficient use of numerical tools for nonlinear structural analysis (Coaquira et al., 2021; Coaquira, 2020; Mazzilli et al., 2022). While general finite element software or specialized software for both open and closed section profiles (Bebiano et al., 2018; Schafer, 2020; Nguyen et al., 2015) can often be effective, ROMs serve as valuable tools for gaining deeper insights

into the influence of material and geometric parameters on structural behavior. Furthermore, they aid in the development of explicit formulas to support design rules and recommendations (Ascione et al., 2016; Cardoso et al., 2014; Cardoso et al., 2017).

Depending on the fibers' distribution, composite materials may display more than one stable equilibrium configuration without damage. This behavior has given rise to a new research area on multistable structural systems, with applications in vibration control, energy harvesting, microelectromechanical systems (MEMS), robotics, energy absorbers, morphing structures and programmable devices as well as metamaterials (Hu & Burgueño, 2015; Fang et al., 2022; de Castro et al., 2023; Mitura et al., 2024).

In this work, reduced-order models (ROMs) based on the nonlinear von Kármán classical plate theory (CPT) are proposed for analyzing the linear and nonlinear buckling and vibration of equal and unequal-leg FRP pultruded angle section columns. These ROMs enable analysis across a range of defined parameters, elucidating the dominant regions for each buckling/vibration phenomenon. To achieve this, consistent expressions for in-plane and transverse displacements are geometrically derived for each plate of the angle. The two plates are assumed as simply supported at the two ends of the column. The Ritz method is applied to discretize the continuous system and a set of coupled ordinary equations of motion are obtained by means of the Hamilton's principle, which are numerically solved by the Runge-Kutta fourth-order method. The eigenvalue problems allow for the determination of critical loads and natural frequencies of the FRP columns. The resulting eigenvalues and eigenvectors are compared with those obtained from GBTul (Bebiano et al., 2008a; Bebiano et al., 2008c; Bebiano et al., 2018), utilized here as a benchmark. Numerical results for the post-buckling paths, parametric instability regions, frequency-amplitude relations, bifurcation diagrams, and basins of attraction of FRP pultruded angle columns are presented, and the influence of geometric and material parameters is clarified by the proposed consistent ROMs.

1.3
Motivation

This thesis is part of the research line on Stability and Dynamics of Structures of the Department of Civil and Environmental Engineering, PUC-RIO, which analyzes the loss of static and dynamic stability and non-linear vibrations of slender structures. It is part of the research projects on thin-walled open-section bars and composite structures (Carvalho, 2013; Mancilla, 2014; Coaquira, 2016; Coaquira, 2020).

Angle section profiles find applications in various engineering fields. Despite being relatively simple and commonly used structural elements, the literature lacks studies on the buckling and vibrations of these elements, particularly when made of pultruded FRP materials. Therefore, this work aims to broaden our understanding of these elements in aspects that have not yet been explored.

1.4
Objectives

The aim of this study is to offer a comprehensive understanding of the linear and nonlinear buckling and vibration behavior exhibited by pultruded FRP angle section columns, serving as a valuable reference point for future experimental and theoretical advancements, along with informing design considerations.

Highlights of this work are:

- Buckling and vibration analysis of composite FRP angles employing a nonlinear plate theory;
- Identification of the modal participation in the buckling and vibration modes and possible modal interaction of FRP equal- and unequal-leg angle sections, covering short to long columns;
- Derivation of reduced order models (ROMs) covering the typical buckling phenomena of FRP columns and expected modal interaction. For this the displacement field of the two plates are analytically derived, enabling the use of the Ritz method;

- Investigation, based on the developed ROMs, of the influence of geometric and material parameters on the nonlinear buckling and vibration response of angle section profiles, particularly on post-buckling paths, nonlinear dynamic response, and parametric instability boundaries.

1.5 Scope of the thesis

This thesis is divided into eight chapters, as listed and described below:

- Chapter 2 summarizes the characteristics of composite materials, specially pultruded materials, outlining the typical properties and constitutive relations of these materials. A standard pultruded material is selected for the analyses in the subsequent chapters, based on existing literature and experimental results;
- Chapter 3 presents the von Kármán nonlinear classical plate theory (CPT) and derives the total potential energy functional of the angle profile considered as an assembly of two plates;
- Chapter 4 presents the analytical development of the displacement fields for the predominant deformation modes of a general angle section profile, enabling the derivation of reduced-order models (ROMs) for buckling and vibration analysis by means of the Ritz method;
- Chapter 5 focuses on the linear buckling and vibration analysis of pultruded FRP angle section profiles, clarifying the influence of geometric and material parameters on critical loads and natural frequencies;
- Chapter 6 investigates the post-buckling behavior of axially loaded pultruded FRP angle section profiles. The nonlinear equilibrium equations for each ROM are solved to determine the post-buckling paths. Also, the sensitivity of the solutions to initial geometric imperfections is explored;
- Chapter 7 presents the dynamic stability analysis of the pultruded column under harmonic axial loading. The parametric instability boundaries as a function of the frequency and magnitude of the excitation force are

determined. The bifurcations associated with these boundaries are explored and the evolution of the basins of attraction of coexisting solutions is analyzed;

- Finally, in Chapter 8, conclusions and suggestions for future work are presented.

2
Pultruded Materials

In this chapter, the characteristics of composite materials are addressed, with a focus on pultruded materials. The typical properties of these materials, as well as their constitutive relation, are presented. Finally, based on the literature, a standard pultruded material is adopted for the analyses to be carried out in the following chapters.

2.1
Types of composites

The properties of composite materials are intricately linked to their constituent phases, the proportions of these phases, and the geometric attributes of the dispersed phase. This dispersion is defined by the shape and size of the reinforcing elements, their distribution and orientation within the composite structure. Figure 2.1 illustrates a comprehensive classification scheme for various types of composite materials, encompassing four primary divisions: particle-reinforced, fiber-reinforced, structural, and nanocomposites (Callister & Rethwisch, 2013).

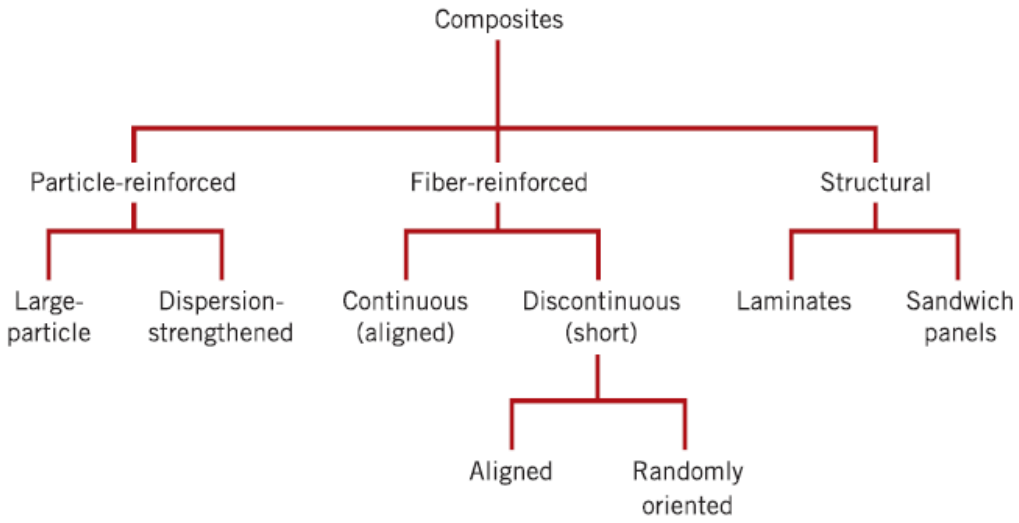

Figure 2.1 - Classification scheme for types of composites (Callister & Rethwisch, 2013).

The dispersed phase in particle-reinforced composites is equiaxial, indicating that the particle dimensions are roughly equal in all directions. In this type of composite, the particles may assume a significant size, leading to an interaction between the particle and matrix that is better addressed through continuum mechanics rather than molecular considerations. This scenario is exemplified by materials like concrete. Alternatively, these particles can contribute to reinforcement through a uniform dispersion mechanism.

In fiber-reinforced composites, the dispersed phase comprises elements with a fibrous geometry - thin and elongated structures characterized by a high length-to-diameter ratio. As illustrated in Figure 2.1, these composites are further categorized into continuous, where fibers align seamlessly along the longitudinal direction without interruption, and discontinuous, where fibers are segmented (cut), with the possibility of being aligned or randomly oriented. The concentration and distribution of fibers within the continuous phase, along with their relative orientation, are pivotal factors that significantly influence the overall strength of composite materials.

Structural composites represent multilayered materials characterized by their typically low density, designed for applications demanding both structural integrity and exceptional strength and stiffness against diverse stressors. The properties of these composites are influenced not only by the inherent characteristics of their constituent materials but also by the geometric arrangement of the different layers.

Laminated composites and sandwich panels stand out as the predominant types within the realm of structural composites.

Nanocomposites, on the other hand, are composite materials wherein the dispersed phase is comprised of nanoscale particles (≤ 100 nm). Engineered with precision, these materials are designed to exhibit superior properties compared to conventional counterparts, including enhanced magnetic, optical, and thermal characteristics.

2.2
Pultruded profiles

Pultrusion is an automated manufacturing process employed for the production of continuous fiber composite components featuring a consistent cross-sectional profile. In this process, depicted schematically in Figure 2.2, reinforcing fibers are pulled from spools and directed into an impregnation tank, where they undergo partial or complete immersion in a thermosetting resin. Following this step, the component is drawn into an initial mold, where it is pre-shaped into the desired form, establishing the resin-to-fiber ratio. Subsequently, the component is subjected to a heated mold, initiating the resin curing process (hardening) and giving it its final, definitive shape (Callister & Rethwisch, 2013).

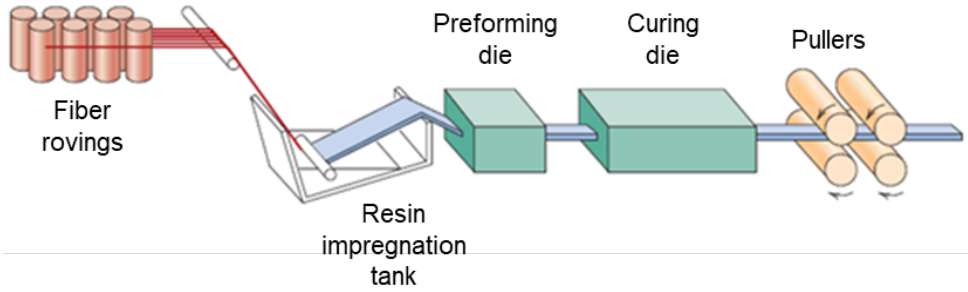

Figure 2.2 - Schematic diagram showing the pultrusion process (Callister & Rethwisch, 2013).

The pultrusion technique boasts a notably high production rate, rendering the process both cost-effective and efficient. Key reinforcements employed in this method encompass glass, carbon and aramid fibers, typically at concentrations ranging from 40 to 70%. Due to their low cost, high mechanical strength and corrosion resistance, E-glass fibers are preferentially used in the manufacturing of

pultruded profiles (Barbero, 2017). Commonly used matrices include polyesters, vinyl esters, and epoxy resins. A major advantage of the pultrusion process lies in its versatility for crafting profiles. Figure 2.3 showcases examples of pultruded profiles, featuring sections commonly encountered in practical engineering applications.

Figure 2.3 - Pultruded profiles (Source: 4peabody.com, accessed on Sep 14, 2020).

Several companies in the market specialize in the fabrication of pultruded profiles, particularly for applications such as stairs, walkways, guardrails, floor grates, and cable trays. However, there has been a growing interest in their utilization as load-bearing elements in critical engineering structures like bridges, towers and walkways, as illustrated in Figure 1.1.

2.3
Mechanical properties

For pultruded materials, it is possible to define a system of orthogonal axes compatible with the direction of the fibers, based on which mechanical properties are identified. Axis 1 is identified as the longitudinal axis in the direction of the fibers, associated with the length of the bar obtained in the pultrusion process. Axis 2 is orthogonal to the fibers and within the plane of the bar walls, and finally, axis 3 is orthogonal to the previous axes (Figure 2.4). In general, pultruded materials with unidirectional reinforcement are defined as orthotropic materials with transverse isotropy, due to the mechanical properties in directions 2 and 3 being similar.

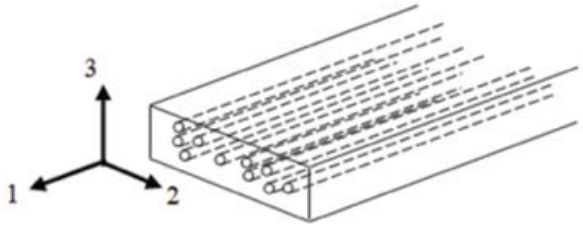

Figure 2.4 - Axis system of the pultruded component (Ribeiro et al., 2008).

The volumetric fraction of fibers represents the proportion of the total composite material volume occupied by fibers, playing a critical role in determining the mechanical properties of the composite. The formulation derived from the Rule of Mixtures allows for the calculation of the mechanical properties of the composite based on the properties of its components and their volumetric fractions (Jones, 1998), as given by:

$$\begin{aligned} E_1 &= E_f V_f + E_m V_m \\ E_2 &= \frac{E_f E_m}{E_f V_m + E_m V_f} \\ G_{12} &= \frac{G_f G_m}{G_f V_m + G_m V_f} \\ \nu_{12} &= \nu_f V_f + \nu_m V_m \end{aligned} \tag{2.1}$$

where E_1 and E_2 are the respective longitudinal and transversal Young's moduli of the composite, E_f and E_m are the respective elastic moduli of the fiber and matrix, both considered isotropic materials, ν_{12} represents the Poisson's ratio in the 1-2 direction of the composite, ν_f and ν_m are the respective Poisson's ratios of the matrix and fiber, and finally, V_f and V_m represent the volumetric fractions of fibers and matrix, respectively. V_m can be expressed as:

$$V_m = 1 - V_f \tag{2.2}$$

Many authors have investigated the mechanical properties of pultruded profiles. For most pultruded profiles, the ratio E_1/E_2 is close to 3.0 and values of E_1/G_{12} are typically in the range of 5 to 10 (Hollaway et al., 2004). An extensive review of the mechanical properties of some commonly used pultruded materials in the literature is reported in Vedernikov et al. (2020). A summary of this review is provided in Table 2.1, Table 2.2 and Table 2.3, for typical matrix, fiber and pultruded element properties, respectively. It can be observed that the lower limit

for the tensile modulus of a pultruded element is in the range of 18-21 GPa, and the upper limit for their shear modulus approaches 5.0 GPa.

The values observed in the literature highlight a significant variety of materials that can be employed as matrix and fibers, enabling many combinations for pultrusion process. The elements of the constituent phases interact synergistically, resulting in an enhanced combination of properties for the composite (Lopes, 2017).

Table 2.1 - Typical matrix properties (Vedernikov et al., 2020).

Material	Tensile Strength (MPa)	Tensile Modulus (GPa)	Flexural Strength (MPa)	Flexural Modulus (GPa)	Shear Strength (MPa)	Shear Modulus (GPa)	Density (kg/m³)	Poisson's ratio
Epoxy	55-130	2.5-4.1	70-140	3.0	46-70	0.98-1.24	1100-1300	0.2-0.37
Polyester	20-100	1.8-4.1	70-132	3.9-4.0	56-70	1.38-1.6	1100-1450	0.1-0.38
Vinylester	70-87	3.0-5.1	149-156	3.2-3.5	-	1.43-1.6	1100-1300	0.3-0.4
Acrylic	56-88	2.2-3.1	117-215	2.9-3.7	-	-	-	-
Fenol	35-60	1.2-1.4	48	-	43	-	1200-1400	-
Polypropylene	34-37.2	0.7	34	1.2-1.5	-	-	900	-
ABS	28-45	1.5-2.4	63-76	2.1-2.2	62.1	1.06	1020-1050	-

Table 2.2 - Typical reinforcement fiber properties (Vedernikov et al., 2020).

Material	Tensile Strength (MPa)	Tensile Modulus (GPa)	Shear Strength (MPa)	Shear Modulus (GPa)	Filament Diameter (μm)	Density (kg/m³)	Poisson's ratio
Basalt	2500-4800	85-110	-	21.7	7-17	2600-2800	0.2-0.26
Carbon	3650-7000	207-600	1400	90	3-7	1700-1800	0.25-0.3
E-glass	2500-4800	70-81.2	830	26-28.8	7-20	2540-2570	0.2-0.3
S-glass	4200-4800	83-93	-	35-39	-	2485-2540	0.21-0.23
Kevlar (Aramid)	2900-3400	70-152	280	2.9	12	1390-1467	0.35

Table 2.3 - Typical pultruded element properties (Vedernikov et al., 2020).

Material	Fiber volume fraction (%)	Density (kg/m³)	Tensile Strength (MPa)	Tensile Modulus (GPa)	Compressive Strength (MPa)	Shear Strength (GPa)	Shear Modulus (GPa)
E-glass roving/polyester	46-80	1600-2000	307-1320	21-59	290-1240	27	3.5
E-glass mat+ roving/polyester	48-61	1750-1900	235-400	18-36	220-485	25-52	2.6-5.0
E-glass roving/vinylester	62	1770	240	18-42	240	22	4.0
E-glass roving/epoxy	52-53	-	414-790	32-40	-	-	3.0-4.5
E-glass roving/ polyurethane	58	-	310-850	37-47	-	-	-
Carbon roving/epoxy	65	1500-1600	1430-2200	130-180	985-1450	72	3.6-4.2
Carbon roving/vinylester	-	1600	2000	140-145	1400	-	-

2.4
Constitutive relations

The constitutive law of orthotropic material with transverse isotropy, which relates deformation and stress through a flexibility matrix with respect to the coordinate system defined in Figure 2.4, contains five independent elastic constants (Jones, 1998):

$$\begin{Bmatrix} \varepsilon_{11} \\ \varepsilon_{22} \\ \varepsilon_{33} \\ \gamma_{23} \\ \gamma_{13} \\ \gamma_{12} \end{Bmatrix} = \begin{bmatrix} \frac{1}{E_1} & -\frac{\nu_{21}}{E_2} & -\frac{\nu_{21}}{E_2} & & & \\ -\frac{\nu_{12}}{E_1} & \frac{1}{E_2} & -\frac{\nu_{32}}{E_2} & & \mathbf{0} & \\ -\frac{\nu_{12}}{E_1} & -\frac{\nu_{23}}{E_2} & \frac{1}{E_2} & & & \\ & & & \frac{2(1+\nu_{23})}{E_2} & 0 & 0 \\ & \mathbf{0} & & 0 & \frac{1}{G_{12}} & 0 \\ & & & 0 & 0 & \frac{1}{G_{12}} \end{bmatrix} \begin{Bmatrix} \sigma_{11} \\ \sigma_{22} \\ \sigma_{33} \\ \tau_{23} \\ \tau_{13} \\ \tau_{12} \end{Bmatrix} \tag{2.3}$$

where:

ε_{ii} = longitudinal strains in the direction i;

γ_{ii} = shear strains in the direction ij;

σ_{ii} = normal stresses in the direction i;

τ_{ii} = shear stresses in the direction ij;

ν_{ii} = Poisson's ratios (strain in the direction i caused by stress in the direction j);

E_i = modulus of elasticity in the direction i; and

G_{ij} = shear modulus in the plane ij.

Due to the symmetry of the flexibility matrix, one obtains:

$$\frac{\nu_{12}}{E_1} = \frac{\nu_{21}}{E_2}$$
$$\frac{\nu_{23}}{E_2} = \frac{\nu_{32}}{E_2} \tag{2.4}$$

Thus, the five elastic constants of the constitutive relation are:

$$\{E_1,\ E_2,\ G_{12},\ \nu_{12},\ \nu_{23}\} \tag{2.5}$$

For a plane stress state, hypothesis commonly assumed for pultruded profiles, the following stresses are null:

$$\begin{Bmatrix} \sigma_{33} \\ \tau_{13} \\ \tau_{23} \end{Bmatrix} = \mathbf{0} \tag{2.6}$$

simplifying the stiffness matrix of the orthotropic material, which yields:

$$\begin{Bmatrix} \sigma_{11} \\ \sigma_{22} \\ \tau_{12} \end{Bmatrix} = \begin{bmatrix} Q_{11} & Q_{12} & 0 \\ Q_{12} & Q_{22} & 0 \\ 0 & 0 & Q_{66} \end{bmatrix} \begin{Bmatrix} \varepsilon_{11} \\ \varepsilon_{22} \\ \gamma_{12} \end{Bmatrix} \tag{2.7}$$

where:

$$Q_{11} = \frac{E_1}{(1-\nu_{12}\nu_{21})}$$
$$Q_{22} = \frac{E_2}{(1-\nu_{12}\nu_{21})} \tag{2.8}$$
$$Q_{12} = \frac{\nu_{21}E_2}{(1-\nu_{12}\nu_{21})}$$
$$Q_{66} = G_{12}$$

In this work, as a reference to the analyses, the material properties were extracted from the experimental work conducted by Cintra et al. (2019) at the Structures and Materials Laboratory of the Civil and Environmental Engineering Department of PUC-Rio and are summarized in Table 2.4. Variations of these properties will be introduced to evaluate the influence of material properties on both linear and nonlinear results, observing the limits shown in Table 2.3.

Table 2.4 - Selected mechanical properties for pultruded profiles.

E_1	21.3 GPa
E_2	6.08 GPa
G_{12}	2.31 GPa
ν_{12}	0,23
ν_{21}	0,066
ρ	1850 kg/m³

3
Mathematical Formulation

This chapter summarizes the formulation of the nonlinear von Kármán plate theory used in the instability and vibrations analysis of angle section profiles. The profile is modelled as two slender plates, as illustrated in Figure 3.1. The compatibility conditions at the connection between the plates are satisfied for each investigated deformation mode, which will be the subject of study in the following chapter.

Figure 3.1 - Typical angle section profile

3.1
Classical Plate Theory

In this work, the von Kármán classical nonlinear plate theory (CPT) is considered. The CPT is commonly adopted for thin plates, where shear deformations have negligible effects and can be disregarded (Wang et al., 2000).

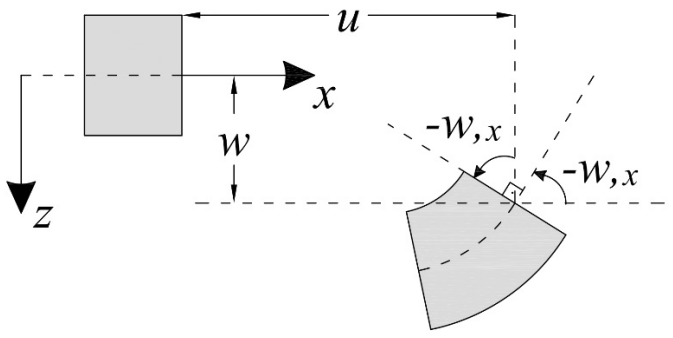

Figure 3.2 - Classical Plate Theory assumption.

The von Kármán classical plate theory is based on the Kirchhoff assumptions (Brush & Almroth, 1975):

1 - Straight lines normal to the undeformed middle surface of the plate remain straight, normal, and inextensible after deformation (as illustrated in Figure 3.2), allowing the shear deformations γ_{xz} and γ_{yz} to be neglected;

2 - The normal stress σ_z and the corresponding strain are negligible, and therefore, the transversal deflection of any point on the plate (x, y, z) is equal to the transversal deflection of the corresponding point on the mid-surface (x, y, 0).

In general, plates are classified as thick plates when the minimum dimension to thickness ratio (b/t) is less than 10 and thin plates when the (b/t) ratio ranges from 10 to about 100 (Chia, 1980; Musmar, 2022). The effect of shear may increase in thin composite plates. However, Coaquira (2020) compared through a systematic parametric analysis the effect of the first order shear plate theory on the linear and nonlinear buckling and vibration results of slender pultruded channel section profiles, and concluded that the CPT leads to reliable results for $b/t \geq 10$, as confirmed by the present results.

Consider a thin-walled column of length L with a slender unequal-leg angle section discretized as two plates. The longer leg is labeled plate 1, with width b_1 and thickness t_1, and the shorter leg is labeled plate 2, with width b_2 and thickness t_2, as illustrated in Figure 3.3 ($b_1 \geq b_2$ throughout this work), with the global coordinate system located at the geometric center (gc). Since most commercially available pultruded shapes have constant thickness, it is hereafter assumed that $t_1 = t_2 = t$. The column is axially loaded at the ends with a distributed load per unit length N along the edges (Figure 3.3a). Figure 3.3b shows a plate element together with the local coordinate system and the corresponding displacement field. The Kirchhoff assumptions imply that (Brush & Almroth, 1975):

$$\begin{aligned} \overline{u} &= u - z w_{,x} \\ \overline{v} &= v - z w_{,y} \\ \overline{w} &= w \end{aligned} \tag{3.1}$$

where $\overline{u}$ and $\overline{v}$ are the in-plane displacement components in the x and y directions of the local coordinate system, respectively, and $\overline{w}$ is the transversal displacement in the z direction of an arbitrary point of coordinates (x, y, z); u, v and w are the

corresponding displacements of the middle surface ($z = 0$). The subscripts after comma indicate derivatives with respect to the corresponding spatial variable.

Figure 3.3c illustrates the cross-section of the angle profile, constituted by the union of two orthogonal plates. The local x-axis of each plate coincides with the common edge, passing through the section shear center (sc), whose distance from the geometric center (gc) is given by the coordinates (z_{gc}, y_{gc}), being parallel to the global axis X. Thus, the origin of the local axes y_1 and y_2 coincides with the shear center, being y_1 and y_2 parallel to the global Y and Z axes, respectively.

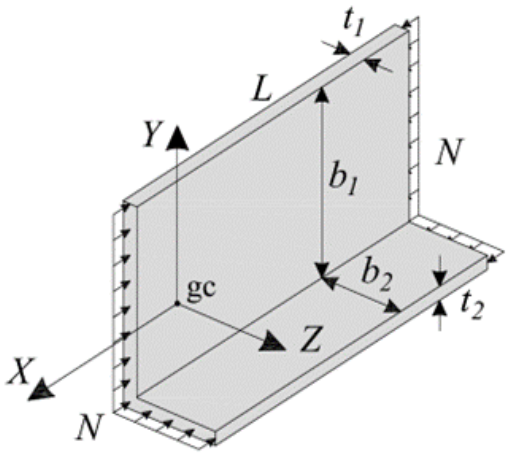

(a) profile geometry and global coordinate system

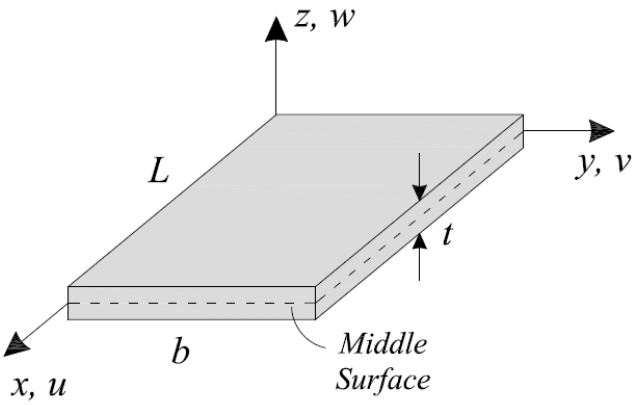

(b) Plate element, local coordinate system and displacement field

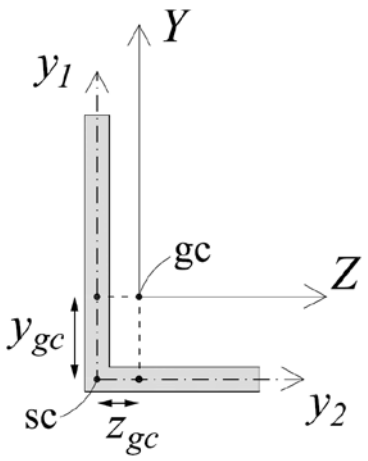

(c) cross section, global reference frame, and shear center coordinates

Figure 3.3 - Angle section profile.

For small strains and moderate rotations, considering the nonlinear terms of the von Kármán plate theory, the strain-displacement relations for of an arbitrary point of the plate are given by:

$$\begin{aligned}
\bar{\varepsilon}_x &= \bar{u}_{,x} + \frac{1}{2}\bar{w}_{,x}^2 \\
\bar{\varepsilon}_y &= \bar{v}_{,y} + \frac{1}{2}\bar{w}_{,y}^2 \\
\bar{\gamma}_{xy} &= \bar{u}_{,y} + \bar{v}_{,x} + \bar{w}_{,x}\bar{w}_{,y}
\end{aligned} \tag{3.2}$$

Substituting eq. (3.1) into eq. (3.2), the strain-displacement relations at any point of the plate can be written in terms of the middle surface quantities as:

$$\begin{aligned}
\bar{\varepsilon}_x &= \varepsilon_x + z\kappa_x \\
\bar{\varepsilon}_y &= \varepsilon_y + z\kappa_y \\
\bar{\gamma}_{xy} &= \gamma_{xy} + 2z\kappa_{xy}
\end{aligned} \tag{3.3}$$

where ε_x, ε_y and γ_{xy} are the normal and shear strain components in the plate middle surface; κ_x and κ_y are the curvatures in the x and y directions, respectively, and κ_{xy} is the twist.

Therefore, the strain-displacement relations of the plate mid-surface and changes of curvature are:

$$\begin{aligned}
\varepsilon_x &= u_{,x} + \frac{1}{2}w_{,x}^2 \\
\varepsilon_y &= v_{,y} + \frac{1}{2}w_{,y}^2 \\
\gamma_{xy} &= u_{,y} + v_{,x} + w_{,x}w_{,y} \\
\kappa_x &= -w_{,xx} \\
\kappa_y &= -w_{,yy} \\
\kappa_{xy} &= -\frac{1}{2}\left(w_{,xy} + w_{,yx}\right)
\end{aligned} \tag{3.4}$$

The effect of initial geometric imperfections can be described by a function $w_0(x, y)$. By incorporating this function into the kinematic relations, one obtains:

$$\begin{aligned}
\varepsilon_x &= u_{,x} + \frac{1}{2} w_{,x}^2 + w_{,x} w_{0,x} \\
\varepsilon_y &= v_{,y} + \frac{1}{2} w_{,y}^2 + w_{,y} w_{0,y} \\
\gamma_{xy} &= u_{,y} + v_{,x} + w_{,x} w_{,y} + w_{,x} w_{0,y} + w_{0,x} w_{,y} \\
\kappa_x &= -w_{,xx} \\
\kappa_y &= -w_{,yy} \\
\kappa_{xy} &= -\frac{1}{2}\left(w_{,xy} + w_{,yx} \right)
\end{aligned} \tag{3.5}$$

The resultant forces per unit length in a plate element can be obtained by integrating the stresses along the plate thickness, as follows:

$$\begin{aligned}
\begin{Bmatrix} N_x \\ N_y \\ N_{xy} \end{Bmatrix} &= \int_{-t/2}^{t/2} \begin{Bmatrix} \bar{\sigma}_x \\ \bar{\sigma}_y \\ \bar{\tau}_{xy} \end{Bmatrix} dz \\
\begin{Bmatrix} M_x \\ M_y \\ M_{xy} \end{Bmatrix} &= \int_{-t/2}^{t/2} \begin{Bmatrix} \bar{\sigma}_x \\ \bar{\sigma}_y \\ \bar{\tau}_{xy} \end{Bmatrix} z dz
\end{aligned} \tag{3.6}$$

where $\bar{\sigma}_x$, $\bar{\sigma}_y$ and $\bar{\tau}_{xy}$ denote the normal and shear stress components, N_x, N_y and N_{xy} are the normal and shear in-plane force resultants per unit length, and M_x, M_y and M_{xy} are the flexural and torsional moment resultants per unit length, as illustrated in Figure 3.4. It is assumed that the Cauchy stress tensor components are linearly related to the strains by Hooke's law.

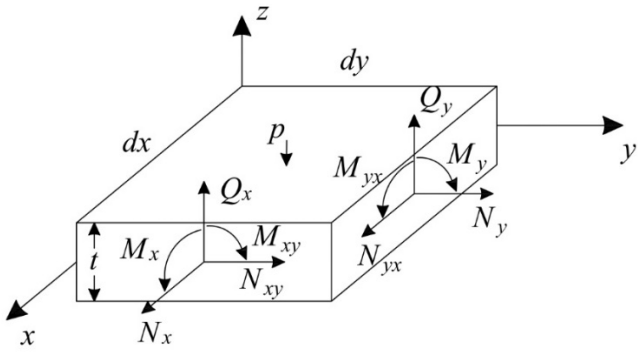

Figure 3.4 - Plate element and internal force resultants per unit length in the local coordinate system (positive directions).

The pultrusion manufacturing process causes the FRP plates to exhibit well-defined mechanical properties in two main directions defined by the fibers (see Figure 2.4). Considering the constitutive equations of a typical orthotropic material,

the expression relating the internal forces and moments to the mid-surface strain measures of the FRP plate element can be written as:

$$\begin{Bmatrix} N_x \\ N_y \\ N_{xy} \\ M_x \\ M_y \\ M_{xy} \end{Bmatrix} = \begin{bmatrix} A_{11} & A_{12} & 0 & 0 & 0 & 0 \\ A_{12} & A_{22} & 0 & 0 & 0 & 0 \\ 0 & 0 & A_{66} & 0 & 0 & 0 \\ 0 & 0 & 0 & D_{11} & D_{12} & 0 \\ 0 & 0 & 0 & D_{12} & D_{22} & 0 \\ 0 & 0 & 0 & 0 & 0 & D_{66} \end{bmatrix} \begin{Bmatrix} \varepsilon_x \\ \varepsilon_y \\ \gamma_{xy} \\ \kappa_x \\ \kappa_y \\ \kappa_{xy} \end{Bmatrix} \tag{3.7}$$

where A_{ij} and D_{ij} (i, j = 1, 2, 6) are the plate membrane and bending stiffness coefficients defined by the following integrals along the plate thickness:

$$A_{ij} = \int_{-t/2}^{t/2} Q_{ij} dz$$
$$D_{ij} = \int_{-t/2}^{t/2} Q_{ij} z^2 dz \tag{3.8}$$

The x direction coincides with the direction of the fibers along the column length, the y direction is perpendicular to the fibers along the plate width, and the z direction coincides with the normal to the plate surface. The quantities Q_{ij} are written in terms of the elastic constants of the material, as previously shown in eq (2.8).

3.2
Variational formulation

The strain energy, U, is given by the volume integral:

$$U = \frac{1}{2} \iiint_V \left(\bar{\sigma}_x \bar{\varepsilon}_x + \bar{\sigma}_y \bar{\varepsilon}_y + \bar{\tau}_{xy} \bar{\gamma}_{xy} \right) dV \tag{3.9}$$

Considering eqs. (3.3) to (3.6), eq. (3.9) becomes:

$$U = \frac{1}{2}\int_0^b \int_0^a \Big[N_x \left(u_{,x} + \frac{1}{2} w_{,x}^2 + w_{,x} w_{0,x} \right) + N_y \left(v_{,y} + \frac{1}{2} w_{,y}^2 + w_{,y} w_{0,y} \right) + N_{xy} \left(u_{,y} + v_{,x} + w_{,x} w_{,y} + w_{,x} w_{0,y} + w_{0,x} w_{,y} \right) + M_x \kappa_x + M_y \kappa_y + M_{xy} \kappa_{xy} \Big] \, dx \, dy \tag{3.10}$$

Introducing the expressions for internal forces and moments, eq. (3.7), into eq (3.10) yields:

$$U = \frac{1}{2}\int_0^b \int_0^L \Big[A_{11} \left(u_{,x} + \frac{1}{2} w_{,x}^2 + w_{,x} w_{0,x} \right)^2 + A_{22} \left(v_{,y} + \frac{1}{2} w_{,y}^2 + w_{,y} w_{0,y} \right)^2 + 2A_{12} \left(u_{,x} + \frac{1}{2} w_{,x}^2 + w_{,x} w_{0,x} \right) \left(v_{,y} + \frac{1}{2} w_{,y}^2 + w_{,y} w_{0,y} \right) + A_{66} \left(u_{,y} + v_{,x} + w_{,x} w_{,y} \right)^2 + D_{11} \kappa_x^2 + 2D_{12} \kappa_x \kappa_y + D_{22} \kappa_y^2 + 4D_{66} \kappa_{xy}^2 \Big] \, dx \, dy \tag{3.11}$$

The potential energy of the applied loads, V, for a plate under uniform axial compression, is written as (Brush & Almroth, 1975):

$$V = -N_x \int_0^b \int_0^L u_{,x} \, dx \, dy \tag{3.12}$$

where N_x is the applied axial load per unit length at $x = 0$ and $x = L$, as shown in Figure 3.3a.

Disregarding rotational inertia, a commonly adopted assumption for thin plates, the kinetic energy T of the plate is given by:

$$T = \frac{\rho t}{2} \iint_A \left(\dot{u}^2 + \dot{v}^2 + \dot{w}^2 \right) dx \, dy \tag{3.13}$$

where the superscript $(\cdot)$ denotes the derivative with respect to time, $\bar{t}$, and ρ is the material density.

The introduction of damping into the energy functional is achieved by considering the non-conservative work done by a frictional force, as shown:

$$W_{nc} = \iint_A \frac{1}{2} \bar{c} \left(\dot{u}^2 + \dot{v}^2 + \dot{w}^2 \right) dx \, dy \tag{3.14}$$

where c is the damping coefficient, given by:

$$\overline{c} = 2\Xi\rho t\omega_0 \tag{3.15}$$

where Ξ is the linear viscous damping parameter and ω_0 is the natural frequency of the system.

The Lagragian of the system, L_g, considering the two plates of the angle profile, is given by:

$$\begin{aligned} L_g &= \sum_{i=1}^{2} T_i - \Pi \\ \Pi &= \sum_{i=1}^{2} U_i + V_i \end{aligned} \tag{3.16}$$

where Π is the total potential energy of the system.

Consider, following the variational methodology adopted in Brush & Almroth (1975) and the Lagrange-Dirichlet theorem, that the fundamental static equilibrium configuration is described by the displacement field U_0 (usually the plate membrane solution under the in-plane loads) and an incremental displacement field, U_1. Then the variation of the total potential energy between the two states is given by $\Delta\Pi = \Pi(U_0+U_1)-\Pi(U_0)$. Considering the nonlinear strain-displacement relations, eq. (3.4), the variation of the total potential energy can be written as:

$$\Delta\Pi = \delta\Pi\big|_{U_0} + \frac{1}{2!}\delta^2\Pi\Big|_{U_0} + \frac{1}{3!}\delta^3\Pi\Big|_{U_0} + \frac{1}{4!}\delta^4\Pi\Big|_{U_0} \tag{3.17}$$

Where $\delta^n\Pi$ is the n-*th* variation of the functional. Since U_0 is an equilibrium configuration, $\delta\Pi|_{U0} = 0$ and, according to the Trefftz criterion, $\delta(\delta^2\Pi) = 0$, which leads to the criticality condition that will be used herein to obtain the buckling eigenvalue problem. The kinetic energy is given in terms of the incremental time dependent displacements only and the equations of motion are obtained using Hamilton's principle ($\delta L_g = 0$).

The explicit equations of motion of the pre-loaded plate are given by:

$$\left[A_{11}\left(u_{,x}+\tfrac{1}{2}w_{,x}^{2}+w_{,x}w_{0,x}\right)+A_{12}\left(v_{,y}+\tfrac{1}{2}w_{,y}^{2}+w_{,y}w_{0,y}\right)\right]_{,x} + \left[A_{66}\left(u_{,y}+v_{,x}+w_{,x}w_{,y}+w_{,x}w_{0,y}+w_{0,x}w_{,y}\right)\right]_{,y}=\rho h\ddot{u} \tag{3.18}$$

$$\left[A_{12}\left(u_{,x}+\tfrac{1}{2}w_{,x}^{2}+w_{,x}w_{0,x}\right)+A_{22}\left(v_{,y}+\tfrac{1}{2}w_{,y}^{2}+w_{,y}w_{0,y}\right)\right]_{,y} + \left[A_{66}\left(u_{,y}+v_{,x}+w_{,x}w_{,y}+w_{,x}w_{0,y}+w_{0,x}w_{,y}\right)\right]_{,x}=\rho h\ddot{v} \tag{3.19}$$

$$\begin{aligned} &D_{11}w_{,xxxx}+2D_{12}w_{,xxyy}+D_{22}w_{,yyyy}+4D_{66}w_{,xxyy} \\ &-\Big\{\left[A_{11}\left(u_{,x}+\tfrac{1}{2}w_{,x}^{2}+w_{,x}w_{0,x}\right)+A_{12}\left(v_{,y}+\tfrac{1}{2}w_{,y}^{2}+w_{,y}w_{0,y}\right)\right]w_{,xx} \\ &+2\left[A_{66}\left(u_{,y}+v_{,x}+w_{,x}w_{,y}+w_{,x}w_{0,y}+w_{0,x}w_{,y}\right)\right]w_{,xy} \\ &+\left[A_{12}\left(u_{,x}+\tfrac{1}{2}w_{,x}^{2}+w_{,x}w_{0,x}\right)+A_{22}\left(v_{,y}+\tfrac{1}{2}w_{,y}^{2}+w_{,y}w_{0,y}\right)\right]w_{,yy}\Big\}=\rho h\ddot{w} \end{aligned} \tag{3.20}$$

3.3
Ritz method

The Ritz method is a common variational method used to discretize an energy functional (Leissa, 2005). It is an effective tool for solving linear and nonlinear problems when the resulting differential equations from the physical model are complex, but approximation functions can be easily derived for the specified boundary conditions. The method involves solving the system of differential equations in weak form, generating approximate solutions.

In the Ritz method, the exact solution for the displacement fields *u*, *v* and *w* is replaced by approximate solutions, υ_n, given by the linear combination of admissible functions that satisfy the essential boundary conditions of the problem, typically trigonometric or polynomial functions. This solution is usually expressed as:

$$\upsilon_n=\sum_{n=1}^{n_d}C_n\upsilon_{Xn}\upsilon_{Yn} \tag{3.21}$$

where C_n are the modal amplitudes, υ_{Xn} and υ_{Yn} are the admissible functions adopted for the plate in the *x* and *y* coordinates, respectively, and n_d represents the number of terms used in the modal expansion.

The number of terms used represents a crucial factor in the accuracy of numerical results. A higher number of modes leads to an approximate solution that is closer to the analytical solution. For the buckling and vibrations analyses using the CPT, the displacement fields related to the predominant deformation modes will be analytically deduced. The accuracy of linear results will be examined through comparisons with outcomes provided by GBTul software (Bebiano et al., 2008a; Bebiano et al., 2018).

4
Reduced-Order Models

In this chapter, reduced-order models (ROMs) are derived for the displacement fields associated with the predominant deformation modes of a general angle section profile, based on the nonlinear equations of motion. Initially, a brief introduction to the GBTuL program is provided. The GBTuL program is then used to explore the influence of geometric and physical parameters on modal participation. Finally, based on the modal participation analyses, the displacement fields of the two plates of the angle section profile are analytically derived for each of the predominant deformation modes, enabling the development of coupled and uncoupled consistent reduced-order models.

4.1
GBTuL

The GBTuL program is a free-access software developed at the Technical University of Lisbon (UTL) based on the Generalized Beam Theory (GBT). The software performs elastic buckling and vibration analyses of open and closed thin-walled section profiles (Bebiano et al., 2008a; Bebiano et al., 2008c).

The software considers as approximation function a linear combination of deformation modes, which represent the deformed shapes of the profile cross-section and calculates the participation of each mode in the buckling and vibration modes (Bebiano et al., 2008a). The main distinctive feature of GBT is the approximation of the cross-section displacement field by a linear combination of deformation modes with a clear structural meaning. The deformation modes are obtained through a set of displacement fields associated with the constituent plates of the profile, where the fields for each plate are described by a set of polynomial functions. Thus, the displacement components in the axial, transverse, and normal directions can be expressed as:

$$\zeta_k = \begin{cases} u_k(x,s) = u_k(s)\varphi_k(x) \\ v_k(x,s) = v_k(s)\varphi_k(x) \\ w_k(x,s) = w_k(s)\varphi_k(x) \end{cases} \tag{4.1}$$

where $u_k(s)$, $v_k(s)$ and $w_k(s)$ are the modal displacement defined along the cross-section mid-line for mode k, and $\varphi_k(x)$ are the longitudinal functions (the summation convention applies to subscript k).

For given material properties and cross-section geometry, the cross-section analysis leads to the identification of its deformation modes and the evaluation of the corresponding modal mechanical properties. The GBT elastic strain energy, U, takes into account the stiffness matrices associated with several cross-section properties, namely primary/secondary warping, transverse extension/flexure, wall shear distortion/torsion and membrane/flexural Poisson effects. For the simply supported condition, the interpolating function can be defined as:

$$\varphi_k(x) = C_k(\overline{t})\sin\left(\frac{m\pi x}{L}\right) \tag{4.2}$$

The contribution of a given cross-section deformation mode in a member deformed configuration (buckling or vibration mode) consists of determining its modal participation factor P_k, on the basis of its contribution to the total strain energy of the system. It is defined as:

$$P_k = \frac{U_k}{\sum_{i=1}^{n_d} U_i} \tag{4.3}$$

where n_d is the total number of deformation modes included in the analysis.

The member analysis yields the solution of the buckling or vibration eigenvalue problem, namely the corresponding eigenvalues (buckling loads or natural frequencies) and eigenvectors (buckling or vibration mode shapes). Illustrative examples, the fundamentals as well as instructions on the use of the GBTuL program, can be found in Bebiano et al. (2018).

The results obtained from the proposed linear analyses using the classical plate theory are compared in Chapter 5 and validated against the results obtained from GBTuL. Although GBTuL has been chosen as a comparison benchmark for this work, other approaches could also be used, such as programs based on the finite strip method (Schafer, 2020).

4.2
Modal participation

For the development of the ROMs, first the buckling and vibration modes of the FRP angle profile are investigated using the GBTuL software, which allows to identify the dominant buckling and vibration modes as a function of material and geometric parameters and compute their modal content (Bebiano at al., 2018). The buckling behavior of an angle section member under axial compression can be described by one or more of the local or global (torsional, major-axis flexural and minor-axis flexural) displacement patterns illustrated in Figure 4.1 (Dinis et al., 2010; Behzadi-Sofiani et al., 2021). The major and minor principal axes of the cross section are represented by *z*' and *y*', respectively. The major-axis flexural displacement pattern involves the corner moving in the direction of the minor axis, while the opposite occurs for the minor-axis flexural displacement pattern, where the corner shifts in the direction of the major axis. Torsion takes the form of a rigid-body rotation of the cross-section around the shear center and may occur in combination with major-axis flexure, mainly in equal-leg angle section columns of short-to-intermediate length, or with minor-axis flexure, mostly in unequal-leg cases, as will be shown hereafter. The local plate buckling displacement profiles essentially resemble the rotation of the entire cross-section about its shear center. This assumes that the angle of rotation is identical for both plate elements when they buckle simultaneously with the deformation pattern along the plate width satisfying the continuity condition at the plate's connection and the opposite free boundary, as illustrated in Figure 4.1a.

In this work, the profile walls are assumed to be simply supported (SS) at the loaded ends (end sections globally pinned and free to warp) but the axial rotation is restricted at the supports to prevent rigid body rotation around the *X* axis (He et al., 2024). Compatibility at the junction between the plates (legs) is ensured on the deformation modes. The other two edges of the two plates are assumed to be free.

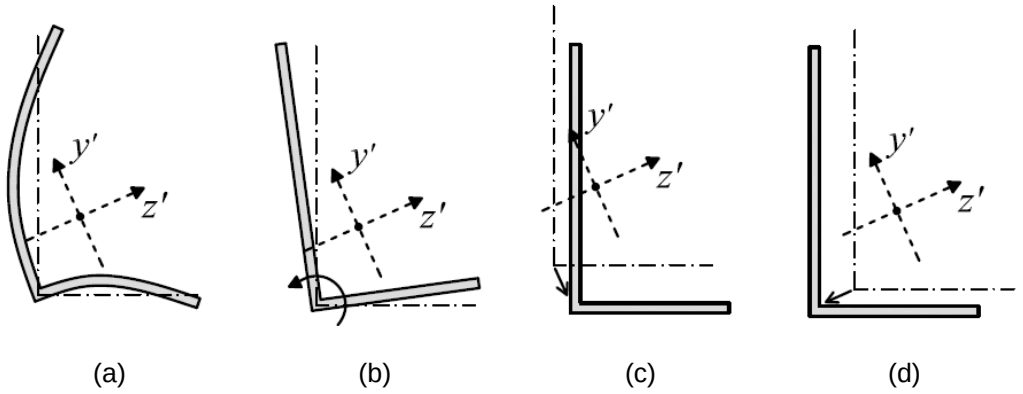

(a) (b) (c) (d)

Figure 4.1 - Cross-section displacement patterns for angle columns under axial compression, showing: (a) local, (b) torsional, (c) major axis flexural, and (d) minor axis flexural modes. Dashed profile: initial undeformed configuration. Continuous profile: deformed configuration.

Based on the geometry of the angle section, see Figure 3.3, the cross sections are labelled as L b_1xb_2xt, with dimensions in millimeters. Furthermore, the aspect ratio for the angle section legs is defined as:

$$\beta = \frac{b_2}{b_1} \tag{4.4}$$

where β = 1,0 denote equal-leg sections and β = 0 means that the profile is reduced to a single plate, as b_2 becomes zero.

A detailed parametric analysis was performed to study the dominant modes as a function of the profile geometry. In order to illustrate the influence of the parameter β on the modal participation, two angle section profiles are adopted, one having equal-legs (L 150x150x5; β = 1.0), and the other one having unequal-legs (L 150x75x5; β = 0.5), both with the same thicknesses (t = 5 mm) as illustrated in Figure 4.2. As mentioned in the preceding chapter, the material properties, unless stated otherwise, are summarized in Table 2.4.

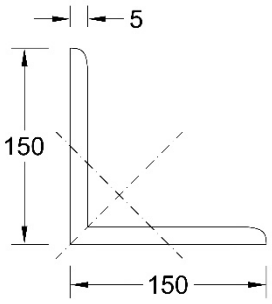

(a) Equal-leg section
(L 150x150x5, β = 1.0, b_2/t=30)

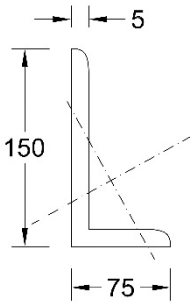

(b) Unequal-leg section
(L 150x75x5, β = 0.5, b_2/t=15)

Figure 4.2 - Angle section profiles.

Figure 4.3 shows the variation of the modal participation in the buckling and vibration fundamental mode of both sections as a function of the column length, L. For the equal-leg section (β = 1.0), the torsional mode is dominant while the bending mode around the major axis has a low participation, reaching a maximum of 2.0% when L = 4 m. On the other hand, for the unequal-leg section (β = 0.5), although torsion is predominant for all lengths up to L = 4 m, both torsion and minor axis bending modes are equally important, with the modal participation of the torsional mode decreasing and the modal participation of the minor axis bending mode increasing as the profile length increases. There is a critical length, function of the material and geometric parameters, where the blue and green curves intercept and the influence of minor axis bending becomes dominant. This critical length decreases as the thickness and shear modulus increases within the present constraints. Figure 4.4 shows the results for a thicker profile (L 150x75x7; β = 0.5; t=7mm). In this case, minor axis bending becomes dominant for L > 3.03 m. Furthermore, a neglected participation of the local-plate mode can be observed in the unequal-leg case for short lengths (L < 1 m).

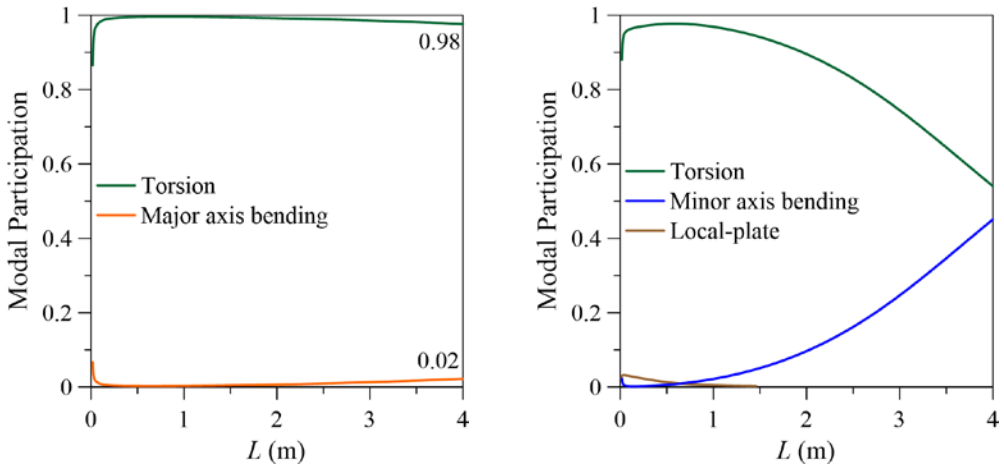

(a) L 150x150x5 (β = 1.0). (b) L 150x75x5 (β = 0.5).

Figure 4.3 - Variation of the modal participation in the first buckling and vibration mode for the angle profiles as a function of the column length.

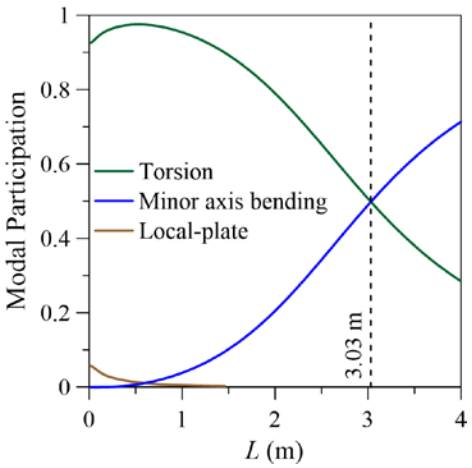

Figure 4.4 - Variation of the modal participation in the first buckling and vibration mode for the angle L 150x75x7 (β = 0.5) as a function of the column length.

These results show that the parameter $\beta = b_2/b_1$ has an important influence on the modal participation, differentiating the behavior of equal-leg and unequal-leg profiles, a topic not explored in the technical literature. Figure 4.5a shows the variation of the modal participation for a column with intermediate length, L = 2.5 m, with the shorter leg width b_2 varying from 50 mm to 150 mm, keeping b_1 = 150 mm and t = 5 mm. The corresponding range of β is shown by the upper horizontal axis. It is observed that the participation of the torsional mode increases steadily approaching 1, while the participation of the minor axis bending mode decreases to zero. In parallel, the participation of major axis bending mode, although rather small, increases slowly, in agreement with Figure 4.3a. Decreasing the longer leg to b_1 = 75 mm and keeping t = 5 mm and the same column length,

L = 2.5 m, Figure 4.5b shows the variation of the modal participation with the shorter leg width b_2 varying from 25 mm to 75 mm (the same range of parameter $\beta = b_2/b_1$). The modal participation is strongly altered by the leg-asymmetry when compared with Figure 4.5a. The minor axis bending mode is dominant and the relevance of the torsional mode decreases throughout the studied range. As the leg-asymmetry decreases, the contribution of the minor axis bending decreases while the torsional mode participation increases up to $\beta = 0.8$, inverting their contribution subsequently and the influence of torsion cease to exist for the symmetric profile ($\beta = 1$). A very small contribution of the major axis bending mode is also detected.

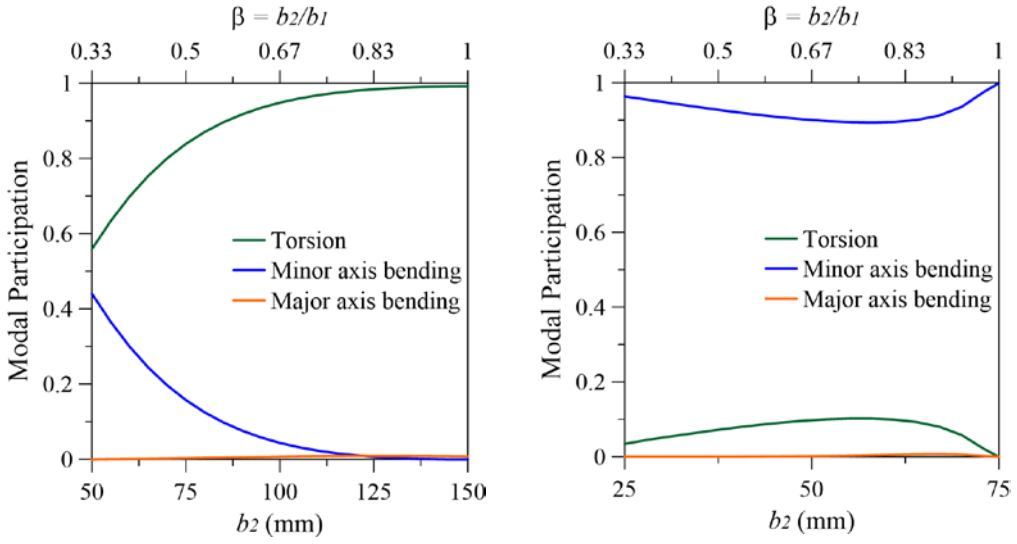

(a) L 150xb_2x5 (β = 1.0). (a) L 75xb_2x5 (β = 0.5).

Figure 4.5 - Modal participation as a function of the shorter length b_2 in the first buckling and vibration mode for the unequal-leg angle profiles (L = 2.5 m).

It is known that in equal-leg section columns, minor-axis flexural buckling predominates in long angle profiles, while flexural-torsional buckling occurs in shorter columns (Behzadi-Sofiani et al., 2021). This phenomenon can be observed as the leg's width decreases, keeping the thickness constant. In order to illustrate this, Figure 4.6 presents the modal participation for the equal-leg angles L 75x75x5 and L 50x50x5. Here, the wider plate aspect ratio of a general angle section profile is defined as:

$$\varphi = \frac{b_1}{L} \tag{4.5}$$

where b_1 is the wider plate's width (according to Figure 3.3a). The parameter is given on the upper x-axis of Figure 4.6 as $\varphi = b/L$, since $b_1 = b_2 = b$ in equal-leg

profiles. In both cases, a sudden discontinuous transition can be observed in the modal participation at a certain length, which is a function of the material and geometric parameters. For the L 75x75x5 section the transition length is L_t = 2.30 m (φ = 0.032) while for the L 50x50x5 section it decreases to L_t = 1.02 m (φ = 0.049). The results confirm that, the coupling between torsion and major axis bending governs the response for shorter lengths, while for longer profiles, minor axis bending becomes fully responsible for the linear behavior. For the slender cross section L 150x150x5 no transition was observed (see Figure 4.3a). These examples illustrate the predominant modes in the buckling and vibration analysis of angle section columns.

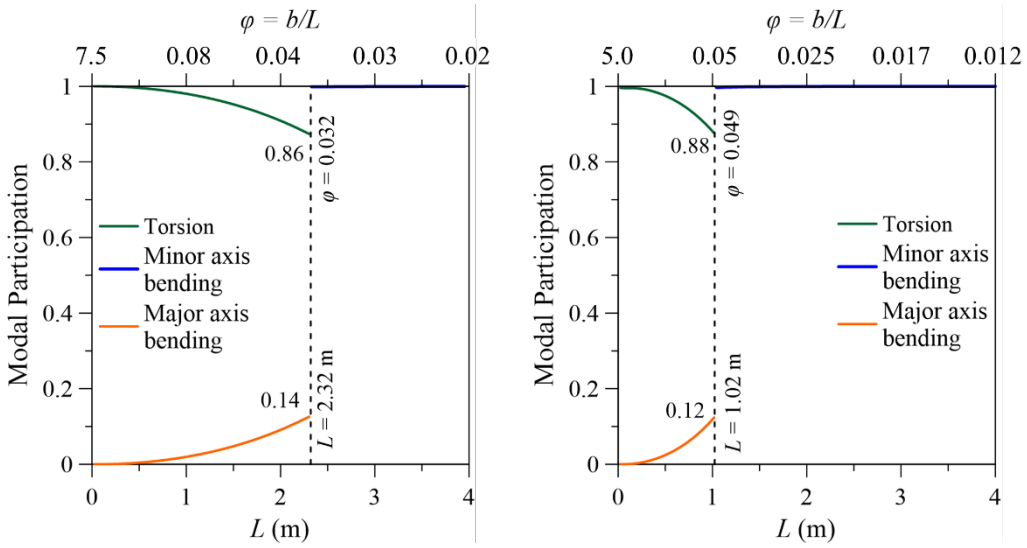

(a) L 75x75x5 (β = 1.0, b_i/t=15) (a) L 50x50x5 (β = 1.0, b_i/t=10)

Figure 4.6 - Variation of the modal participation in the first buckling and vibration mode for the angle profiles as a function of the column length.

The influence of the material properties on the modal participation of angle section profiles is also studied. Four distinct materials are considered, as shown in Table 4.1. The materials are denoted as M1, M2, M3 and M4, with the first three being typical pultruded materials (Cintra et al., 2019), and the last one being an isotropic material, where $E_1 = 2G_{12}(1-\nu)$. For all materials, ν_{12} = 0.23 is assumed. Observe that the material M2 was the same considered in the previous analyses.

Here, the nondimensional material parameter ψ is defined as:

$$\psi = \frac{G_{12}\left(1-\nu_{12}\nu_{21}\right)}{E_1} \tag{4.6}$$

One can observe that the isotropic material has the highest material parameter (ψ = 0.3850), given that the relationship $E_1 = 2G_{12}(1-\nu)$ results in a high value for the shear modulus, deviating from the typical E_1/G_{12} ratio for pultruded materials that lies between 5 to 10. Substituting the isotropic relationship into eq. (4.6), the material parameter equation for isotropic materials can be simplified to $\psi = (1-\nu)/2$.

Table 4.1 - Pultruded and isotropic materials.

Material	E_1	E_2	G_{12}	ν_{12}	ν_{21}	ψ
M1	36.8	6.08	3.12	0.23	0.04	0.0835
M2	21.3	6.08	2.31	0.23	0.07	0.1068
M3	17.2	5.50	3.10	0.23	0.07	0.1775
M4	21.3	21.3	8.66	0.23	0.23	0.3850

Figure 4.7 shows the variation of the modal participation in the buckling and vibration fundamental mode of the angle L 75x75x5 for each of the materials in Table 4.1. It is observed that the abrupt transition between the major-axis flexural-torsional mode and pure minor-axis bending occurs for shorter profile lengths as the material parameter ψ increases. This indicates that a material profile with a higher ψ value is more prone to pure bending for a wider range of profile lengths, in agreement with existing results for steel sections. As will be shown in later chapters, the transition point between modal participations exhibits a sudden change in post-critical stiffness and nonlinear vibration amplitudes.

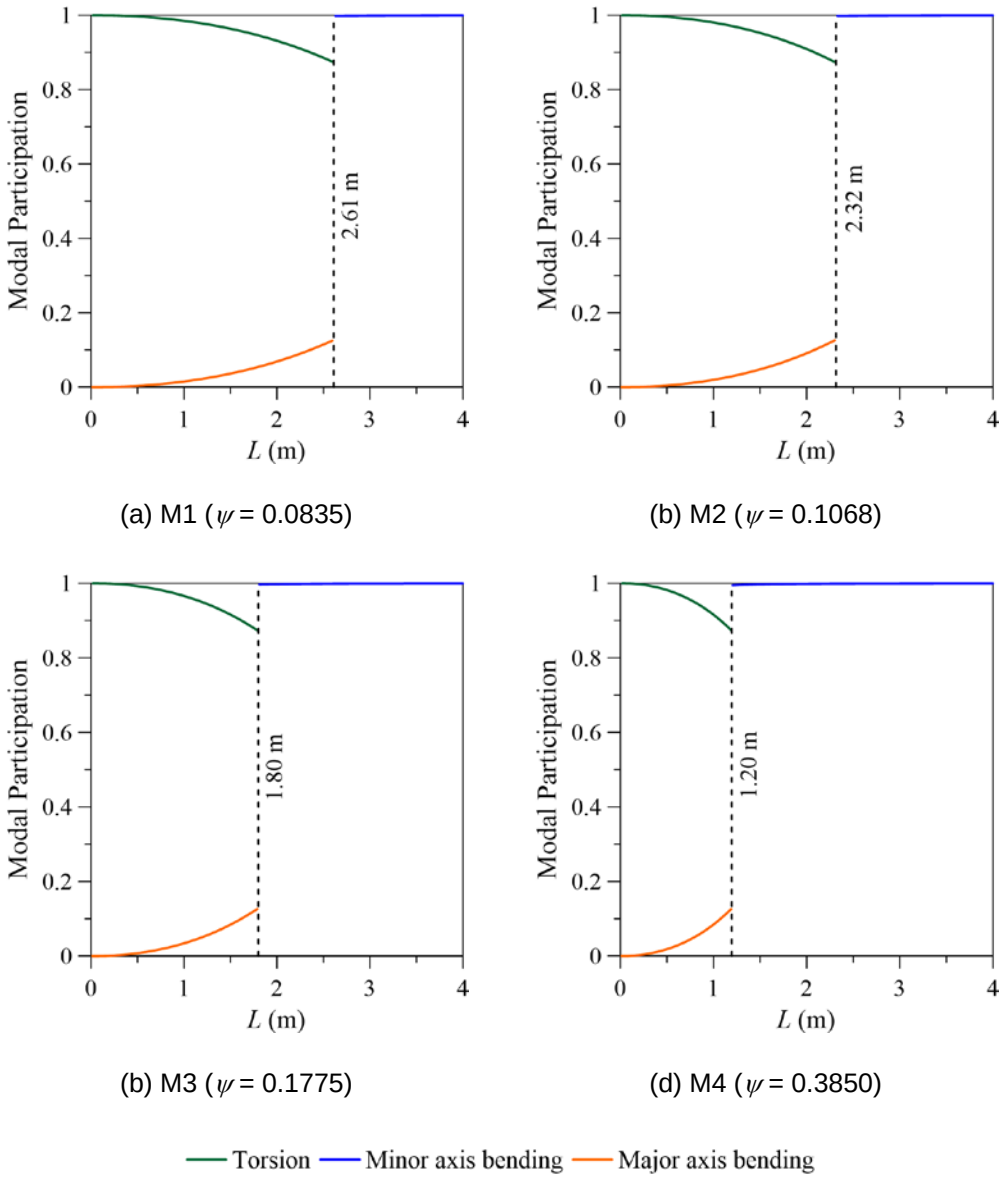

(a) M1 (ψ = 0.0835) (b) M2 (ψ = 0.1068)

(b) M3 (ψ = 0.1775) (d) M4 (ψ = 0.3850)

Figure 4.7 - Variation of the modal participation in the first buckling and vibration mode for the angle L 75x75x5 (β = 1.0) as a function of the column length, considering the materials of Table 4.1.

4.3
Reduced-order models

Based on the previous parametric analyses, the ROMs for the buckling and vibration analysis of angle-sections are here proposed, including: (1) pure minor axis bending, (2) pure torsion, (3) torsion plus minor axis bending and (4) torsion plus major axis bending. In order to discretize the Lagragian, appropriate shape functions for the displacement field of the angle plates need to be derived in each case. It is shown in the following chapters that rather low-dimensional ROMs

considering properly selected modes can describe with good accuracy the response of the slender angle section pultruded profiles for a large range of geometries.

The displacements of a single mode are separated into the products of a time function and two spatial functions. For each constituent plate, the set of admissible functions for the displacement components (u, v, w) takes the form:

$$\zeta_k\left(x, y, \bar{t}\right) = C_k e^{i\omega_0 \bar{t}}\, g(x)\, f\left(y\right) \tag{4.7}$$

in which ω_0 is the free vibration frequency, ζ_k represents one of the displacement components (u, v, w), C_k is the modal amplitude, and $g(x)$ and $f(y)$ are the shape functions in the x and y directions, respectively, where $g(x)$ must satisfy the plate boundary conditions at $x = [0, L]$ and $f(y)$ depends on the continuity conditions along the connection of the two plates and the opposite free boundary. Here, the columns are assumed to be simply supported and allowed to rotate about their two principal axes.

4.3.1
Minor axis bending mode

The global coordinate system (X, Y, Z) and the local coordinate system of each plate (x, y, z) used here are shown in Figure 3.3. In order to derive the required shape functions, the local coordinates axes (y_1, y_2), located at the shear center (sc) of the section and parallel to the legs, is used to identify the in-plane axes along the width of plates 1 and 2, respectively (see cross-section in Figure 3.3c). The orientation of the major and minor principal axes of the cross section located at the geometric center (gc), z' and y', is defined by the angle α. When subjected to bending, the two plates displace in axial, transversal and normal directions, except at the supports, where the section is only free to rotate, since simply supported conditions are imposed. Figure 4.8 shows the angle section and the adopted reference systems.

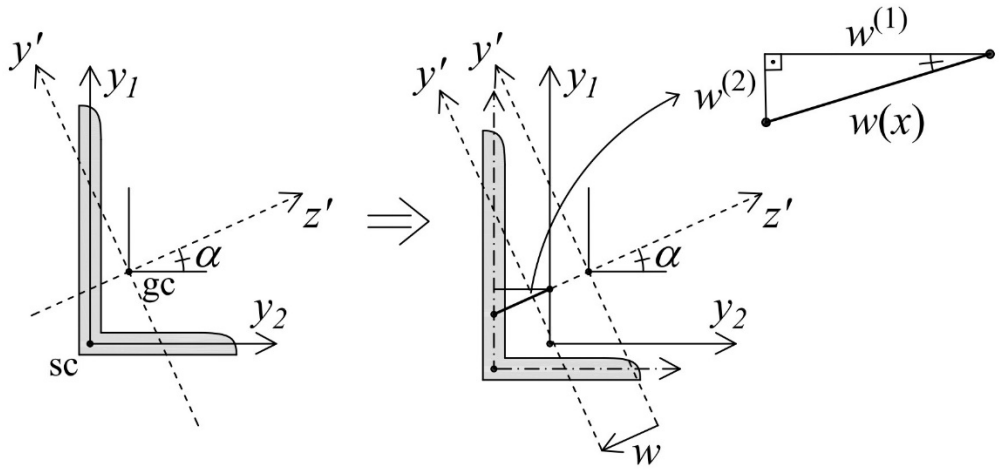

Figure 4.8 - Angle section in minor axis bending mode.

Bending about the minor axis promotes different in-plane displacements in each plate. In the absence of local plate buckling and considering the local coordinate system of each plate and the compatibility constraints, the in-plane displacement, *v*, in the *y* direction in one of the plates is equal to the transversal displacement, *w*, in the other plate. Thus, for a simply-supported column the variation of the transversal displacement *w* and in-plane displacements *v* in the *x* direction can be written as:

$$\begin{aligned} w_{mb}^{(1)}(x) &= v_{mb}^{(2)}(x) = C_k \sin(\pi x/L)\cos\alpha \\ w_{mb}^{(2)}(x) &= v_{mb}^{(1)}(x) = C_k \sin(\pi x/L)\sin\alpha \end{aligned} \tag{4.8}$$

in which the subscript *mb* designates minor axis bending, the superscript denotes the plate and the angle α is given by:

$$\alpha = \frac{1}{2}\arctan\left(-\frac{2I_{yz}}{\left(I_y - I_z\right)}\right) \tag{4.9}$$

where I_y and I_z are the moments of inertia about the *Y* and *Z* global axes and I_{yz} is the respective product of inertia. For a simply-supported plate the higher buckling and vibration modes can be obtained considering $g(x) = \sin(m\pi x/L)$, where *m* indicates the number of axial half-waves.

The axial displacements along the minor principal axis *y*' are zero and constant along any other parallel axis, as illustrated in Figure 4.9. Thus, it is a linear function of the major axis coordinate *z*'. Based on the classical plate theory hypotheses, the axial displacements take the form:

$$u_{mb}\left(x, z'\right) = -C_j \cos\left(\pi x / L\right) z' \tag{4.10}$$

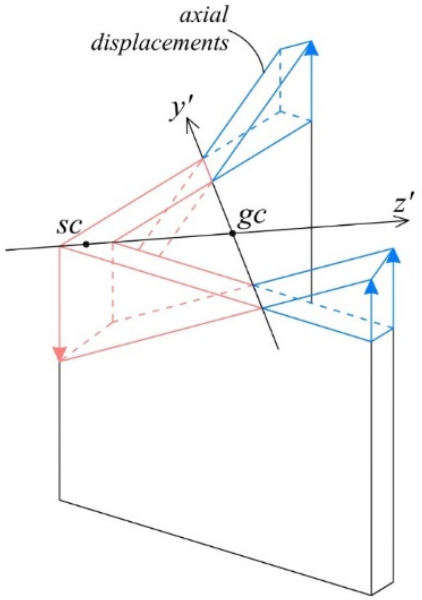

Figure 4.9 - Axial displacements due to minor axis bending.

In order to obtain the axial displacements in terms of the local coordinates of plates 1 and 2, y_1 and y_2, an auxiliary axis $\bar{z}$ parallel to the major principal axis z' and passing through the shear center (sc) is adopted, as illustrated in Figure 4.10. The distance between the geometric and shear centers in the $\bar{z}$ direction is given by:

$$d_z = \left(z_{gc} / \cos\alpha\right) + \left(y_{gc} - z_{gc} \tan\alpha\right) \sin\alpha \tag{4.11}$$

in which z_{gc} and y_{gc} are the geometric center coordinates (see Figure 3.3c).

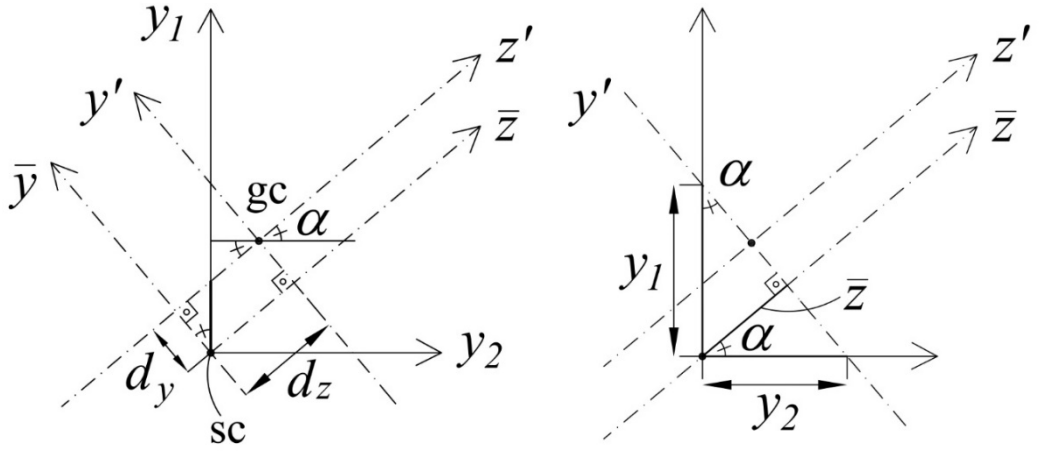

Figure 4.10 - (a) Auxiliary axes $\bar{y}$ and $\bar{z}$ on the shear center. (b) Local axial displacement components.

Hence, the axial displacements can be written in terms of the coordinate $\bar{z}$ as:

$$u_{mb}\left(x,\bar{z}\right) = -C_j \cos\left(\pi x/L\right)\left(\bar{z} - d_z\right) \tag{4.12}$$

Thus, the axial displacements in each plate can be written in terms of the local coordinate reference system (y_1, y_2), taking into account the relations $y_1 = \bar{z}/\sin\alpha$ and $y_2 = \bar{z}/\cos\alpha$ (see Figure 4.10b), as:

$$\begin{aligned} u_{mb}^{(1)}\left(x,y_1\right) &= C_j \cos\left(\pi x/L\right)\left(y_1 \sin\alpha - d_z\right) \\ u_{mb}^{(2)}\left(x,y_2\right) &= C_j \cos\left(\pi x/L\right)\left(y_2 \cos\alpha - d_z\right) \end{aligned} \tag{4.13}$$

Finally, from eqs. (4.8), (4.11) and (4.13), the resulting shape functions for the displacement field of plates 1 and 2 due to minor axis bending, denoted respectively by $\zeta_{mb}^{(1)}$ and $\zeta_{mb}^{(2)}$, are written as:

$$\zeta_{mb}^{(1)} \begin{cases} u_{mb}^{(1)}\left(x,y_1\right) = C_1 \cos\left(\pi x/L\right)\left\{y_1 \sin\alpha - \left[z_{gc}/\cos\alpha + \left(y_{gc} - z_{gc}\tan\alpha\right)\sin\alpha\right]\right\} \\ v_{mb}^{(1)}\left(x\right) = C_2 t \sin\left(\pi x/L\right)\sin\alpha \\ w_{mb}^{(1)}\left(x\right) = C_2 t \sin\left(\pi x/L\right)\cos\alpha \end{cases}$$

$$\zeta_{mb}^{(2)} \begin{cases} u_{mb}^{(2)}\left(x,y_2\right) = C_1 \cos\left(\pi x/L\right)\left\{y_2 \cos\alpha - \left[z_{gc}/\cos\alpha + \left(y_{gc} - z_{gc}\tan\alpha\right)\sin\alpha\right]\right\} \\ v_{mb}^{(2)}\left(x\right) = C_2 t \sin\left(\pi x/L\right)\cos\alpha \\ w_{mb}^{(2)}\left(x\right) = C_2 t \sin\left(\pi x/L\right)\sin\alpha \end{cases}$$

(4.14)

Thus, a 2dof ROM is obtained where C_1 and C_2 are the modal amplitudes. Here, to render the in-plane amplitudes C_2 dimensionless, they are multiplied by the thickness of the plates (t).

4.3.2
Major axis bending mode

Considering major axis bending, see Figure 4.11, the variation of the transversal displacement w and in-plane displacement v in the x direction can be written as:

$$\begin{aligned} w_{Mb}^{(1)}(x) &= v_{Mb}^{(2)}(x) = w(x)\sin\alpha = C_k \sin(\pi x/L)\sin\alpha \\ w_{Mb}^{(2)}(x) &= v_{Mb}^{(1)}(x) = w(x)\cos\alpha = C_k \sin(\pi x/L)\cos\alpha \end{aligned} \tag{4.15}$$

in which the subscript *Mb* means major axis bending.

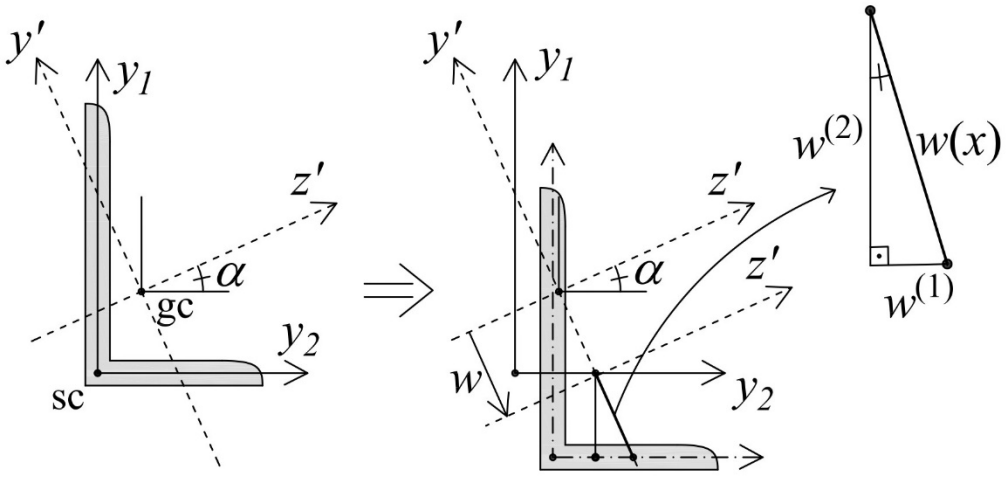

Figure 4.11 - Angle section in major axis bending mode.

The axial displacements due to major axis bending are obtained as a function of the coordinate *y*' of the minor principal axis, similar to eq. (4.10). Figure 4.10a also shows the auxiliary axis $\bar{y}$ parallel to the minor principal axis *y*' and passing through the shear center (sc), which can be used to provide the axial displacements in terms of the local coordinates of plates 1 and 2, y_1 and y_2. The distance between the geometric and shear centers projected on the $\bar{y}$ axis is given by:

$$d_y = \left(y_{gc} - z_{gc}\tan\alpha\right)\cos\alpha \tag{4.16}$$

In this case, the axial displacements are null along the principal major axis (z') and constant along any other parallel axis. Similar to the previous case, any axial displacement at a specific coordinate $\bar{y}$ is equivalent to the corresponding displacements at y_1 and y_2. Considering the relations $y_1 = \bar{y}/\cos\alpha$ and $y_2 = \bar{y}/\sin\alpha$, one obtains:

$$\begin{aligned} u_{Mb}^{(1)}(x, y_1) &= C_j \cos(\pi x/L)\left(y_1\cos\alpha - d_y\right) \\ u_{Mb}^{(2)}(x, y_2) &= C_j \cos(\pi x/L)\left(y_2\sin\alpha - d_y\right) \end{aligned} \tag{4.17}$$

Hence, by combining eqs. (4.15), (4.16), and (4.17), the resulting shape functions for the displacement field of the two plates due to major axis bending are written as follows:

$$\zeta_{Mb}^{(1)}\begin{cases} u_{Mb}^{(1)}(x,y_1) = C_3\cos(\pi x/L)\left[\, y_1\cos\alpha - \left(y_{gc} - z_{gc}\tan\alpha\right)\cos\alpha\,\right] \\ v_{Mb}^{(1)}(x) = C_4 t\sin(\pi x/L)\cos\alpha \\ w_{Mb}^{(1)}(x) = C_4 t\sin(\pi x/L)\sin\alpha \end{cases}$$

$$\zeta_{Mb}^{(2)}\begin{cases} u_{Mb}^{(2)}(x,y_2) = C_3\cos(\pi x/L)\left[\, y_2\sin\alpha - \left(y_{gc} - z_{gc}\tan\alpha\right)\cos\alpha\,\right] \\ v_{Mb}^{(2)}(x) = C_4 t\sin(\pi x/L)\sin\alpha \\ w_{Mb}^{(2)}(x) = C_4 t\sin(\pi x/L)\cos\alpha \end{cases} \tag{4.18}$$

where $\zeta_{Mb}^{(1)}$ and $\zeta_{Mb}^{(2)}$ denote the displacement fields of plates 1 and 2, respectively. Thus, again, a 2dof ROM is obtained where C_3 and C_4 are the modal amplitudes. Again, the in-plane amplitude C_4 is nondimensionalized with respect to the plates' thickness.

4.3.3
Torsional mode

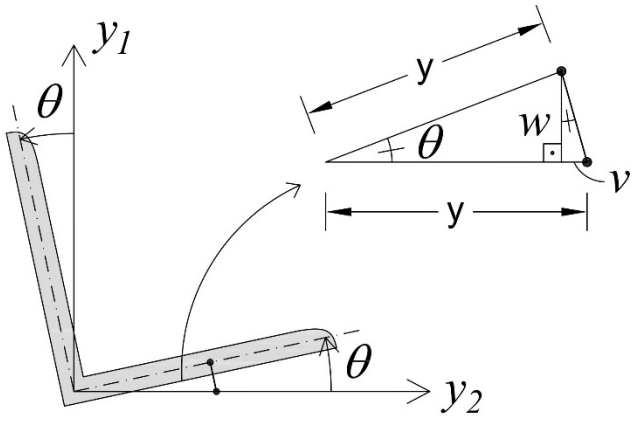

Figure 4.12 - Angle section in torsional mode.

Figure 4.12 shows the angle section after the torsional deformation with respect to the coordinate system (y_1, y_2). Both legs rotate with equal angular amplitudes. Considering small rotation, the in-plane displacement v is neglected ($v \propto (1 - cos\theta)$) and the transversal displacement field due to torsion is linear in y_1 and y_2. Thus, in the linear analyses, the displacement field of each plate, $\zeta_t^{(1)}$ and $\zeta_t^{(2)}$, takes the form:

$$\zeta_t^{(1)}\begin{cases} u_t^{(1)} = 0 \\ v_t^{(1)} = 0 \\ w_t^{(1)}\left(x, y_1\right) = C_5 t \sin\left(\pi x/L\right)\left(y_1/b_1\right) \end{cases}$$
$$\zeta_t^{(2)}\begin{cases} u_t^{(2)} = 0 \\ v_t^{(2)} = 0 \\ w_t^{(2)}\left(x, y_2\right) = C_5 t \sin\left(\pi x/L\right)\left(y_2/b_2\right) \end{cases} \tag{4.19}$$

where the subscript t denotes torsion, and C_5 is the torsional amplitude. The y_i coordinate is normalized by the respective plate width b_i, such that $0 \leq (y_i/b_i) \leq 1$. If the local plate mode is to be considered, the linear functions y_i should be substitute by polynomials similar to those in Figure 4.1a. Usually a cubic polynomial can describe with precision the deformed shape in each leg (Bebiano et al., 2018; Gonçalves et al., 2010; Bebiano et al., 2015; Gonçalves et al., 2023), with the coefficients dependent on the section geometry, leading again to a sdof ROM.

In the nonlinear analyses, non-zero displacements u and v are considered for the torsional model to consider the nonlinear relation between the in-plane displacements and the quadratic terms involving the transversal displacement, w, as shown in eq. (3.18) and (3.19). The compatibility is guaranteed by assuming twice the number of longitudinal half-waves for the harmonic functions in u and v. From the transverse displacements (w_t) and eq. (3.18) and (3.19), the nonlinear torsional ROM results in (Coaquira, 2020):

$$\zeta_t^{(1)}\begin{cases} u_t^{(1)}\left(x, y_1\right) = C_6 t \sin\left(2\pi x/L\right)\left(y_1^2/b_1^2\right) \\ v_t^{(1)}\left(x, y_1\right) = C_7 t \cos\left(2\pi x/L\right)\left(y_1/b_1\right) \\ w_t^{(1)}\left(x, y_1\right) = C_5 t \sin\left(\pi x/L\right)\left(y_1/b_1\right) \end{cases}$$
$$\zeta_t^{(2)}\begin{cases} u_t^{(2)}\left(x, y_2\right) = C_6 t \sin\left(2\pi x/L\right)\left(y_2^2/b_2^2\right) \\ v_t^{(2)}\left(x, y_2\right) = C_7 t \cos\left(2\pi x/L\right)\left(y_2/b_2\right) \\ w_t^{(2)}\left(x, y_2\right) = C_5 t \sin\left(\pi x/L\right)\left(y_2/b_2\right) \end{cases} \tag{4.20}$$

Since the displacement fields were deduced with regard to the local coordinate system, the expressions for plates 1 and 2 satisfy the compatibility at the common boundary for each mode, resulting in low-dimensional models for the minor axis bending mode $\zeta_{mb}(x, y)$, the major axis bending mode $\zeta_{Mb}(x, y)$ and the torsional mode $\zeta_t(x, y)$. The ROMs incorporating flexural-torsional deformations

are obtained by considering the sum of the corresponding shape functions. Thus, the minor-axis flexural-torsional ROM will be designated as $\zeta_{mb}(x, y) + \zeta_t(x, y)$ and the major-axis flexural-torsional ROM as $\zeta_{Mb}(x, y) + \zeta_t(x, y)$. Introducing the displacement fields into eq. (3.17) and employing the Ritz method, a system of up to five coupled nonlinear ordinary equations of motion is obtained.

5
Critical Loads and Natural Frequencies

In this chapter, the reduced-order models (ROMs) developed in Chapter 4 are employed to carry out the linear analyses for pultruded angle section profiles. The influence of geometric and physical properties on critical loads and natural frequencies is investigated, considering the appropriate modal participation in each case.

For equal-leg short-to-intermediate lengths angle section profiles, despite their stability being guided by the major-axis flexural-torsional ROM ($\zeta_{Mb}+\zeta_t$), linear results are also obtained for the pure torsional ROM (ζ_t), since the torsional mode plays a predominant role in the first buckling and vibration mode of these profiles. This allows to assess situations in which the uncoupled ROM provides a good approximation, leading to a reduction in computational effort in nonlinear analyses. On the other hand, unequal-leg profiles exhibit significant participation of the minor-axis flexural-torsional mode, requiring the use of the coupled ROM ($\zeta_{mb}+\zeta_t$). The pure bending ROM (ζ_{mb}) is found to play an important role in very long angle profiles.

5.1
Eigenvalue problem

Substituting the harmonic function $e^{i\omega_0 t}$ into the linearized equations of motion, a system of homogeneous algebraic equations is obtained, resulting in the desired eigenvalue problem. In this section, the linear eigenvalue problem for buckling and vibration analysis is presented for each ROM. In order to obtain the critical loads per unit length (N_{cr}) and natural frequencies (ω_0), the following eigenvalue problem is solved:

$$\left[\mathbf{K} - N_{cr}\mathbf{K_G} - \omega_0^2\mathbf{M}\right]\mathbf{C} = 0 \tag{5.1}$$

where **K** and $\mathbf{K_G}$ are the stiffness and geometric matrices, respectively, **M** is the mass matrix and **C** is the displacement vector which contains the modal amplitudes. The critical load is given by:

$$P_{cr} = N_{cr}\left(b_1 + b_2\right) \tag{5.2}$$

5.1.1
Torsional mode

Considering only the torsional mode ζ_t, eq. (4.1) reduces to a single-degree-of-freedom (sdof) system and the vector **C** is equal to the torsional amplitude C_5. The stiffness, geometric and mass coefficients are given by:

$$K_t = \frac{\pi^4}{6L^3}\left(b_1^3 + b_2^3\right)D_{11} + \frac{2\pi^2}{L}\left(b_1 + b_2\right)D_{66} \tag{5.3}$$

$$K_{Gt} = \frac{\pi^2}{6L}\left(b_1^3 + b_2^3\right) \tag{5.4}$$

$$M_t = \frac{\rho tL}{6}\left(b_1^3 + b_2^3\right) \tag{5.5}$$

Thus, the critical load and fundamental frequency are given respectively by:

$$N_{cr} = \frac{\pi^2 E_1 t^3}{12(1-\nu_{12}\nu_{21})L^2} + \frac{t^3}{L^2}\frac{\left(1+\beta\right)}{\varphi^2\left(1+\beta^3\right)}G_{12} \tag{5.6}$$

$$\omega_0^2 = \frac{\pi^4 E_1 t^2}{12(1-\nu_{12}\nu_{21})\rho L^4} + \frac{\pi^2 t^2}{\rho L^4}\frac{\left(1+\beta\right)}{\varphi^2\left(1+\beta^3\right)}G_{12} \tag{5.7}$$

These analytical expressions show clearly the influence of material and geometric parameters on the buckling and vibration of pultruded angle section profiles. They also show that there is a linear relation between the applied load, N_x, and the square of the fundamental frequency, ω_0, with the fundamental frequency decreasing with the compressive load and becoming zero at $N_x = N_{cr}$. It was observed that the modal participation of the vibration mode is not affected by the compressive load level.

5.1.2
Minor axis bending mode

A 2dof ROM is obtained. The vector **C** is given by $[C_1, C_2]^T$, and the symmetric stiffness, geometric and mass matrices are given in eqs. (5.8), (5.9) and (5.10), respectively.

For the particular case of minor axis bending, considering the plane section hypothesis of the classical plate theory, the constraint $C_1 = -(C_2\pi/L)$ between the modal amplitudes can be imposed reducing the model to a sdof ROM.

The critical load and fundamental frequency for the minor axis bending mode, considering equal-leg profiles ($b_1 = b_2 = b$) can be written respectively as:

$$P_{cr} = \frac{1}{12}\frac{\pi^2 E_1 tb\left(2t^2 + b^2\right)}{L^2\left(1-\nu_{12}\nu_{21}\right)} \tag{5.8}$$

$$\omega_0^2 = \frac{\pi^4 E_1\left(t^2 + b^2\right)}{L^2\rho\left(\pi^2 b^2 + 24L^2\right)\left(1-\nu_{12}\nu_{21}\right)} \tag{5.9}$$

$$\mathbf{K_{mb}} = \begin{bmatrix} \frac{\pi^2}{2L}\left(\frac{c^2 b_2^3}{3} - \frac{c^2 b_1^3}{3} + \frac{b_1^3}{3} + b_1 d_z^2 + b_2 d_z^2 - s b_1^2 d_z - c b_2^2 d_z\right) A_{11} + \frac{L}{2}\left(b_1 s^2 + b_2 c^2\right) A_{66} & \frac{\pi}{2}\left(b_1 s^2 + b_2 c^2\right) A_{66} \\ \frac{\pi}{2}\left(b_1 s^2 + b_2 c^2\right) A_{66} & \frac{\pi^2}{2L}\left(b_1 s^2 + b_2 c^2\right) A_{66} + \frac{\pi^4}{2L^3}\left(b_2 s^2 + b_1 c^2\right) D_{11} \end{bmatrix} \tag{5.10}$$

$$\mathbf{K_{Gmb}} = \begin{bmatrix} 0 & 0 \\ 0 & \frac{\pi^2}{2L}\left(b_2 s^2 + b_1 c^2\right) \end{bmatrix} \tag{5.11}$$

$$\mathbf{M_{mb}} = \begin{bmatrix} \frac{\rho t L}{2}\left(-c b_2^2 d_z - s b_1^2 d_z + \frac{1}{3} c^2 b_2^3 - \frac{1}{3} c^2 b_1^3 + b_2 d_z^2 + b_1 d_z^2 + \frac{1}{3} b_1^3\right) & 0 \\ 0 & \frac{\rho t L}{2}\left(b_1 + b_2\right) \end{bmatrix} \tag{5.12}$$

where c and s denote $\cos(\alpha)$ and $\sin(\alpha)$, respectively.

5.1.3
Flexural-torsional mode considering minor axis bending

Considering the coupling between torsion and minor axis bending ($\zeta_{mb}+\zeta_t$), one obtains a 3dof ROM, in which the vector **C** is given by $[C_1, C_2, C_5]^T$. The symmetric stiffness, geometric and mass matrices are given by eqs. (5.13), (5.14) and (5.15), respectively.

It can be observed that most coefficients are similar to those obtained from pure torsional and pure minor axis bending eigenvalue problems, as previously specified, with the exception being the presence of coupling coefficients in the matrix elements with subindex 23.

5.1.4
Flexural-torsional mode considering major axis bending

Finally, considering the coupling of torsion with major axis bending ($\zeta_{Mb}+\zeta_t$), also results in a 3dof ROM, with **C** = $[C_3, C_4, C_5]^T$. The stiffness, geometric and mass matrices are given by eqs. (5.16), (5.17) and (5.18), respectively.

By using the above ROMs, the influence of geometric and physical parameters on critical loads and natural frequencies can now be studied and the results compared to those from the GBTul software.

$$\mathbf{K_{mb+t}} = \begin{bmatrix} \frac{\pi^2}{2L}\left(\frac{c^2b_2^3}{3}-\frac{c^2b_1^3}{3}+\frac{b_1^3}{3}+b_1d_z^2+b_2d_z^2-sb_1^2d_z-cb_2^2d_z\right)A_{11}+\frac{L}{2}\left(b_1s^2+b_2c^2\right)A_{66} & \frac{\pi}{2}\left(b_1s^2+b_2c^2\right)A_{66} & 0 \\ \frac{\pi}{2}\left(b_1s^2+b_2c^2\right)A_{66} & \frac{\pi^2}{2L}\left(b_1s^2+b_2c^2\right)A_{66}+\frac{\pi^4}{2L^3}\left(b_2s^2+b_1c^2\right)D_{11} & \frac{\pi^4}{4L^3}\left(cb_1^2+sb_2^2\right)D_{11} \\ 0 & \frac{\pi^4}{4L^3}\left(cb_1^2+sb_2^2\right)D_{11} & K_t \end{bmatrix} \tag{5.13}$$

$$\mathbf{K_{Gmb+t}} = \begin{bmatrix} 0 & 0 & 0 \\ 0 & \frac{\pi^2}{2L}\left(b_2s^2+b_1c^2\right) & \frac{\pi^2}{4L}\left(cb_1^2+sb_2^2\right) \\ 0 & \frac{\pi^2}{4L}\left(cb_1^2+sb_2^2\right) & K_{Gt} \end{bmatrix} \tag{5.14}$$

$$\mathbf{M_{mb+t}} = \begin{bmatrix} \frac{\rho tL}{2}\left(-cb_2^2d_z-sb_1^2d_z+\frac{1}{3}c^2b_2^3-\frac{1}{3}c^2b_1^3+b_2d_z^2+b_1d_z^2+\frac{1}{3}b_1^3\right) & 0 & 0 \\ 0 & \frac{\rho tL}{2}\left(b_1+b_2\right) & \frac{\rho tL}{4}\left(cb_1^2+sb_2^2\right) \\ 0 & \frac{\rho tL}{4}\left(cb_1^2+sb_2^2\right) & M_t \end{bmatrix} \tag{5.15}$$

where K_t, K_{Gt} and M_t are the torsional coefficients defined in eqs. (5.3), (5.4) and (5.5).

$$\mathbf{K_{Mb+t}} = \begin{bmatrix} \frac{\pi^2}{2L}\left(-\frac{c^2b_2^3}{3}+\frac{c^2b_1^3}{3}+\frac{b_2^3}{3}+b_1d_y^2+b_2d_y^2-cb_1^2d_y-sb_2^2d_y\right)A_{11}+\frac{L}{2}\left(b_2s^2+b_1c^2\right)A_{66} & \frac{\pi}{2}\left(b_2s^2+b_1c^2\right)A_{66} & 0 \\ \frac{\pi}{2}\left(b_2s^2+b_1c^2\right)A_{66} & \frac{\pi^2}{2L}\left(b_2s^2+b_1c^2\right)A_{66}+\frac{\pi^4}{2L^3}\left(b_1s^2+b_2c^2\right)D_{11} & \frac{\pi^4}{4L^3}\left(sb_1^2+cb_2^2\right)D_{11} \\ 0 & \frac{\pi^4}{4L^3}\left(sb_1^2+cb_2^2\right)D_{11} & Kt \end{bmatrix} \tag{5.16}$$

$$\mathbf{K_{GMb+t}} = \begin{bmatrix} 0 & 0 & 0 \\ 0 & \frac{\pi^2}{2L}\left(b_1s^2+b_2c^2\right) & \frac{\pi^2}{4L}\left(sb_1^2+cb_2^2\right) \\ 0 & \frac{\pi^2}{4L}\left(sb_1^2+cb_2^2\right) & K_{Gt} \end{bmatrix} \tag{5.17}$$

$$\mathbf{M_{Mb+t}} = \begin{bmatrix} \frac{\rho tL}{2}\left(-cb_1^2d_y-sb_2^2d_y+\frac{1}{3}c^2b_1^3-\frac{1}{3}c^2b_2^3+b_2d_y^2+b_1d_y^2+\frac{1}{3}b_2^3\right) & 0 & 0 \\ 0 & \frac{\rho tL}{2}\left(b_1+b_2\right) & \frac{\rho tL}{4}\left(sb_1^2+cb_2^2\right) \\ 0 & \frac{\rho tL}{4}\left(sb_1^2+cb_2^2\right) & M_t \end{bmatrix} \tag{5.18}$$

5.2
Dimensional results

Figure 5.1 shows the variation of the critical loads as a function of the column length for the angle sections L 150x150x5 ($\beta = 1.0$) and L 150x75x5 ($\beta = 0.5$), for which the modal participations are shown in Figure 4.3. For the equal-leg section ($\beta = 1.0$), the results from the coupled ROM ($\zeta_{Mb}+\zeta_t$) yield the same outcomes as GBTul. Due to the low contribution of the major axis bending mode in this case, as observed in Figure 4.3a, the results considering the pure torsional (ζ_t) ROM are close to the ones provided by the coupled ROM for short columns but leads to higher critical loads for long columns, with the difference increasing with the column length, also in agreement with Figure 4.3a, where a small increase in the participation of the major axis bending mode is observed as L increases.

On the other hand, for the unequal-leg profile ($\beta = 0.5$), the ($\zeta_{mb}+\zeta_t$) ROM considering torsion plus minor axis bending can adequately describe the solution provided by GBTul. The pure torsional ROM and the flexural-torsional ROM considering major axis bending present the same behavior as in the previous case, but overestimates the critical load and the difference increases with L due to the increasing contribution of the minor axis bending mode as the profile length increases, in agreement with Figure 4.3b. The variation of the fundamental frequency as a function of the column length is shown in Figure 5.2 considering the same profiles. For the equal-leg section ($\beta = 1.0$), both the torsional and the torsional plus major axis bending ROMs show excellent agreement with the GBTul results for any value of L, thus eq. (4.7) can be used successfully. For the unequal-leg section ($\beta = 0.5$), the flexural-torsional ROM considering minor axis bending ($\zeta_{mb}+\zeta_t$) agrees quite well with the GBTul results, while the other ROMs lead to slightly higher frequency values. These results show the importance of considering the adequate ROM when determining the linear response of the system. For both sections, the frequency displays a hyperbolic variation with the column length. Comparing Figure 5.1b and Figure 5.2b, although the modal participation is the same in both cases, it is observed that the flexural-torsional coupling considering

minor axis bending ($\zeta_{mb}+\zeta_t$) is much stronger in the buckling case, leading to much lower critical loads.

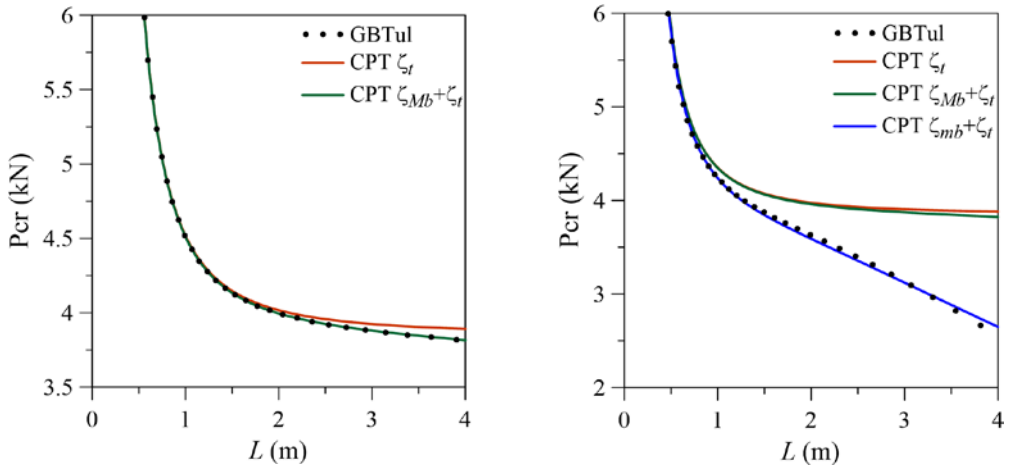

(a) L 150x150x5 (β = 1.0) (b) L 150x75x5 (β = 0.5)

Figure 5.1 - Critical loads as a function of the column length for the angle sections.

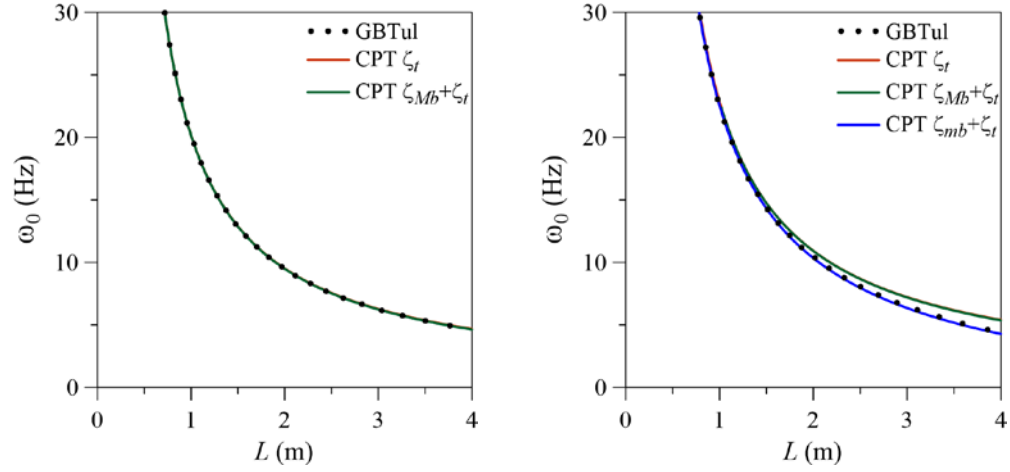

(a) L 150x150x5 (β = 1.0) (b) L 150x75x5 (β = 0.5)

Figure 5.2 - Natural frequencies as a function of the column length for the angle sections.

Usually only the lowest bifurcation load (critical load) is necessary for design, unless coincident or nearly coincident buckling loads are observed. However, in dynamic analyses higher modes may be necessary to identify the higher resonance regions. As stated previously, for a simply-supported plate, the higher buckling and vibration modes can be obtained considering $g(x) = \sin(m\pi x/L)$, where m is the number of axial half-waves.

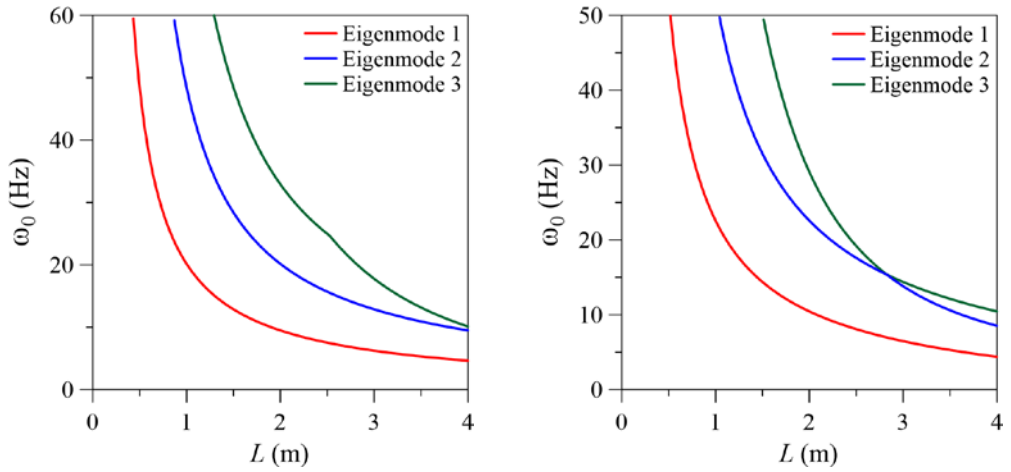

(a) L 150x150x5 (β = 1.0) (b) L 150x75x5 (β = 0.5)

Figure 5.3 - The three lowest natural frequencies as a function of the column length for the angle sections.

The variation of the three lowest natural frequencies as a function of the column length is shown in Figure 5.3a for the L 150x150x5 section and in Figure 5.3b for the L 150x75x5 section. The modal participation of each mode is shown in Figure 5.4 for the L 150x150x5 section and in Figure 5.5 for the L 150x75x5 section. The difference between the frequencies increases as L decreases, thus being the resonant peaks well separated. In both cases the change in modal participation increases in complexity as the mode number increase. For the equal-leg L 150x150x5 profile, the first mode, as shown previously, is dominated by the torsional mode with a small percentage of the major axis bending mode for all values of L. The second mode already presents a modal participation transition at L_t = 0.75 m. For short columns the local plate mode is dominant but a small participation of the minor axis bending mode is observed. For L > 0.75 m the modal participation is the same observed for the 1st mode, with $\omega_{02} \approx 2\omega_{01}$. The third mode, on the other hand, display several discontinuities in modal content. Initially, for short columns (L < 0.75m), the torsional mode is dominant but a negligible participation of the major axis bending mode is observed. For intermediate columns, in the interval 0.75m < L < 1.26 m, the dominant local plate mode decreases with L, while the minor axis bending mode increases up to the next transition point at L_t = 2.52 m. For intermediate columns, in the interval 1.26 m < L < 2.52 m, a purely torsional mode is observed. However, for L > 2.52 m, the minor axis bending mode dominance increases from 93% with L

while the small participation of the local mode decreases. This change in modal composition is observed as a kink in the green curve, Figure 5.3. As observed, the frequencies decrease exponentially with L. So, for short profiles it is expected that these modes will be excited by usual environmental or human induced loads. For the unequal-leg profile, a similar scenario with increasing changes in modal participation with mode number is also observed, as shown in Figure 5.5. However, the dominant modes in each interval are quite distinct from the equal-leg case, emphasizing again the importance of the geometric parameter $\beta = b_2/b_1$ on the results.

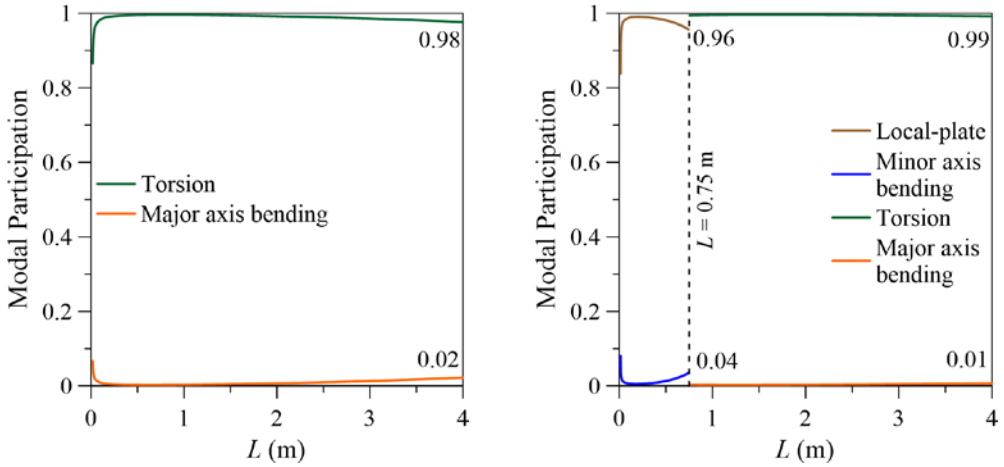

(a) 1st vibration mode

(b) 2nd vibration mode

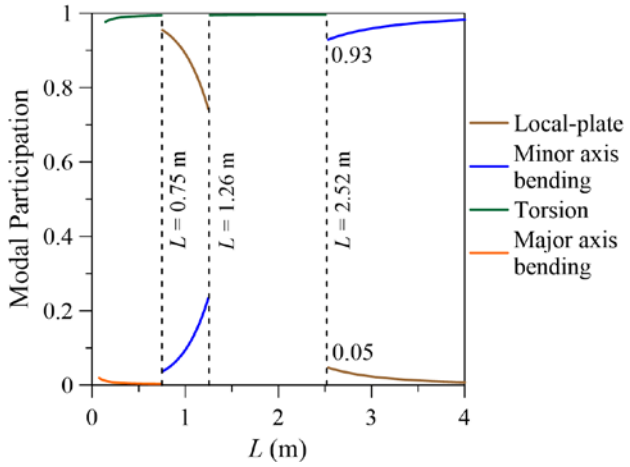

(c) 3rd vibration mode

Figure 5.4 - Variation of the Modal participation for the first three vibration modes of the angle section L 150x150x5 (β = 1.0).

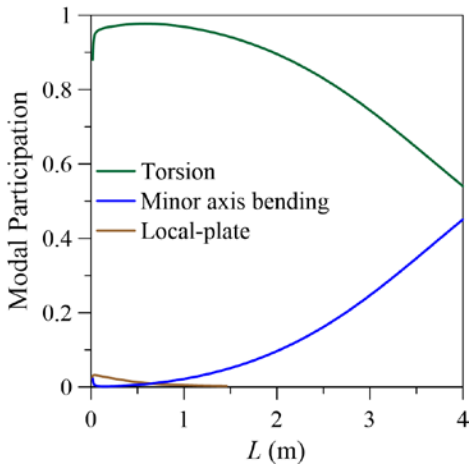

(a) 1st vibration mode

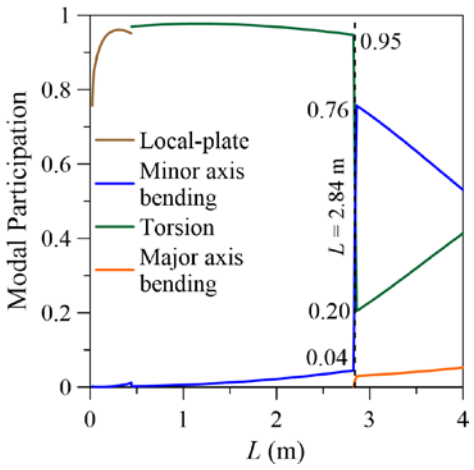

(b) 2nd vibration mode

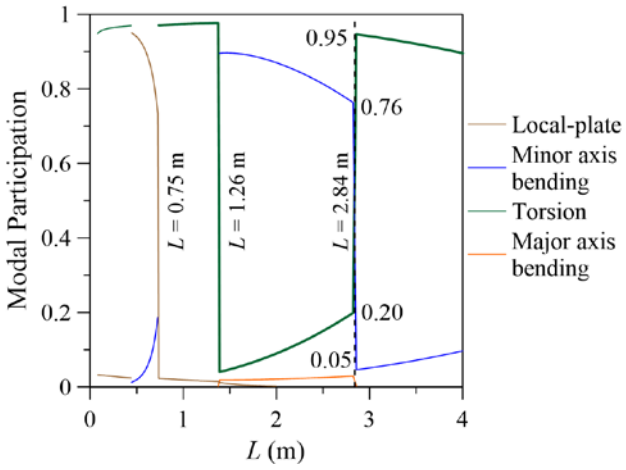

(c) 3rd vibration mode

Figure 5.5 - Variation of the Modal participation for the first three vibration modes of the angle section L 150x75x5 ($\beta = 0.5$).

As shown in Figure 4.5 and corroborated by the previous results, the geometric parameter $\beta = b_2/b_1$ has an important influence on the modal participation. Figure 5.6 shows the GBTul results from 3 ROMs as a function of the leg width b_2 for a column with intermediate length, L = 2.5 m, with the shorter leg varying between 50 mm and 150 mm ($b_2/t \geq 10$), keeping b_1 = 150 mm and t = 5 mm. It is observed in both cases that the flexural-torsional model considering minor axis bending leads to a lower bound of the results, in agreement with Figure 5.1b and Figure 5.2b for $\beta = 0.5$, while the flexural-torsional model considering major axis bending (which agrees with torsional ROM in this case) leads to an upper bound of the results. As β increases the GBTul results moves continuously from the

lower bound towards the upper bound, in agreement with Figure 4.5a. Also, the upper and lower bounds approach each other as $\beta \rightarrow 1$.

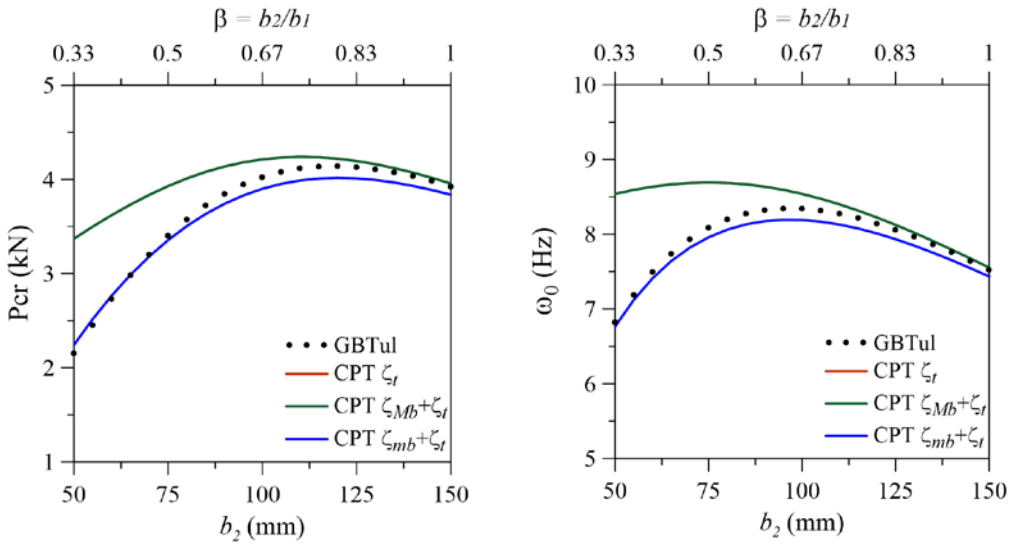

(a) Critical loads (b) Natural frequencies

Figure 5.6 - Influence of the geometrical parameter $\beta = b_2/b_1$ on the linear results for the angle section L 150xb_2x5 (L = 2.5 m).

Some equal-leg angle section profiles can exhibit abrupt transitions regarding the contribution of deformation modes, particularly less slender sections. Figure 5.7 presents the results for the equal-leg angle section L 75x75x5 as a function of the column length. As shown in Figure 4.6a, the discontinuity occurs at L_t = 2.32 m, φ_t = 0.032. For $L < L_t$, the (ζ_{Mb}+ζ_t) ROM compare quite well with the outcomes from GBTul software for both the critical load and fundamental frequency. On the other hand, after the transition length ($L > L_t$), the model considering purely minor axis bending (ζ_{mb}) agrees with the GBTul results up to L = 4 m. This change occurs when the curve obtained by the (ζ_{Mb}+ζ_t) ROM depicted in green intercepts the characteristic Euler hyperbola in black. The purely torsional ROM leads to reliable results for short columns (L < 0.5 m) but results in higher values for longer profiles. The influence of the modal content is particularly important in the evaluation of the critical loads, where the difference between different ROMs is substantial. The transition length where the change in modal content occurs decreases as the thickness to leg thickness to width ratio, $\xi = t/b$, increases, reaching the transition value of L_t = 1.02 m for the L 50x50x5 section, as illustrated in Figure 5.8. Thus, for a compact section, the critical load and natural frequency of intermediate to long

columns is expected to be governed mainly by the minor axis bending mode, as described by eqs. (5.11) and (5.12), which gives practically the same results as the global formulation for these profiles (Timoshenko & Gere, 2009). Although the modal participation displays a sudden change, the variation of the critical load and fundamental frequency is rather smooth around the transition point as shown by the signature curves.

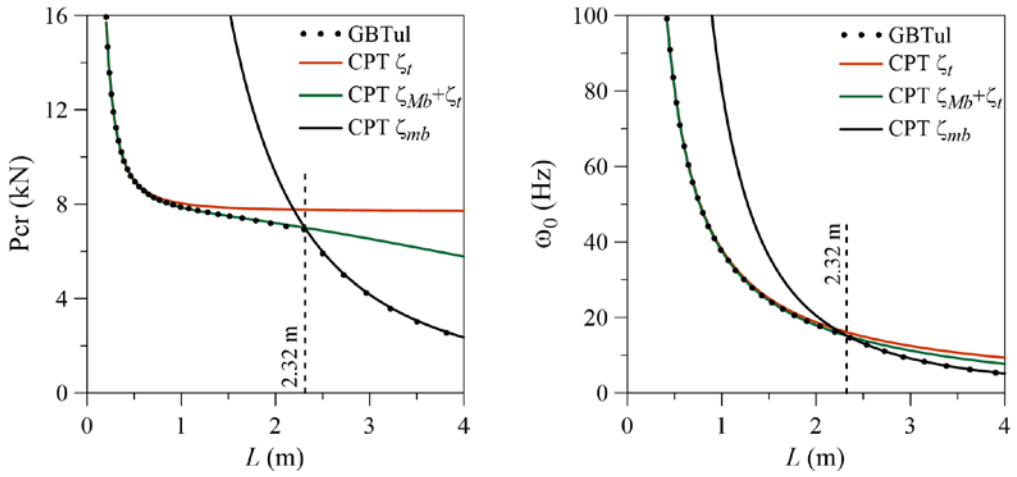

(a) Critical loads (b) Natural frequencies

Figure 5.7 - Linear results as a function of the column length for the angle section L 75x75x5 (β = 1.0).

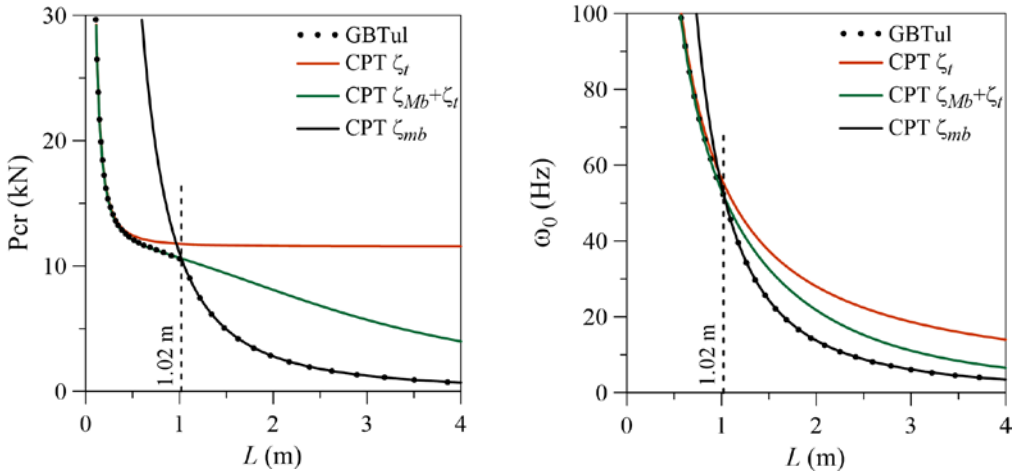

(a) Critical loads (b) Natural frequencies

Figure 5.8 - Linear results as a function of the column length for the angle section L 50x50x5 (β = 1.0).

The previous results for equal-leg angle profiles show that the thickness to leg width ratio ξ has a strong influence on the results. This can be observed in Figure 5.9, where the critical load and fundamental frequency are presented for equal-leg

angle sections as a function of the leg width, which varies from 35 mm to 200 mm ($b = b_1 = b_2$), assuming L = 4 m and maintaining t = 5 mm, ($\xi = 5/b$). As observed, equal-leg angle section profiles exhibit a distinctive behavior when b varies, considering all other parameters constant. As the leg width increases, the GBTul results increase until reaching a peak, where the curve slope abruptly changes sign, leading to a subsequent decrease in results as b continues to increase. This point coincides with the change from the ζ_{mb} mode to the (ζ_{Mb}+ζ_t) mode. Both the critical loads and natural frequencies can be obtained with accuracy using these ROMs. Thus, for a given set of parameters, there is an optimal critical leg width where the critical load and natural frequency attains a maximum value. Here both the maximum critical load and natural frequency occur for b_t = 100 mm. Before the peak value the minor axis bending mode is dominant. It is interesting to notice that for b < 100 mm, the critical load exhibits a quadratic variation but the variation of the fundamental frequency is linear. This is due to the linear relation between the applied load and the square of the frequency parameter, as mentioned previously. After the peak load, as ξ decreases, the desired value can be obtained with precision using the (ζ_{Mb}+ζ_t) ROM. The results considering the torsional ROM converge to those obtained with the (ζ_{Mb}+ζ_t) ROM as b increases beyond b_t. It should be pointed out that these modes may interact near the peak due to nonlinear modal coupling leading to imperfection sensitivity and decreasing the profile load capacity in the vicinity of the transition point (Gioncu, 1994; Hancock, 2018).

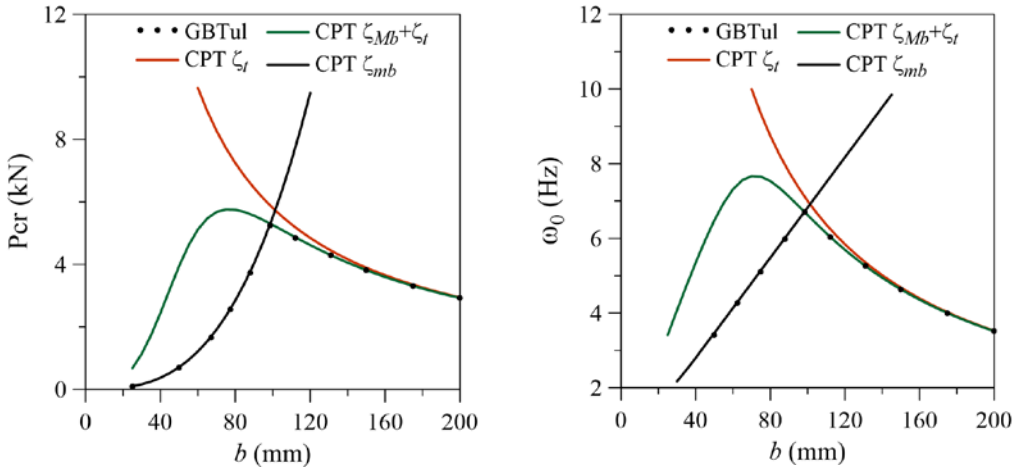

(a) Critical loads (b) Natural frequencies

Figure 5.9 - Linear results as a function of the leg width for equal-leg angle sections ($b = b_1 = b_2$, L = 4 m, t = 5 mm).

5.3
Nondimensional results

Although the dimensional analysis is able to shed light on the buckling and vibration of angle section profiles, it is worthwhile, given the number of variables, to understand the range of validity of each ROM. Aiming at clarifying these points, the eigenvalue problem stated in eq. (5.1) is rewritten in a dimensionless form in terms of geometric and physical nondimensional parameters. The previous analyses show that the leg width ratio ($\beta = b_2/b_1 \leq 1$), the wider plate dimensions ratio ($\varphi = b_1/L$), and the slenderness of the shorter plate given as the thickness to shorter width ratio ($\xi = t/b_2 \leq 1/10$) can describe completely the profile geometry. Alternatively, the parameter $\tau = \varphi\beta\xi = t/L$, which also represents a measure of the column slenderness can be used. Thus, three geometric nondimensional parameters can be used to define the entire geometry of any angle profile, being φ and τ slenderness measures.

With regard to the physical properties of the pultruded material, the nondimensional physical parameter is adopted as in eq. (4.6). For the material properties in Table 2.4, one obtains $\psi = 0.1068$, which will be used in all further analysis unless the influence of changes in the material parameter is investigated.

Substituting the defined dimensionless parameters into the stiffness, geometric and mass matrices, the following parameters are obtained for the nondimensional critical load and fundamental frequency parameter:

$$\Gamma_{cr} = \frac{P_{cr}\left(1-\nu_{12}\nu_{21}\right)}{\pi^2 E_1 L^2} \tag{5.19}$$

$$\Omega_0^2 = \frac{\omega_0^2 \rho L^2 \left(1-\nu_{12}\nu_{21}\right)}{\pi^2 E_1} \tag{5.20}$$

For the torsional mode, the nondimensional parameters are given by:

$$\Gamma_{cr} = \frac{1}{12}\frac{(1+\beta)\left(\pi^2\varphi^2 + 12\psi + \pi^2\varphi^2\beta^2 - \pi^2\varphi^2\beta\right)\beta^3\xi^3\varphi^2}{\pi^2\left(\beta^2 - \beta + 1\right)} \tag{5.21}$$

$$\Omega_0^2 = \frac{1}{12}\frac{\left(\pi^2\varphi^2 + 12\psi + \pi^2\varphi^2\beta^2 - \pi^2\varphi^2\beta\right)\beta^2\xi^2}{\left(\beta^2 - \beta + 1\right)} \tag{5.22}$$

where the material parameter and three geometrical parameters are observed. The relation $\tau = \varphi\beta\xi$ can also be used to simplify the above equations.

For the minor axis bending mode in equal-leg profiles ($\beta = 1.0$), the nondimensional parameters are given as follows:

$$\Gamma_{cr} = \frac{1}{12}\varphi^4\xi\left(2\xi^2 + 1\right) \tag{5.23}$$

$$\Omega_0^2 = \frac{\pi^2\varphi^2\left(1+\xi^2\right)}{\pi^2\varphi^2 + 24} \tag{5.24}$$

As one can see, in this case, there is no dependency on the material parameter; rather, it depends only on the geometric parameters. For the flexural-torsional ROMs, these expressions are lengthy and will not be shown herein, but can be easily calculated using symbolic algebra softwares and the explicit matrices given at the beginning of this chapter.

Figure 5.10 presents the nondimensional critical load and fundamental frequency parameters as a function of the wider plate aspect ratio $\varphi = b/L$ in the range of usual applications, first considering an equal-leg angle section ($\beta = 1{,}0$) and $\xi = t/b = 1/30$ (corresponding to the L 150x150x5 section case). The critical load decreases sharply as φ decreases from 0.1 (long leg/short column) to 0.02 (short leg/long column), while the fundamental frequency remains almost constant, decreasing slightly. In both cases the (ζ_{Mb}+ζ_t) ROM agrees with the GBTul results. Within the considered order of magnitude for the dimensionless parameters, the pure torsional ROM leads to reliable results for the critical loads but overestimate slightly the values of the fundamental frequency as φ decreases. These results agree with the modal participation in Figure 4.3a.

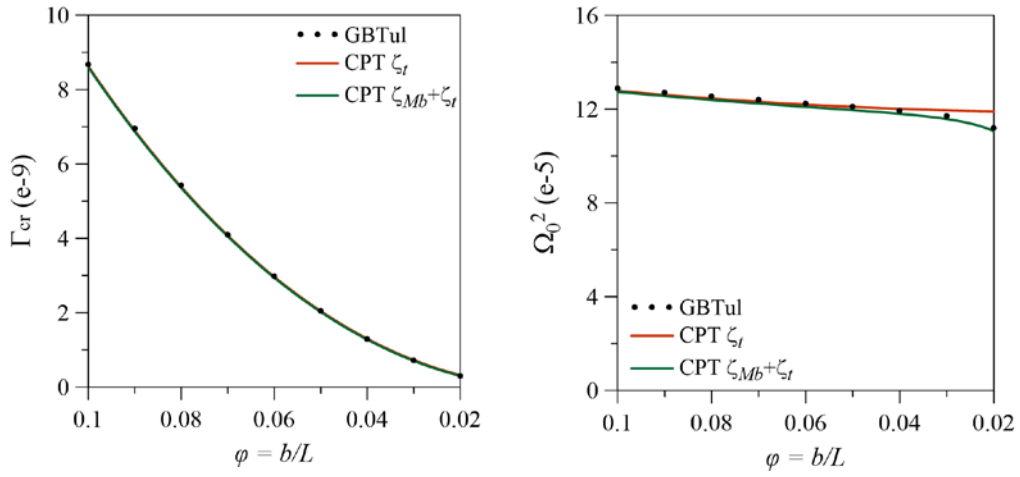

(a) Critical loads

(b) Fundamental frequencies

Figure 5.10 - Nondimensional parameters as a function of the aspect ratio φ (β = 1.0, ξ = 1/30).

It was observed in Figure 4.6, for the equal-leg angle section, that, depending on the geometric parameters, there is a sharp transition in the modal participation. Figure 5.11 presents the results for $\xi = t/b = 1/15$ (equivalent to the L 75x75x5 section case). The transition corresponds to the crossing of the green and black curves at $\varphi = 0.0322$. For $\varphi < 0.0322$ the flexural-torsional model considering major axis bending, (ζ_{Mb}+ζ_t) ROM, gives consistent results for both the critical load and fundamental frequency. For $\varphi > 0.0322$, after the transition point, there is a complete agreement between the minor axis bending mode (eqs. (5.23) and (5.24)) and the GBTul results. In both cases, the purely torsional ROM leads to higher values. As in previous results, there is a perceptible difference in the variation of critical load and fundamental frequency.

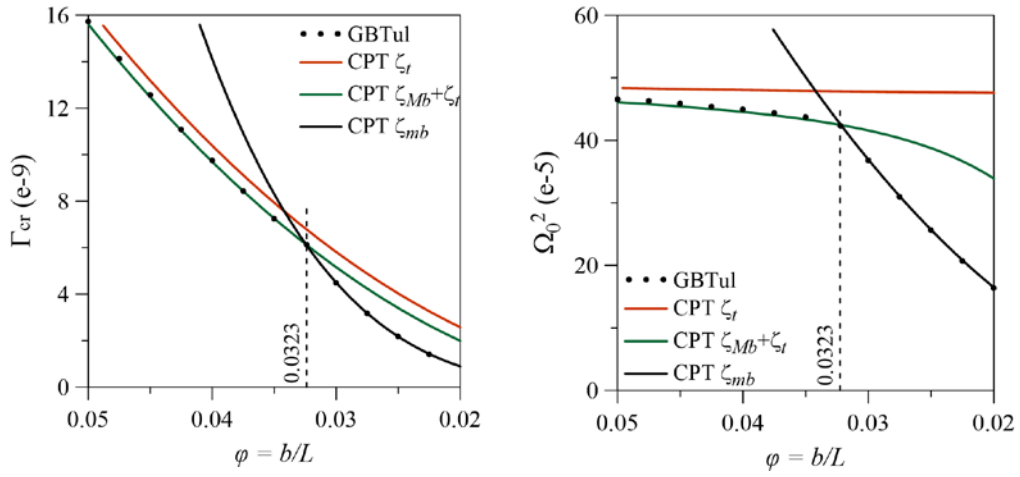

(a) Critical loads

(b) Fundamental frequencies

Figure 5.11 - Nondimensional parameters as a function of the aspect ratio φ ($\beta = 1.0$, $\xi = 1/15$).

Considering this modal transition and its dependence on ξ, Figure 5.12 and Figure 5.13 show, respectively, the variation of the critical load and fundamental frequency parameters with φ, for three selected values of ξ. Both sets of results show that as ξ increases, the transition value φ_t also increases (see dashed lines) and the minor axis flexural results can be applied to a wider range of φ (eqs. (5.23) and (5.24) can be applied to $\varphi \geq \varphi_t$). Considering the relation $\tau = \varphi\beta\xi = t/L$ and $\beta = 1.0$, the slenderness ratio τ decreases (here from 0.00337 to 0.00121) as ξ and φ_t decreases. Considering the transition points in Figure 5.13, the fundamental frequency parameter can be accurately approximated after the transition points by the function $\Omega_0 = 0.349\varphi^{1.95}$ for all value of ξ. The relation between φ_t and ξ is linear, being given by $\varphi_t = 0.489\xi - 0.0003$ (parabolic variation of τ_t).

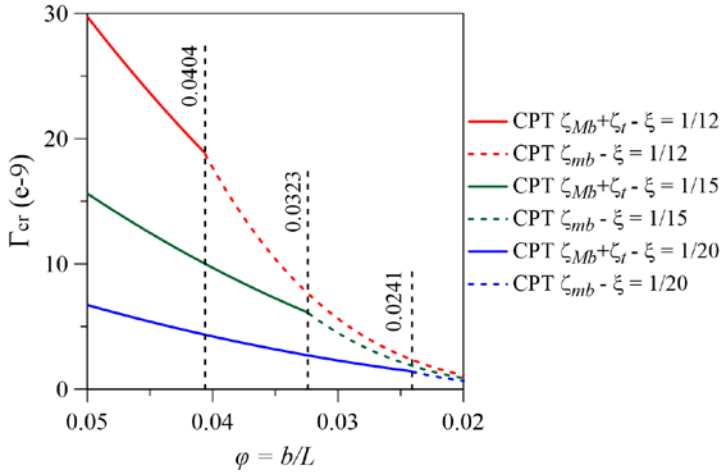

Figure 5.12 - Nondimensional critical load as a function of the aspect ratio φ. Influence of the parameter ξ on the critical aspect ratios φ_t where the sudden modal participation transitions occur. (β = 1.0).

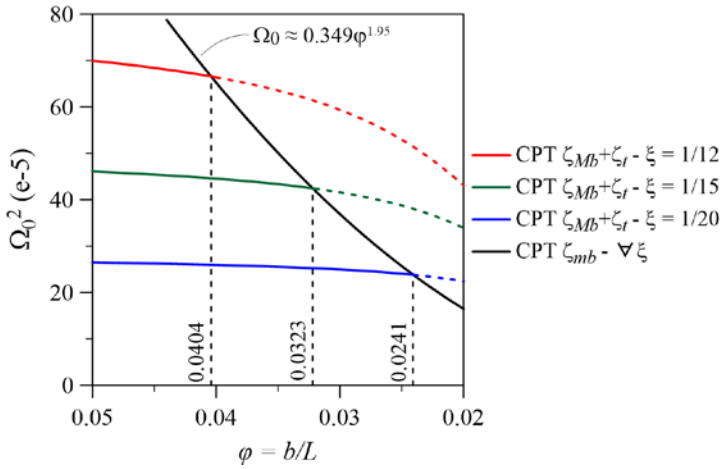

Figure 5.13 - Nondimensional fundamental frequency as a function of the aspect ratio φ. Influence of the parameter ξ on the critical aspect ratios φ_t where the sudden modal participation transitions occur. (β = 1.0).

In unequal-leg sections, the coupling of the minor axis bending mode with the torsional mode is expected. This can be observed in Figure 5.14, which presents the nondimensional critical load and fundamental frequency parameters as a function of the aspect ratio φ, considering β = 0.5 and ξ = 1/15 (values compatible with the L 150x75x5 section). Both sets of results show that the (ζ_{mb}+ζ_t) ROM agrees with the GBTul results in the range $0.02 < \varphi < 0.1$, similar to what was observed in the dimensional analysis. The major axis flexural-torsional and pure torsional ROMs lead to higher results, being the difference more pronounced for the fundamental frequency (Figure 5.14b). Also, as the aspect ratio φ decreases, increasing the profiles slenderness, the minor axis bending (ζ_{mb}) ROM naturally

tend to converge to the GBTul results. The results agree with Figure 4.3b and Figure 4.4.

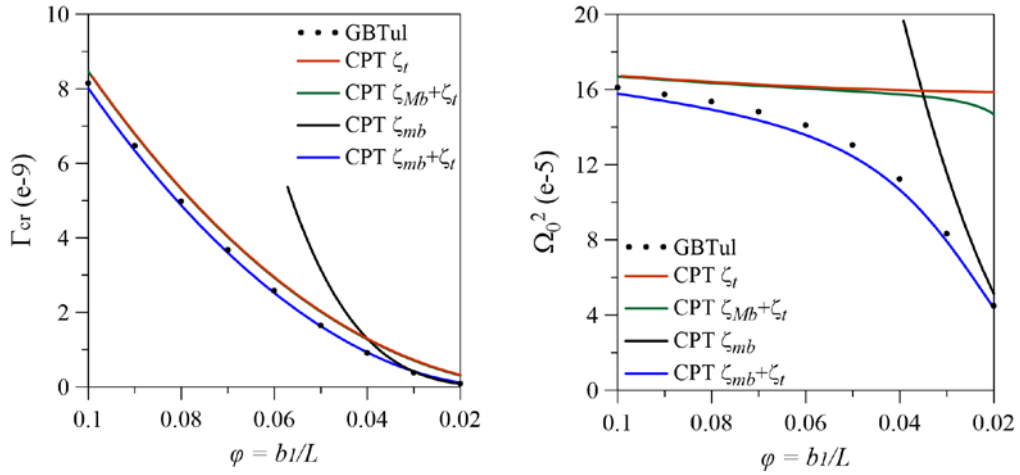

(a) Critical loads (b) Fundamental frequencies

Figure 5.14 - Nondimensional parameters as a function of the aspect ratio φ ($\beta = 0.5$, $\xi = 1/15$).

Figure 5.15 shows the variation of the nondimensional critical load (first column) and fundamental frequency (second column) parameters as a function of the aspect ratio β for $\varphi = 0.06$ and selected values of the slenderness parameter τ. Taking into account the relation between the geometric parameters, in each case $\xi = \tau/(0.06\beta)$. In all cases the ($\zeta_{mb}+\zeta_t$) ROM provides a lower bound while the ζ_t ROM provides an upper bound of the GBTul results, which moves slowly from the lower bound to the upper bound as β increases from 0.2 to 1. For an unequal-leg section with $\beta \leq 0.5$ the ($\zeta_{mb}+\zeta_t$) ROM gives excellent results, while for $\beta \geq 0.8$, the ζ_t ROM can be safely used. As τ decreases (the slenderness increases) the critical load and fundamental frequency parameters decrease and the difference between the two ROMs decrease for $\beta > 0.5$, being the difference very small for equal-leg sections. In the region where the results move from the ($\zeta_{mb}+\zeta_t$) coupled ROM to the ζ_t ROM, a small participation of the major axis bending mode is observed and the results can be obtained with precision using the ($\zeta_{Mb}+\zeta_{mb}+\zeta_t$) ROM (not shown explicitly here).

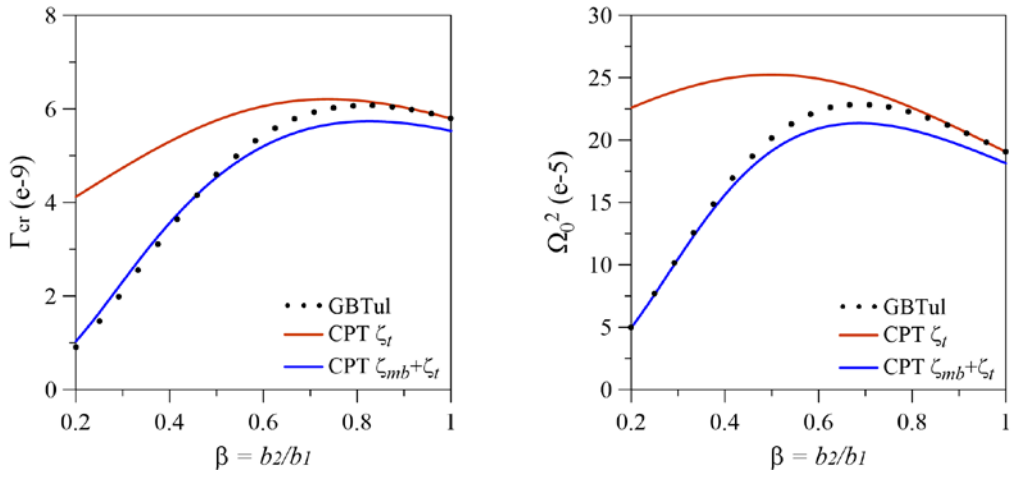

$\tau = t/L = 1/400$, $\xi = 1/(24\beta)$

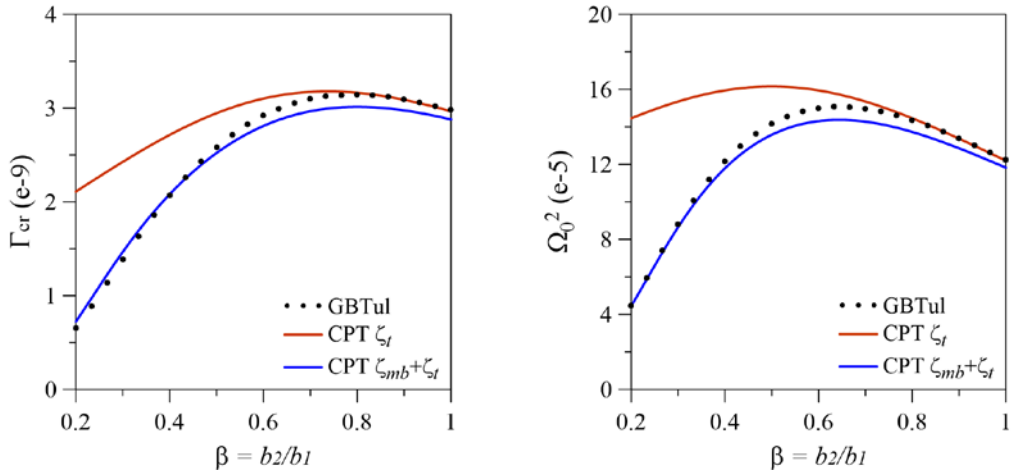

$\tau = t/L = 1/500$, $\xi = 1/(30\beta)$

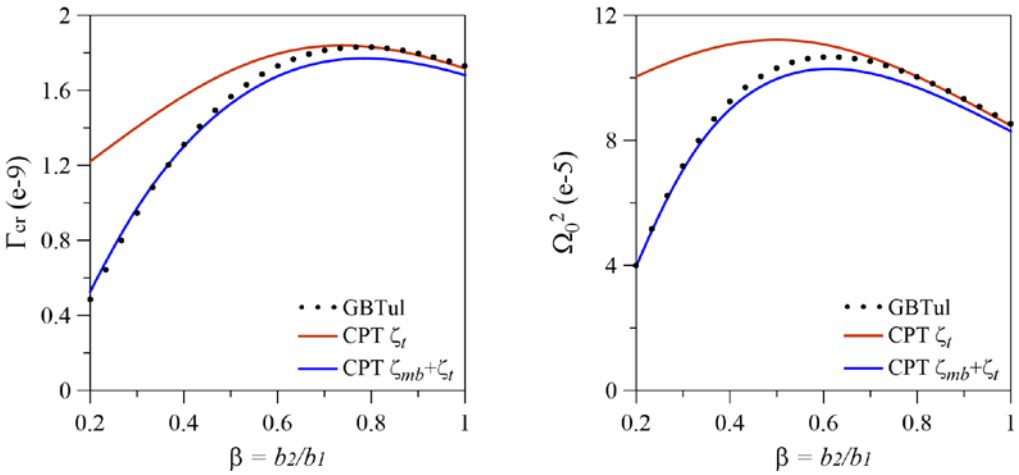

$\tau = t/L = 1/600$, $\xi = 1/(36\beta)$

Figure 5.15 - Nondimensional load and frequency parameters as a function of the aspect ratio β for $\varphi = 0.06$ and selected values of τ. First column: critical loads. Second column: fundamental frequencies.

Figure 5.16 shows the variation in the modal participation in the first buckling and vibration mode as a function of β for the case related to the second row in Figure 5.15 ($\varphi = 0.06$, $\tau = t/L = 1/500$, $\xi = 1/(30\beta)$), where it is possible to observe an interval of simultaneous influence of all the three deformation modes ($0.5 < \beta < 0.8$), which explains the need to consider more than two modes in order to obtain consistent results with the GBTul outcomes in this range of β.

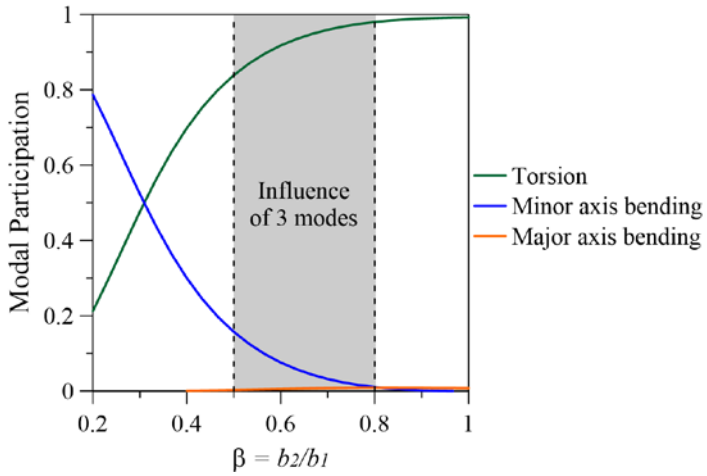

Figure 5.16 - Variation of the modal participation in the first buckling and vibration mode for angle section profiles as a function of β ($\varphi = 0.06$, $\tau = t/L = 1/500$, $\xi = 1/(30\beta)$).

To better understand the influence of β, Figure 5.17 shows the variation of the nondimensional critical load (first column) and fundamental frequency (second column) parameters as a function of the aspect ratio β for $\tau = t/L = 1/500$ and selected values of the parameter φ (0.06, 0.08). Now, $\xi = \tau/(\beta\varphi)$. It is observed that as β increases from 0.2 to 1, the lower bound and upper bound approach each other, being the difference very small for $\varphi = 0.08$, becoming the flexural contribution negligible in this case for $\beta > 0.5$.

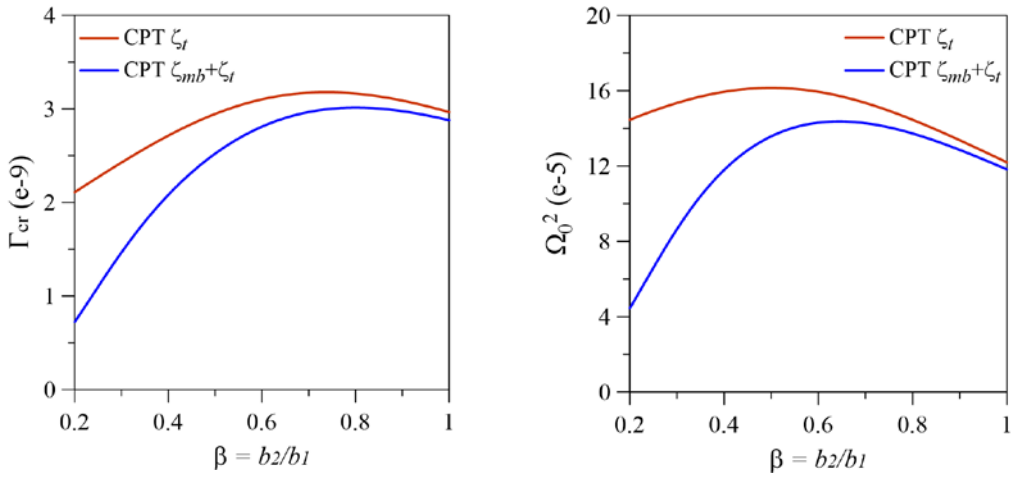

$\varphi = 0.06$, $\xi = 1/(30\beta)$

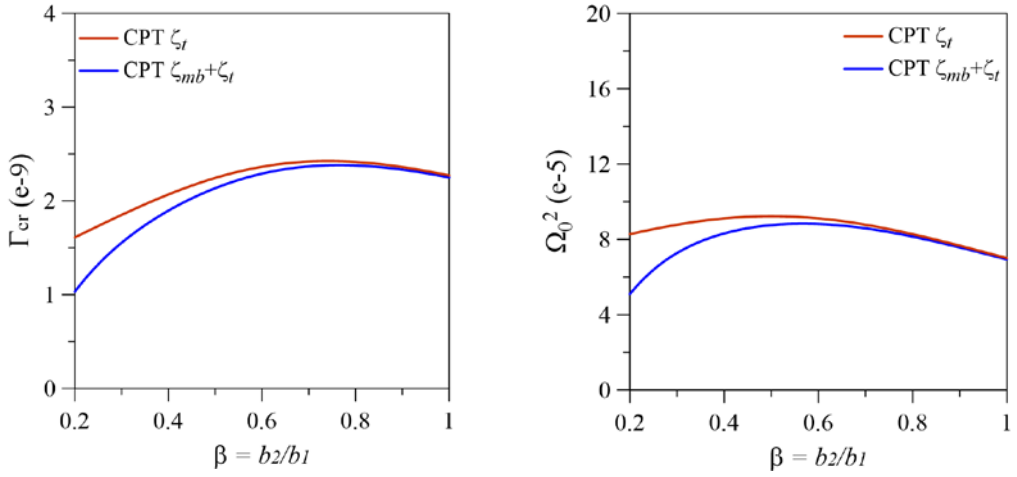

$\varphi = 0.08$, $\xi = 1/(40\beta)$

Figure 5.17 - Nondimensional load and frequency parameters as a function of the aspect ratio β for selected values of φ ($\tau = t/L$ = 1/500). First column: critical loads. Second column: fundamental frequencies.

Finally, the influence of the material properties is investigated. The critical load and fundamental frequency parameters are shown in Figure 5.18 as a function of the aspect ratio φ considering the same values of ψ shown in Table 4.1. As observed in Figure 4.7, in equal-leg profiles ($\beta = 1.0$), the transition point at which the abrupt change in modal participation occurs is also influenced by the material parameter ψ. In order to investigate this effect on the linear results, Figure 5.18 presents the nondimensional critical load and natural frequency parameters for a section equivalent to the L 75x75x5 profile ($\beta = 1.0$; $\xi = 1/15$) as a function of φ for the same values of ψ considered in the modal participation analysis (see Table 4.1). As it can be observed, there is no variation in the results with the material

parameter when the pure bending ROM (ζ_{mb}) is considered, which agrees with eqs. (5.23) and (5.24). Before the transition point, the results are governed by the flexural-torsional($\zeta_{Mb}+\zeta_t$) ROM, in agreement with Figure 4.7, where the modal participation before the abrupt change was observed due to torsional and major-axis bending coupling. Additionally, as φ decreases, the curves for the critical load parameter approach each other, converging to the pure bending ROM. All transition parameters φ_t are in agreement with the respective transition profile lengths shown in Figure 4.7 ($\varphi_t = b/L_t$). One should have in mind that the respective dimensional results should be obtained by inverting eqs. (5.19) and (5.20), being the critical load directly proportional to E_1 and the fundamental frequency proportional to $\sqrt{E_1}$, and both inversely proportional to (1-$\nu_{12}\nu_{21}$) (plate effect).

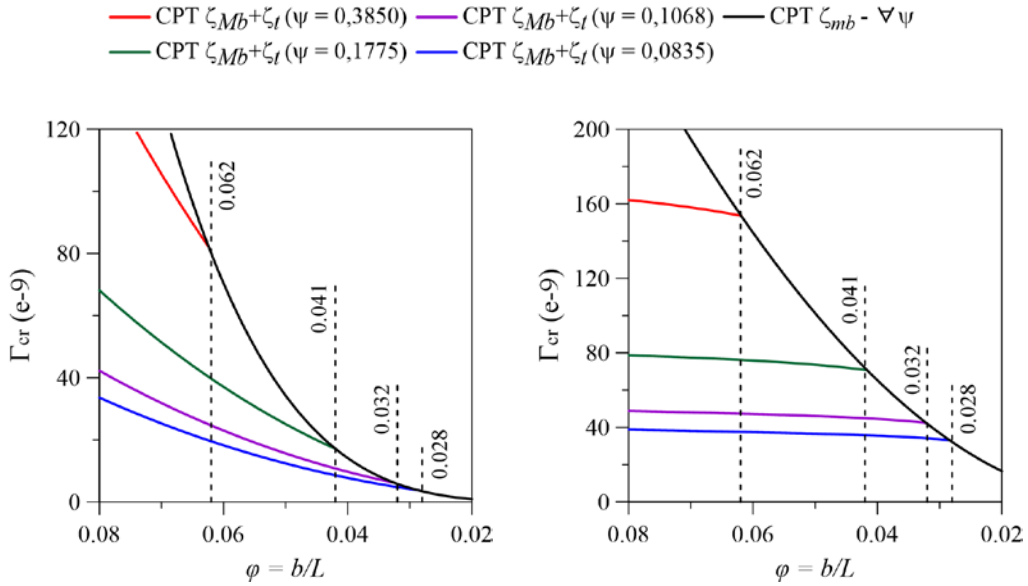

(a) Critical loads (b) Fundamental frequencies

Figure 5.18 - Nondimensional parameters as a function of the aspect ratio φ. Influence of the parameter ψ on the critical aspect ratios φ_t where the sudden modal participation transitions occur. (β = 1.0; ξ = 1/15).

Figure 5.19 shows the nondimensional critical load and fundamental frequency parameters as a function of the material parameter ψ. The curve in green refers to an equal-leg angle section equivalent to the L 150x150x5 section (β = 1.0), while the blue curve refers to an unequal-leg angle section equivalent to the L 150x50x5 section (β = 0.33), both with φ = 0.06 (compatible with the intermediate length L = 2.5 m). For the equal-leg section, torsion is dominant for all values of ψ and the load and frequency parameters increase linearly with the

material parameter ψ. This is expected because the load and frequency are directly proportional to the material parameter when considering pure torsion, as shown previously in eqs. (5.21) and (5.22). On the other hand, for the unequal-leg profile, although torsion is initially dominant, the influence of the minor axis bending mode increases with ψ, and both the load and frequency parameters increase more slowly approaching an upper bound. In the latter case, the participation of the minor axis bending mode increases from 21.64%, for $\psi = 0.05$, to 86.06%, for $\psi = 0.50$, considering $\varphi = 0.06$. In both cases, a linear relation is observed between the applied load Γ and Ω_0^2, the expected load-frequency relation in columns, with $\Omega_0^2 = 0$ at $\Gamma = \Gamma_{cr}$.

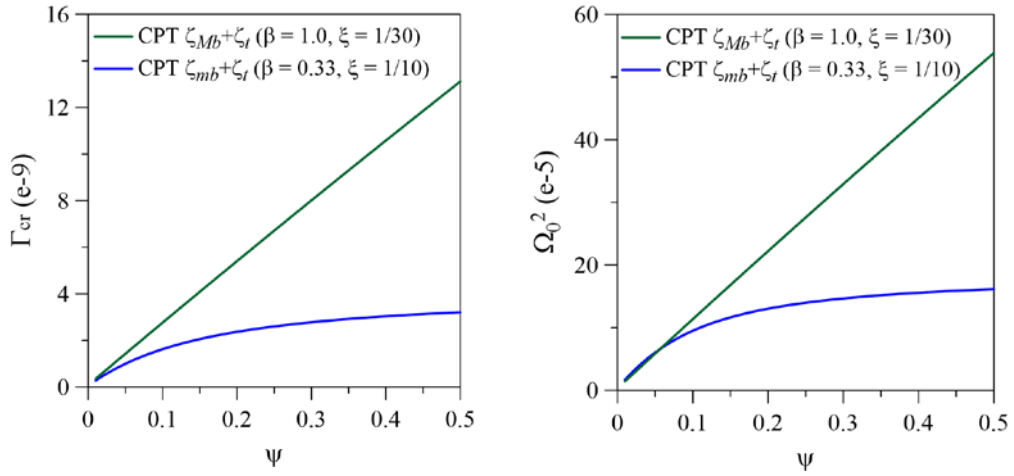

(a) Critical loads

(b) Fundamental frequencies

Figure 5.19 - Nondimensional parameters as a function of the material parameter ψ ($\varphi = 0.06$).

6
Post-buckling Behaviour of FRP Angle Section Profiles

Based on the previous parametric analyses for identification of modal participation, calculation of critical load and comparison with the GBTuL software, this chapter presents an investigation on the post-buckling behavior of axially loaded pultruded angle section profiles. By solving the system of nonlinear equilibrium equations for each reduced-order model (ROM), post-buckling paths are determined, and a detailed parametric analysis of the influence of the dimensionless parameters on post-buckling strength is conducted. Finally, the sensitivity of the solutions to initial geometric imperfections is investigated.

6.1
Nonlinear equilibrium equations

The energy functionals for thin-walled profiles, based on the von Kármán nonlinear plate theory and considering initial geometric imperfections, were derived in Chapter 3. The ROM's deduced in Chapter 4 are used to discretize the functionals by means of the Ritz method. The resulting algebraic nonlinear equations are solved using the Newton-Raphson method and continuation techniques in order to obtain the post-buckling equilibrium paths. The variables are the nondimensional amplitudes C_1 and C_3, related to axial shortening, C_2 and C_4, related to bending, and C_5, C_6 and C_7 related to torsion.

In addition to the nondimensional parameters previously defined, an additional parameter is introduced in the nonlinear analysis; the usual nondimensional axial load parameter defined as:

$$\lambda = \frac{\Gamma}{\Gamma_{cr}} = \frac{P}{P_{cr}} \tag{6.1}$$

where:

$$P = N_x\left(b_1 + b_2\right) \text{ and } \Gamma = \frac{P\left(1-\nu_{12}\nu_{21}\right)}{\pi^2 E_1 L^2} \tag{6.2}$$

The coefficients A_{12}, A_{22} e D_{12} arising from the constitutive relation (eq. (3.7)) appear in the nonlinear terms of the equilibrium equations. Thus, the modulus of elasticity E_2, not present in the linear eigenvalue problems, appears explicitly in the nonlinear equilibrium equations. Hence, the ratio of the transversal and longitudinal Young's moduli of the orthotropic material is introduced as a new variable:

$$\eta = \frac{E_2}{E_1} \tag{6.3}$$

Initially, the post-buckling behavior of the perfect structure is studied. First, the influence of the nondimensional geometric parameters reported in Chapter 5 is investigated while keeping constant the material's physical properties (ψ = 0.1068, η = 0.3, see Table 2.4). Then, the influence of the pultruded material is investigated for a fixed geometry. Finally, the sensitivity of the nonlinear solutions to initial geometric imperfections is examined, an important step in stability analysis.

6.2
Post-buckling behaviour

The cases analyzed here follow the same sequence as those for the critical load in Chapter 5. Figure 6.1a illustrates the three-dimensional post-buckling path of an equal-leg angle profile (β = 1.0) with $\varphi = b/L$ = 0.04 and $\xi = t/b$ = 1/30 together with the projections into two planes, Figure 6.1b and Figure 6.1c. As shown in Figure 5.10, the buckling is governed in this case by the flexural-torsional model considering major axis bending, the (ζ_{Mb}+ζ_t) ROM. Thus, the post-buckling path is a function of the modal amplitudes C_4 and C_5. For both amplitudes, the structure exhibits a stable symmetric pitchfork bifurcation. For the considered profile, it is observed that the amplitudes are small even for high values of λ (λ>>1), indicating a fairly high post-buckling strength reserve, similar to that exhibited by individual plates, in agreement with known experimental results (Cardoso & Togashi, 2018). The transversal displacement due to bending at mid-length of the profile is given by $W_{max} = C_4 t \sin\alpha$ (eq. (4.18)), where t is the plates' thickness, and α is the angle that define the principal axes of inertia (Figure 4.11),

here $\alpha = 45^{o}$. The amplitude C_5, in turn, represents the rotation of the legs due to torsion.

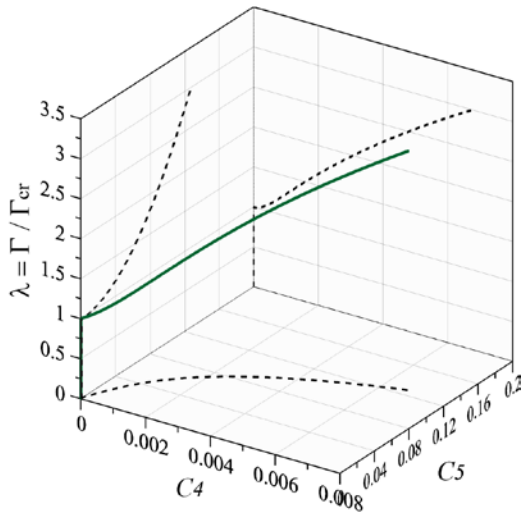

(a) 3D view (solid line in green) and projections (dashed lines)

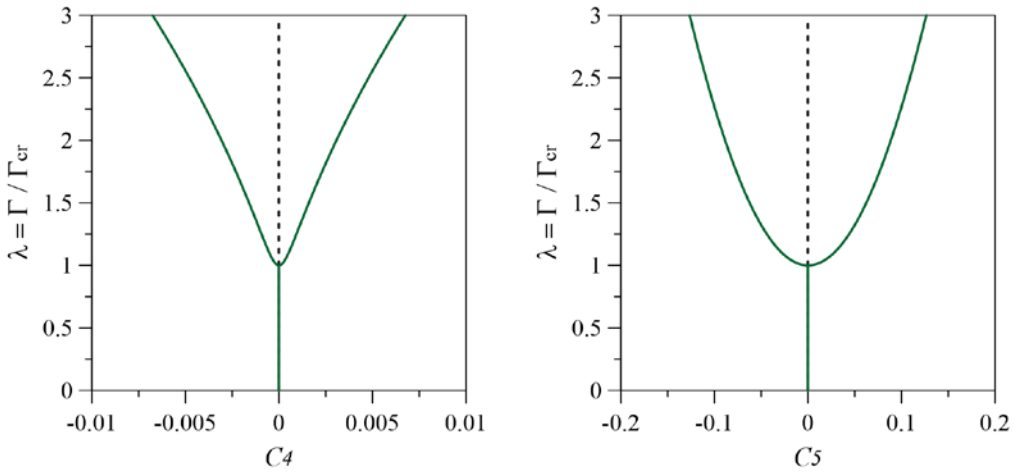

(b) λ x C_4 (c) λ x C_5

Figure 6.1 - post-buckling paths of an equal-leg angle section profile ($\beta = 1.0$, $\varphi = 0.04$, $\xi = 1/30$).

6.2.1

Effect of the wider plate width-to-length aspect ratio, φ, in equal-leg profiles

As shown in preceding chapters through the modal participation analysis (see Figure 4.3), for equal-leg angle sections, as the aspect ratio ($\varphi = b/L$) decreases (shorter leg width or longer profiles), the influence of the torsional mode, initially dominant, decreases as the contribution of major axis bending increases up to a

certain critical value where an abrupt change in modal participation is observed (Figure 4.6). Consequently, the post-buckling flexural stiffness decreases as φ decreases, given their increasing susceptibility to bending. The effect of this trend is shown in Figure 6.2a and b, which depicts the post-buckling paths for equal-leg profiles, considering the ($\zeta_{Mb}+\zeta_t$) ROM and two distinct values of the plate aspect ratio φ, namely $\varphi = 0.04$ and $\varphi = 0.02$. In both cases, a stable symmetric pitchfork bifurcation is observed. However, the modal contribution is different in each case. Figure 6.2c shows the projections of the post critical paths presented in Figure 6.2a and b onto the plane C_5 x C_4. First, the column rotates almost without bending, being this effect more pronounced for higher values of φ. As C_5 increases, the bending displacement C_4 increases more rapidly, tending C_5 to an upper bound, being advanced post-buckling configurations dominated by bending. Indeed, as seen in previous chapters, for very slender profiles, the contribution of torsional mode approaches zero (Figure 4.6), and the profile becomes susceptible to pure minor-axis bending instability.

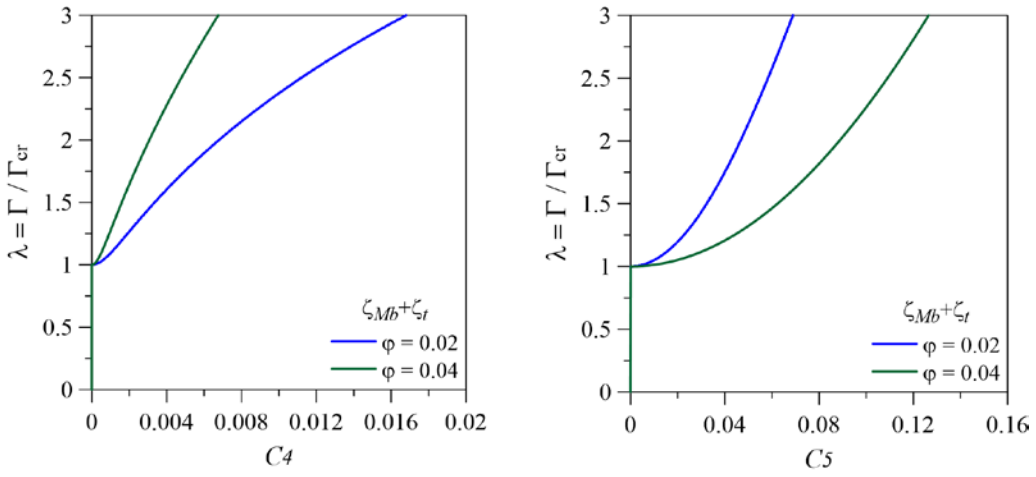

(a) λ x C_4 (b) λ x C_5

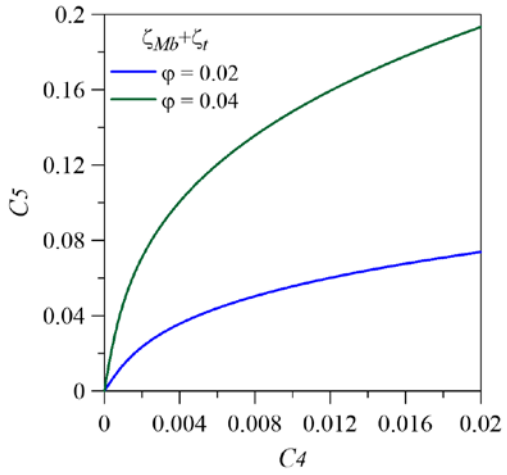

(c) C_5 x C_4

Figure 6.2 - Post-buckling paths for equal-leg angle section profiles with varying plate aspect ratio φ (β = 1.0, ξ = 1/30).

Although the major-axis flexural-torsional mode is predominant for short-to-intermediate length angle profiles, the bending contribution is very low. As shown in Figure 5.10, the pure torsional ζ_t ROM and the coupled (ζ_{Mb}+ζ_t) ROM result in practically the same critical load, being both in agreement with the GBTuL results. Figure 6.3 compares the post-buckling paths obtained with both ROMs. The same post-buckling behavior is observed with the curves becoming increasingly closer as φ increases, reiterating the increasing importance of the torsional contribution with φ. For $\varphi < 0.02$, although still very close, the curves diverge as λ increases, being the post-buckling strength obtained with the ζ_t ROM higher than that of the flexural-

torsional mode. These results show that the post-buckling stiffness is mainly due to torsion.

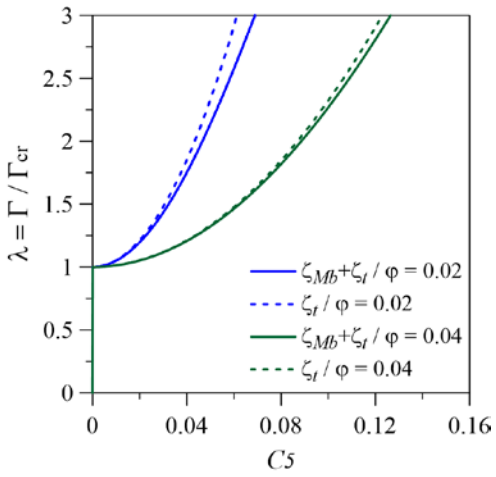

Figure 6.3 - Comparison of post-buckling paths for equal-leg angle section profiles considering pure torsional (ζ_t) and flexural-torsional ($\zeta_{Mb}+\zeta_t$) ROMs (β = 1.0, ξ = 1/30).

6.2.2

Effect of the wider plate width-to-length aspect ratio, φ, in unequal-leg profiles

For the unequal-leg profiles, it was observed that, for low values of φ, the critical load is associated with the minor axis bending mode with a transition to the torsional-flexural mode with minor axis bending as φ increases. Figure 6.4 shows the post-buckling response of unequal-leg profiles with β = 0.5 and ξ = 1/15, considering φ = 0.04 and φ = 0.02. Both the ($\zeta_{mb}+\zeta_t$) ROM and the ζ_{mb} ROM are considered. A stable symmetric pitchfork bifurcation is obtained in both cases. For φ = 0.04, the critical load is given by the torsional-flexural mode with minor axis bending (see Figure 5.14a). The participation of torsion in the critical mode results in a relatively high post-buckling strength (Figure 6.4a), increasing the profile load-carrying capacity, but it is comparatively much lower than that of the equal-leg profile when governed by major-axis flexure-torsion. However, the effective stiffness (tangent to the path) decreases approaching a maximum value (limit point) for large deflections, a behavior detected in some previous analyses (Dinis et al., 2012; Monteiro & Malite, 2021). As φ decreases, the contribution of torsion decreases (Figure 4.3b), and, consequently, the post-buckling stiffness approaches that of a Euler column with an almost horizontal post-buckling path, characterized

by significant bending displacements for a very small increase in the load level. For $\varphi = 0.02$ both ROMs leads to practically the same critical load (see Figure 5.14a) and the equilibrium paths depicted in Figure 6.4b exhibit practically the same behavior. This shows that the torsional contribution to the post-buckling stiffness is also a key factor for unequal-leg angle profiles.

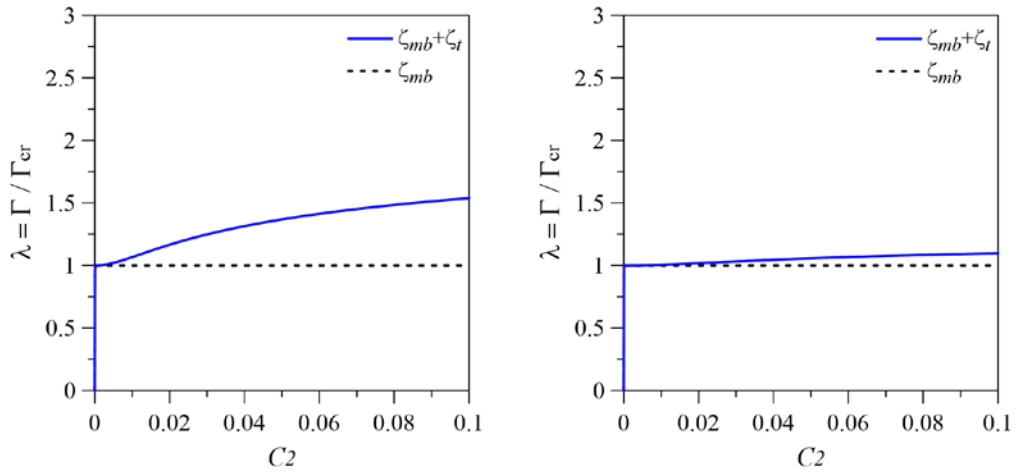

(a) $\varphi = 0.04$ (b) $\varphi = 0.02$

Figure 6.4 - Post-buckling paths of unequal-leg angle section profiles with $\beta = 0.5$ and $\xi = 1/15$, considering pure bending (ζ_{mb}) and flexural-torsional ($\zeta_{mb}+\zeta_t$) ROMs.

Figure 6.5 depicts the effect of the variation of φ on the torsional amplitude (C_5) of the coupled solution. In Figure 6.5a, both curves were plotted until they reached the same bending amplitude near the limit point ($C_2 = 0.05$). It is observed that, for the highest value of φ ($\varphi = 0.04$), the torsional component reaches a much higher amplitude ($C_5 = 0.147$), given that for higher values of φ, the torsional mode has a larger contribution. The same can be observed in Figure 6.5b, which illustrates the projection of the post-critical paths onto the plane C_5 x C_2. It is observed that for the same flexural amplitude, the torsional amplitude is much higher when $\varphi = 0.04$.

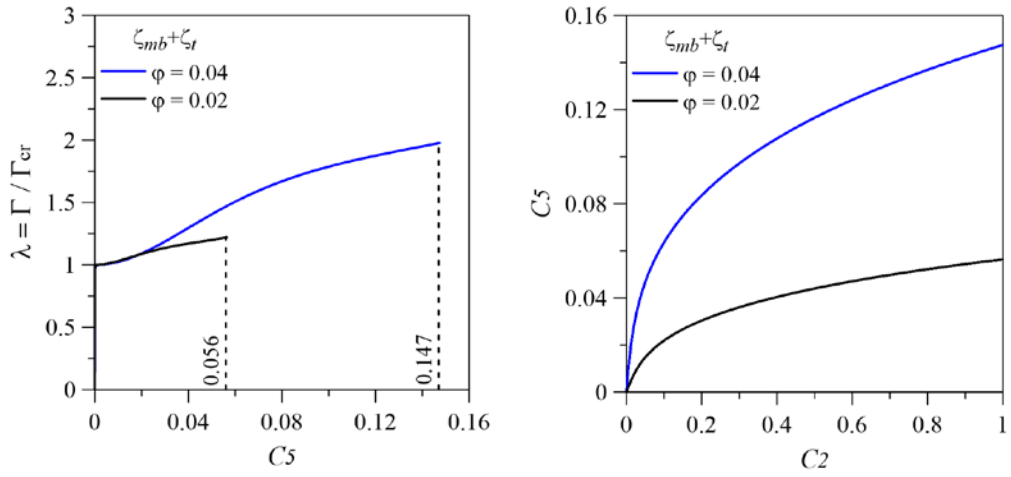

(a) λ x C_5 (b) C_5 x C_2

Figure 6.5 - Post-buckling paths for the unequal-leg angle section profiles. Influence of φ on the torsional amplitudes (β = 0.5, ξ = 1/15 and varying φ).

6.2.3

Effect of the aspect ratio β on the post-buckling response

Flexural-torsional instability in angle section profiles encompasses both minor and major axis bending. Minor axis bending is evident in the flexural-torsional response of unequal-leg profiles as well as in the flexural response of slender equal-leg profiles. On the other hand, major axis bending is observed in short and intermediate-length equal-leg profiles. This underscores the significance of investigating the influence of the ratio of the leg widths, $\beta = b_2/b_1$, on the post-buckling response (see Figure 5.6).

Figure 6.6 compares the post-buckling paths for an equal-leg profile (β = 1.0) and two unequal-leg profiles (β = 0.5 and β = 0.8), both considering the same wider plate aspect ratio (φ = 0.04). In order to investigate the influence of β, the slenderness of the shorter plate ($\xi = t/b_2$) must vary for each profile, so that the thickness of the plates remains the same. Here, the equal-leg section is equivalent to the L 150x150x5 profile (ξ = 1/30), and the unequal-leg sections to the profiles L 150x75x5 (ξ = 1/15) and L 150x120x5 (ξ = 1/24). As bending occurs along different principal axes for each considered aspect ratio, each post-buckling path in Figure 6.6 is obtained by considering the appropriate ROM (see Figure 5.5). The *x*-axis in Figure 6.6a and c are given in terms of the flexural amplitudes C_2 or C_4, since both coupled ROMs are considered. As observed, the equal-leg profile

exhibits significantly higher post-buckling stiffness than the unequal-leg profiles, with λ increasing quickly with the modal amplitudes. The unequal-leg profile with $\beta = 0.5$ exhibits lower post-buckling flexural stiffness due to the contribution of minor axis bending, being the effective stiffness almost constant, leading to very large bending displacements for a small increase in the load level. The influence of the torsional component is illustrated in Figure 6.6b. For the unequal-leg profile with $\beta = 0.8$, the post-critical flexural stiffness shows an intermediate value but always increase with λ, being close to that of the equal-leg angle profile ($\beta = 1.0$), indicating a similar post-buckling load-carrying capacity. Finally, Figure 6.6c shows the projections onto the amplitudes plane. It is observed that, indeed, for the same flexural amplitude, the torsional amplitudes increase with β, reaching its maximum value for the equal-leg angle profile.

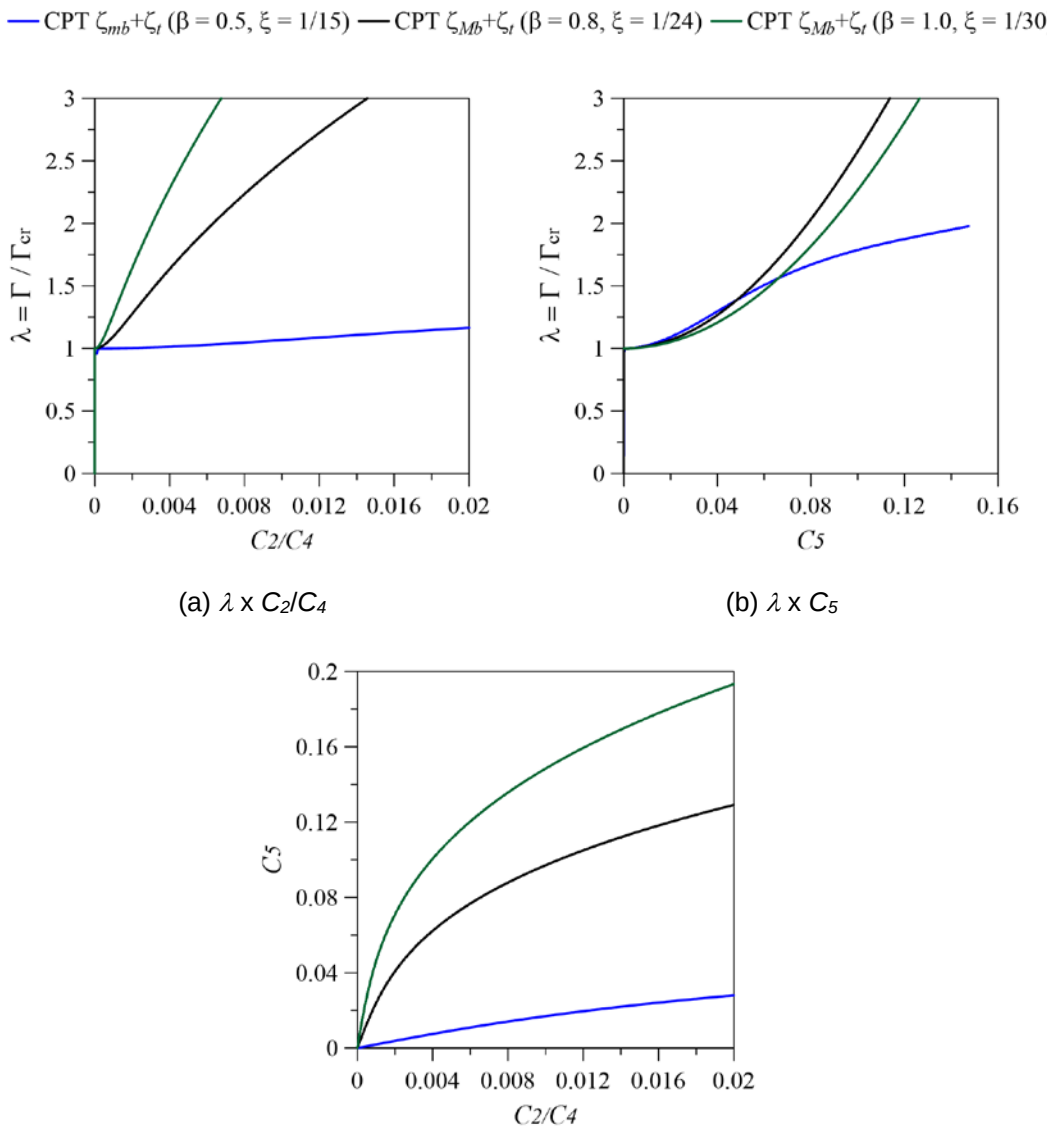

(a) λ x C_2/C_4

(b) λ x C_5

(c) C_5 x C_2/C_4

Figure 6.6 - Post-buckling paths for angle section profiles with varying aspect ratio for the angle legs β (φ = 0.04).

6.2.4
Effect of modal interaction

Figure 5.9a shows that for equal-leg angle sections and small values of *b*, the critical load is obtained using the ζ_{mb} ROM, and it increases exponentially up to a maximum value. At this point, there is an abrupt change in modal participation, and the critical load is now given by the ($\zeta_{Mb}+\zeta_t$) ROM, where the critical load decreases with the leg width *b*. Considering $\beta = 1.0$ and maintaining constant the profile length and thickness, the geometric parameters φ and ξ change accordingly with *b*.

Figure 6.7 shows the post-buckling paths for selected values of b in Figure 5.9a. For $\varphi = 0.02$ and $\xi = 0.0625$ (b = 80 mm), the critical load is associated with minor axis bending. For $\varphi = 0.0248$ and $\xi = 0.0505$ (b = 99 mm), the load reaches a maximum value and the ζ_{mb} and (ζ_{Mb}+ζ_t) ROMs lead to the same critical load. Finally, for $\varphi = 0.03$ and $\xi = 0.0417$ (b = 120 mm), the buckling is governed by the flexural-torsional mode considering major axis bending. The results agree with those in Figure 6.4, where for the ζ_{mb} ROM, the post buckling path is practically horizontal, leading to large flexural displacements. For the (ζ_{Mb}+ζ_t) ROM, the post-buckling path exhibits a much higher stiffness.

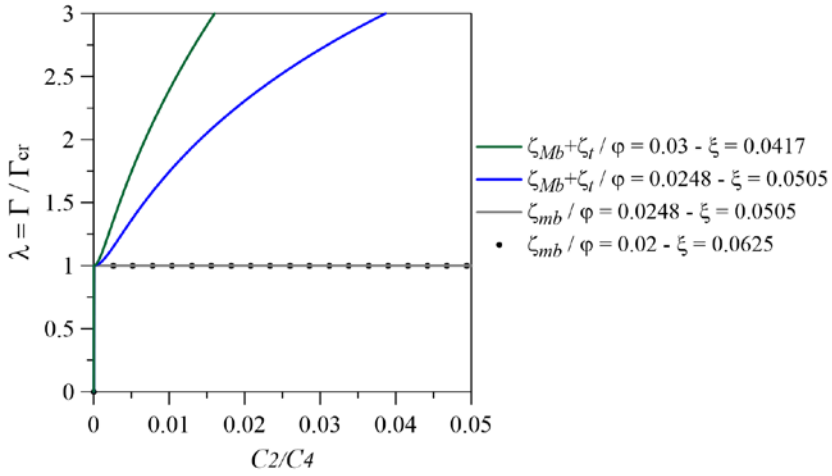

(a) λ x C_2/C_4

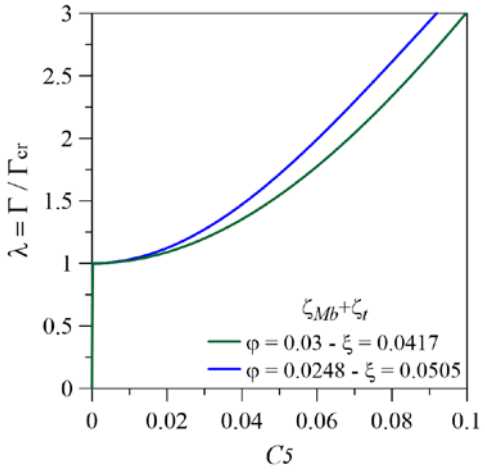

(b) λ x C_5

Figure 6.7 - Post-critical paths for equal-leg angle section profiles with varying φ and ξ (β = 1.0).

As observed in Figure 4.6, equal-leg profiles may also undergo a sudden transition in modal participation as the wider plate aspect ratio φ decreases. At this point, distinct buckling modes exhibit the same critical load value, which may lead to interaction between different deformation modes (modal interaction) due to nonlinear modal coupling terms. For the parameters considered in Figure 5.11, where the transition point occurs at $\varphi_t = 0.032$, the influence of modal interaction on the post-buckling behaviour is investigated. Figure 6.8 shows the post-buckling paths for $\varphi = 0.04$, $\varphi = \varphi_t = 0.032$ and $\varphi = 0.02$. The ($\zeta_{Mb}+\zeta_t$) and ζ_{mb} ROM are used for $\varphi = 0.04$ and $\varphi = 0.02$, respectively, based on the observed modal participation in Figure 5.11. For $\varphi = \varphi_t$, both models are used. As observed in Figure 6.8a, the post-buckling strength decreases as the plate aspect ratio decreases, agreeing with the result observed in Figure 6.2. The column with $\varphi = 0.04$ exhibit high post-buckling strength, which is practically reduced to zero for $\varphi = 0.02$, when only minor axis bending occurs, similar to the classical Euler results (Levien, 2008), leading to large lateral bending deflections. It is important to note the difference in the post-buckling behavior for each ROM at the transition point ($\varphi_t = 0.032$). As in the previous example, the ($\zeta_{Mb}+\zeta_t$) ROM exhibits at $\varphi = \varphi_t$ a high post-buckling stiffness while the ζ_{mb} ROM results in almost neutral post-buckling behavior. The coupled ($\zeta_{Mb}+\zeta_t+\zeta_{mb}$) ROM, which considers all possible interactions, leads to an intermediate post-buckling strength, but also exhibits large bending deflections. Figure 6.8b shows the influence of the torsional mode on the column response, while Figure 6.8c shows the relation between the controlling amplitudes C_5 and C_4. These results confirm the decrease in post-buckling strength with φ and the increasing importance of the flexural displacement in the post-buckling range. Comparing the two curves for $\varphi_t = 0.0323$ in Figure 6.8b, considering two different ROMs, it is observed that the coupled ($\zeta_{Mb}+\zeta_t+\zeta_{mb}$) ROM leads to a different type of behavior with the response becoming progressively more flexible with the column tending to a limit point.

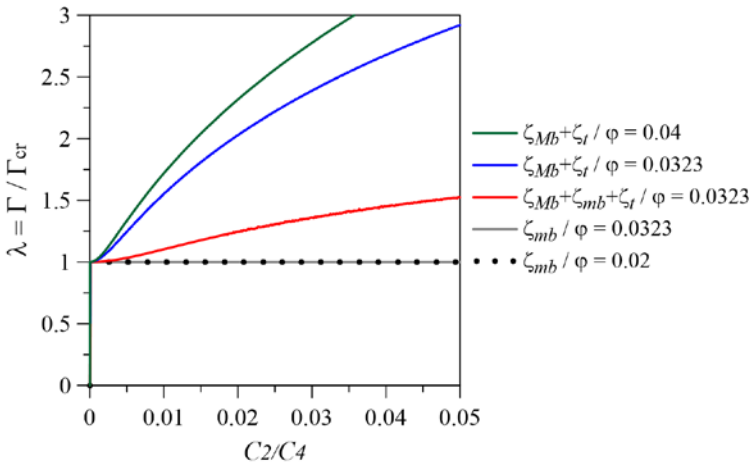

(a) λ x C_2/C_4

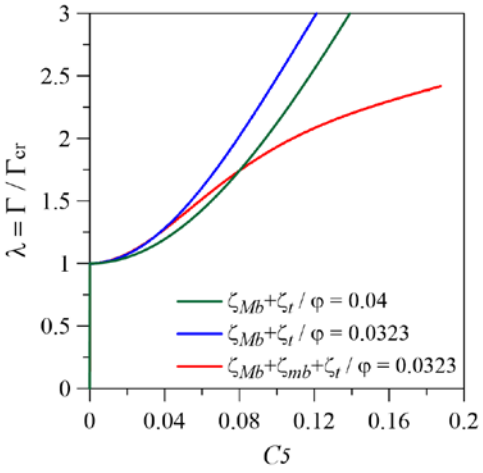

(b) λ x C_5

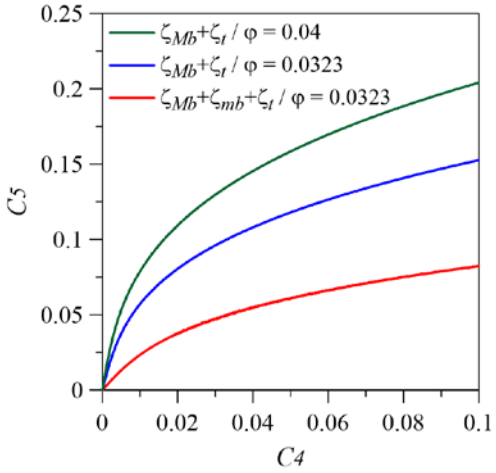

(c) C_5 x C_4

Figure 6.8 - Influence of modal interaction on the post-buckling paths for equal-leg angle section profiles with varying wider plate aspect ratio φ (β = 1.0, ξ = 1/15).

6.2.5

Effect of the material parameter

In Figure 6.9, the influence of the nondimensional material parameter on the post-buckling paths of equal-leg angle section profiles (β = 1.0) is studied, while keeping the geometric parameters constant (ξ = 1/15, φ = 0.05). The same material parameters adopted in Figure 5.18 are here considered. It should be emphasized that the smallest material parameter (ψ = 0.0835) corresponds to the material with the highest longitudinal stiffness (eq. (4.6)), and the largest one (ψ = 0.3850) represents an isotropic material, considering $\nu_{12} = \nu_{21} = 0.23$ ($\psi = (1-\nu)/2$). All paths were obtained using the ($\zeta_{Mb}+\zeta_t$) ROM, except for the isotropic material, whose modal

participation is entirely governed by the pure minor-axis bending mode when $\varphi = 0.05$ (according to Figure 4.7 and Figure 5.18), requiring the use of the ζ_{mb} ROM. The red dashed curve represents what the post-buckling path for the isotropic material would be if the predominant mode continued to be flexural-torsional mode with major-axis bending. As shown in Figure 5.18a, the critical load in each case is necessarily different. For comparison purposes, Table 6.1 shows the critical load for the selected values of the material parameter ψ.

As expected, the profile with the stiffer material in the longitudinal direction ($\psi = 0.0835$) shows the highest post-buckling strength reserve in both bending and torsion. It is observed that a high load ratio is needed to achieve even small flexural displacements, which does not occur for the isotropic material ($\psi = 0.3850$), where the post-buckling flexural stiffness gain is expressively lower (Figure 6.9a). As a reference, for a steel profile ($E = 210$GPa, $\nu = 0.3$), $\psi = 0.35$. For torsional amplitudes, even though the stiffness gain decreases as the material parameter increases, the isotropic material suddenly does not experience these amplitudes (Figure 6.9b), due to its fundamental mode being governed by pure minor axis bending. This shows that, for the same geometric parameters, pultruded profiles exhibit higher post-buckling stiffness than isotropic profiles. Additionally, it is emphasized that isotropic profiles of intermediate to long lengths are prone to larger flexural amplitudes while pultruded profiles of short to intermediate length are liable to reduced amplitudes. The influence of the material on unequal-leg profiles is illustrated in Figure 6.10, considering $\beta = 0.5$, $\xi = 1/15$ and $\varphi = 0.05$. In all cases flexural-torsional buckling with minor axis bending is observed, which implies large bending amplitudes for small load values, even for the axially stiffer pultruded material ($\psi = 0.0835$), compared to equal-leg profiles. Furthermore, the influence of torsion on the post-buckling paths of the isotropic material leads to a positive strength reserve, unlike the flat path observed for the pure bending ROM.

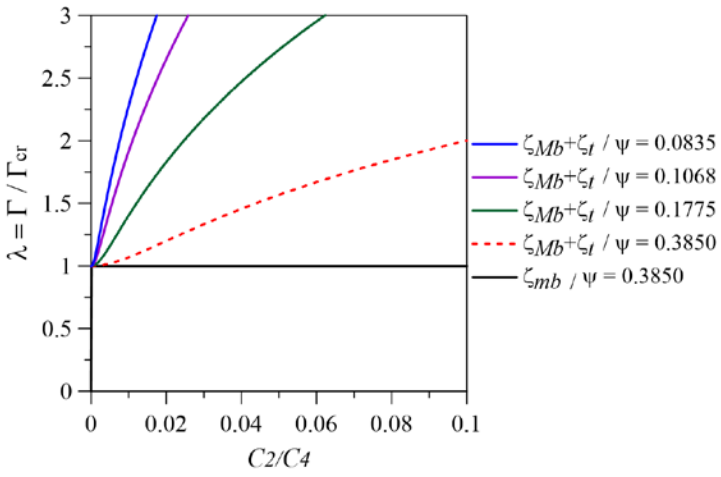

(a) λ x C_2/C_4

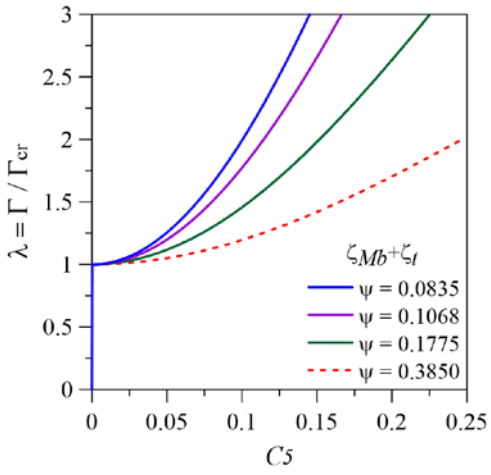

(b) λ x C_5

Figure 6.9 - Post-buckling paths for equal-leg angle section profiles with varying material parameters ψ (β = 1.0, ξ = 1/15, φ = 0.05).

Table 6.1 - Critical load parameters for selected values of ψ (β = 1.0, ξ = 1/15, φ = 0.05).

ψ	ROM	Γ_{cr} (x10-9)
0.0835	$\zeta_{Mb}+\zeta_t$	12.39
0.1068	$\zeta_{Mb}+\zeta_t$	15.62
0.1775	$\zeta_{Mb}+\zeta_t$	25.05
0.3850	$\zeta_{Mb}+\zeta_t$	49.83
0.3850	ζ_{mb}	34.69

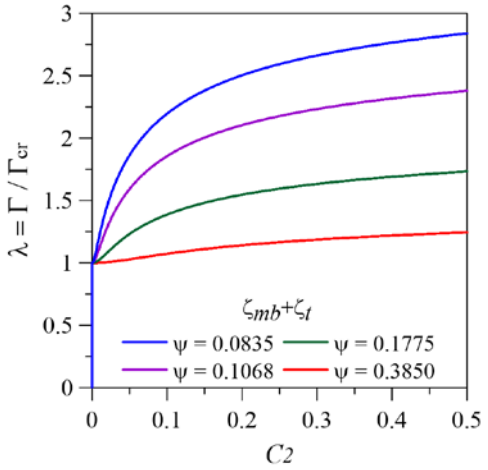

(a) λ x C_2/C_4

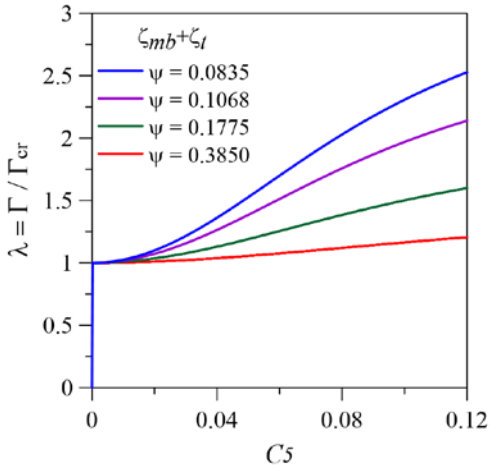

(b) λ x C_5

Figure 6.10 - Post-buckling paths for unequal-leg angle section profiles with varying material parameters ψ (β = 0.5, ξ = 1/15, φ = 0.05).

6.3
Sensitivity to imperfections

The structural behaviour and resistances of thin-walled steel members are generally affected by initial geometric imperfections. For angle section columns, there are three important types of initial geometric imperfections (Behzadi-Sofiani et al., 2021): global imperfections about the major and minor principal axes, and torsional imperfections about the shear center. Zhang et al. (2021) obtained experimentally the initial geometric imperfections of pin-ended stainless steel angle section columns failing by flexural-torsional buckling. The tests and numerical data obtained in their work were used to assess the accuracy of relevant codified design

methods. For FRP angle sections, geometric imperfections are inherently connected to the fabrication process described in Chapter 2. Figure 6.11 illustrates the three-dimensional post-buckling path of an angle profile subjected to initial geometric imperfections, as a function of the modal amplitudes C_4 and C_5, generated by using the ($\zeta_{Mb}+\zeta_t$) ROM. The typical post-buckling behavior of structures with initial imperfections is observed, represented by a curve asymptotic to the equilibrium path of the perfect structure. The imperfection destroys the symmetric bifurcation of the ideal perfect system, leading to a preferential path starting at the unloaded position and function of the imperfection shape and sign (Thompson & Hunt, 1973).

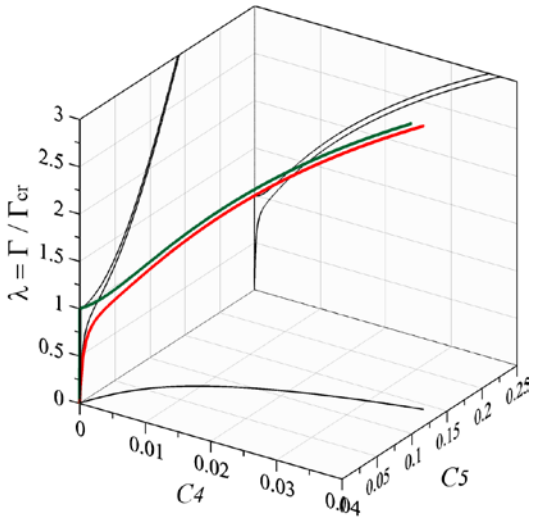

Figure 6.11 - Post-buckling path of an angle profile subjected to initial geometric imperfections (β = 1.0, φ = 0.04, ξ = 1/30). Green curve: perfect structure, red curve: imperfect structure.

The effect of initial geometric imperfections is incorporated into the system through a function $w_0(x)$, as shown in the strain-displacement relations of the plate mid-surface, eq. (3.5). It is generally agreed that the worst imperfection has the form of the transversal buckling mode. Thus, the imperfection function is defined as the product of the initial imperfection amplitudes (C_{20}, C_{40}, C_{50}) and their correspondent displacement component.

For the minor-axis flexural-torsional case, it yields:

$$\begin{aligned} w_{mb+t}^{(1)}(x) &= C_{20}t\sin(\pi x/L)\cos\alpha + C_{50}t\sin(\pi x/L)(y/b_1) \\ w_{mb+t}^{(2)}(x) &= C_{20}t\sin(\pi x/L)\sin\alpha + C_{50}t\sin(\pi x/L)(y/b_2) \end{aligned} \tag{6.4}$$

where the superscripts (1) and (2) refer to the plates 1 and 2, respectively.

For the major-axis flexural-torsional case, it assumes the form:

$$\begin{aligned} w_{Mb+t}^{(1)}(x) &= C_{40} t \sin(\pi x/L)\sin\alpha + C_{50} t \sin(\pi x/L)(y/b_1) \\ w_{Mb+t}^{(2)}(x) &= C_{40} t \sin(\pi x/L)\cos\alpha + C_{50} t \sin(\pi x/L)(y/b_2) \end{aligned} \tag{6.5}$$

For the pure minor-axis bending case, the function is given simply as follows:

$$\begin{aligned} w_{mb}^{(1)}(x) &= C_{20} t \sin(\pi x/L)\cos\alpha \\ w_{mb}^{(2)}(x) &= C_{20} t \sin(\pi x/L)\sin\alpha \end{aligned} \tag{6.6}$$

The sensitivity to geometric imperfections can be analyzed by considering these imperfections in the strain energy functionals and varying the imperfection shape and sign. Figure 6.12 shows the post-buckling paths for the perfect and imperfect equal-leg angle section profiles, with ξ = 1/15 and φ = 0.04, considering increasing values of imperfection in the form of the major-axis bending mode (C_{40}). The curves were obtained through the ($\zeta_{Mb}+\zeta_t$) ROM, as required by the considered geometric and material parameters. It is observed that the imperfect structure exhibits the same increase in the post-critical strength. As expected, the larger the initial imperfection, the greater the bending and torsional amplitudes for the same load ratio. The effects are particularly more substantial when the load approaches the critical value (λ = 1), where deflections grow more prominently, especially the torsional amplitudes. In Figure 6.13, it is shown that initial flexural imperfections do not affect the C_5 x C_4 relationship, indicating that, for the same bending amplitude, the torsional deflection remains the same, regardless of the imperfection level.

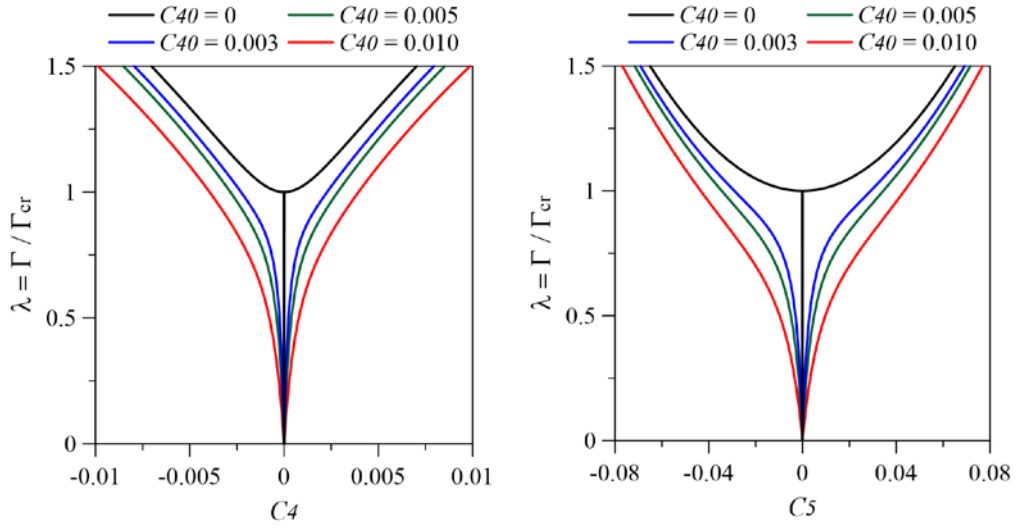

(a) λ x C_4 (b) λ x C_5

Figure 6.12 - Post-buckling paths for equal-leg angle section profiles with initial geometric imperfections in the form of the major-axis bending mode ($C_{40} \neq 0$) ($\beta = 1.0$, $\xi = 1/15$, $\varphi = 0.04$).

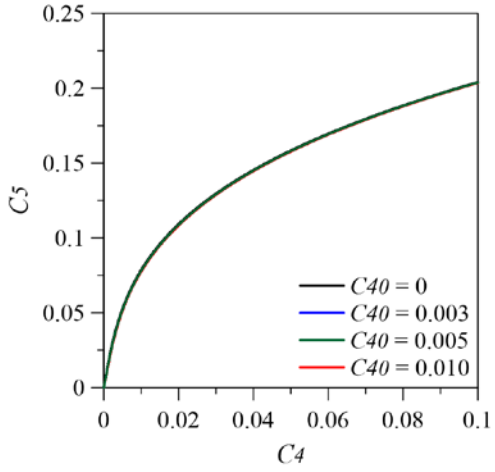

Figure 6.13 - Post-buckling path projections onto the plane C_5 x C_4 for equal-leg angle section profiles with initial geometric imperfections in the form of the major-axis bending mode ($C_{40} \neq 0$) ($\beta = 1.0$, $\xi = 1/15$, $\varphi = 0.04$).

Figure 6.14 presents the post-buckling paths for the same equal-leg angle section profiles as in Figure 6.12 considering now increasing values of initial imperfection in the form of the torsional mode (C_{50}). It can be observed that the post-buckling flexural behaviour of the imperfect structure (Figure 6.14a) shows similarity to the case of flexural imperfection (Figure 6.12a). The curves exhibit the same increase in the post-critical strength as expected for a stable symmetric bifurcation. A distinct behaviour is observed for the torsional amplitudes (Figure 6.14b). As the torsional imperfection increases, the structure exhibits an even

greater torsional stiffness with the paths crossing each other at approximately $C_5 = 0.05$. For $C_{50} = 0.03$, the nonlinear path shows practically a linear behavior, indicating a stiffness gain proportional to the torsional amplitude. Figure 6.15 shows that initial torsional imperfections, unlike flexural imperfection, Figure 6.13, affects the C_5 x C_4 relation. As the imperfection magnitude increases, the amplitude of the flexural mode increases more rapidly.

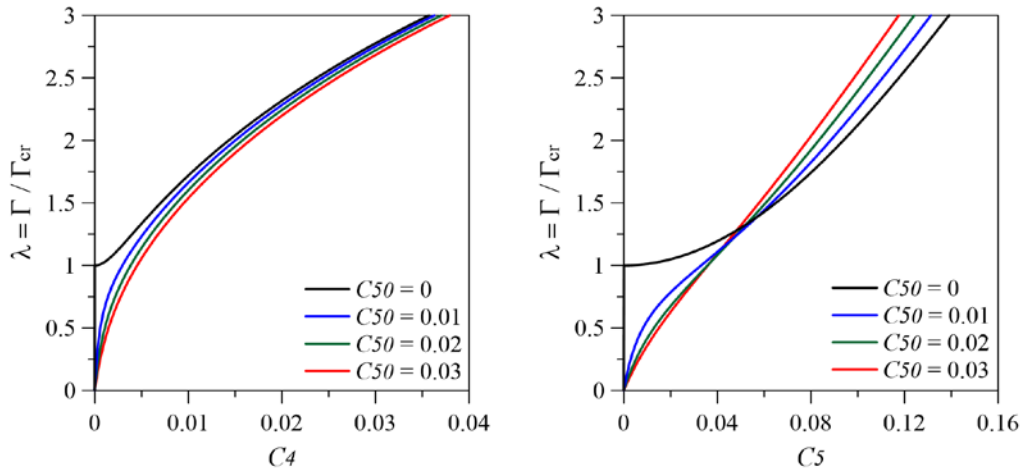

(a) λ x C_4 (b) λ x C_5

Figure 6.14 - Post-buckling paths for equal-leg angle section profiles with initial geometric imperfections in the form of the torsional mode ($C_{50} \neq 0$) ($\beta = 1.0$, $\xi = 1/15$, $\varphi = 0.04$).

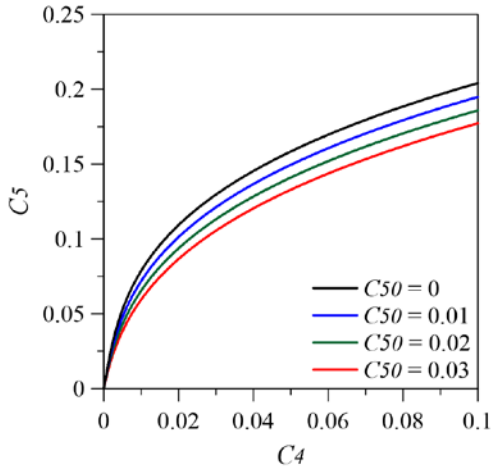

Figure 6.15 - Post-buckling path projections onto the plane C_5 x C_4 for equal-leg angle section profiles with initial geometric imperfections in the form of the torsional mode ($C_{50} \neq 0$) ($\beta = 1.0$, $\xi = 1/15$, $\varphi = 0.04$).

However, initial imperfections are unknown at the design stage, having generally components in all modes when the true imperfection is expanded in terms of the adopted interpolating functions. For plated structures subject to interaction between buckling modes, this topic was discussed in detail by Rasmussen &

Hancock (1988), who proposed an analytical technique for expanding a measured geometric imperfection surface in the buckling modes of a structure. It is generally accepted that in most stability problems the most deleterious imperfection has the form of the buckling mode (Thompson & Hunt, 1973). Both initial flexural and torsional geometric imperfections are considered in Figure 6.16, which is quite similar to that observed in Figure 6.14 and Figure 6.15, corroborating the predominant influence of torsion on the post-buckling strength.

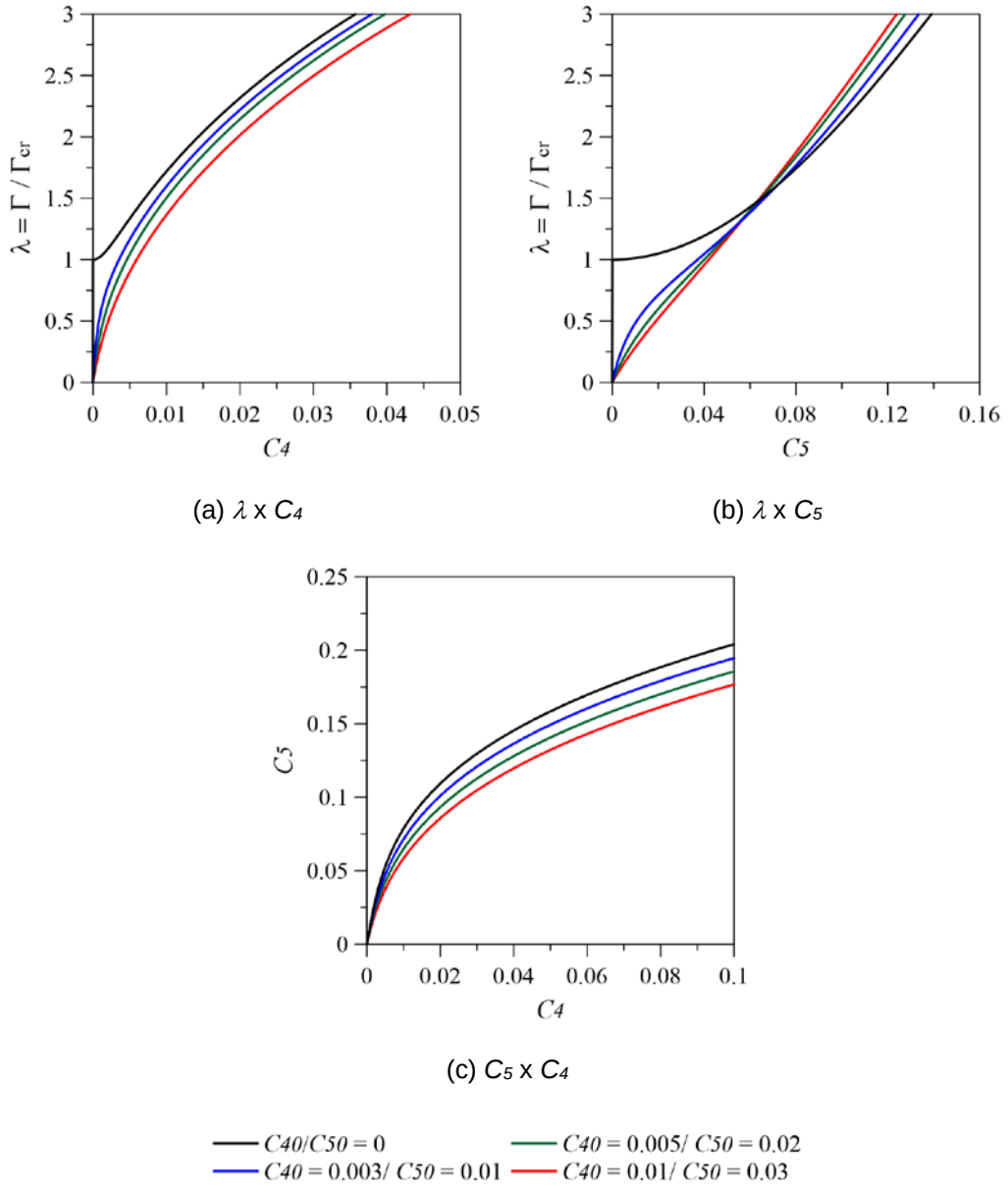

(a) λ x C_4 (b) λ x C_5

(c) C_5 x C_4

Figure 6.16 - Post-buckling paths for equal-leg angle section profiles with initial geometric imperfections with both flexural and torsional components (C_{40} and $C_{50} \neq 0$) ($\beta = 1.0$, $\xi = 1/15$, $\varphi = 0.04$).

It is observed that flexural amplitudes (Figure 6.16a) increase when both imperfections are considered simultaneously, since they have a similar effect on the nonlinear response. The torsional amplitudes (Figure 6.16b) exhibit the same behavior as that observed in Figure 6.15b, but also increases in magnitude. In the C_5 x C_4 projection, Figure 6.16c, exactly the same behavior as in Figure 6.15 is observed, reinforcing the characteristic of this relations for general imperfections.

Figure 6.17 depicts the imperfect nonlinear paths for the case presented in Figure 6.8 ($\beta = 1.0$, $\xi = 1/15$) in which modal participation changes abruptly at $\varphi = 0.032$, considering the same values of φ. Different types of imperfection are considered. For the profiles governed by flexural-torsional buckling, the effect of the three types of imperfection is small and rather similar, converging asymptotically to the solution of the perfect response, displaying high strength reserve. For the profiles governed by minor axis bending, considering the ζ_{mb} ROM, the imperfection in the form of the bending mode leads to large deflections, but the response, as expected, is insensitive to purely torsional imperfections, since this effect is not captured by the ROM (Figure 6.17b). For at $\varphi_t = 0.0323$, the chosen ROM has a strong influence on the results. The response considering (ζ_{Mb}+ζ_t) ROM leads to results similar to those for $\varphi = 0.04$, while the response considering the ζ_{mb} ROM is similar to that for $\varphi = 0.02$. To capture the effect of imperfections in this region, the coupled (ζ_{Mb}+ζ_t+ζ_{mb}) ROM must be used. Results are shown in Figure 6.18, where different types of imperfection lead to similar results, with that considering imperfection components in the three modes leading to the lowest results for small flexural amplitudes.

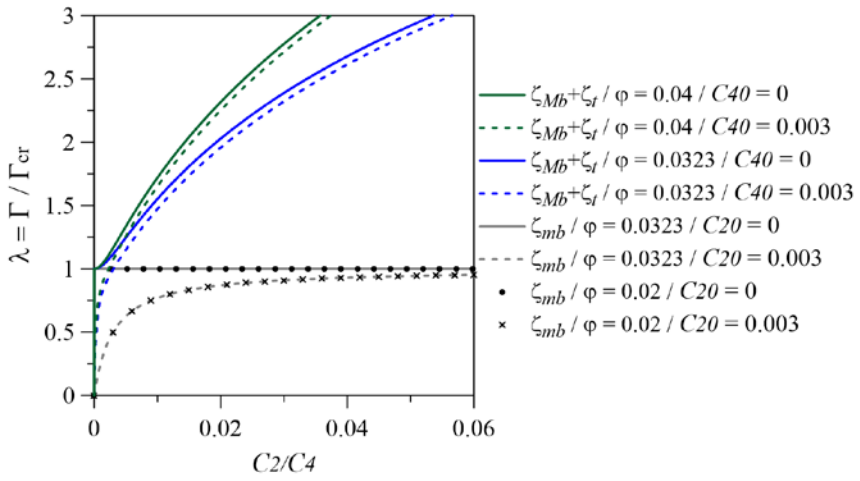

(a) Flexural imperfections (C_{20}, $C_{40} \neq 0$)

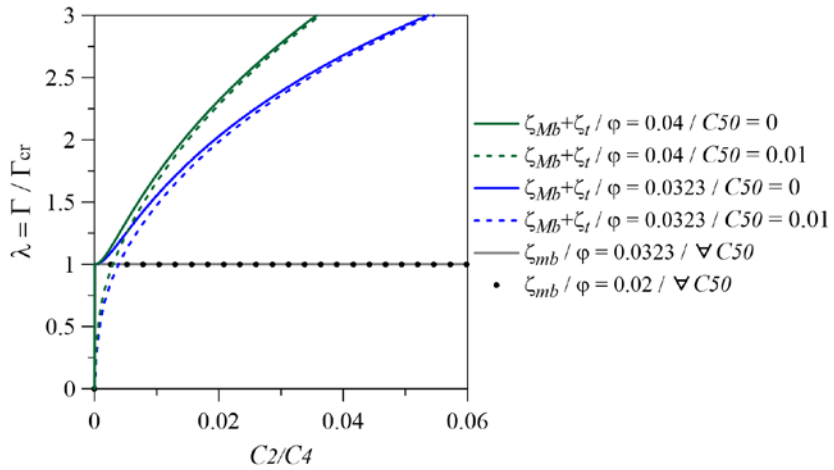

(b) Torsional imperfections ($C_{50} \neq 0$)

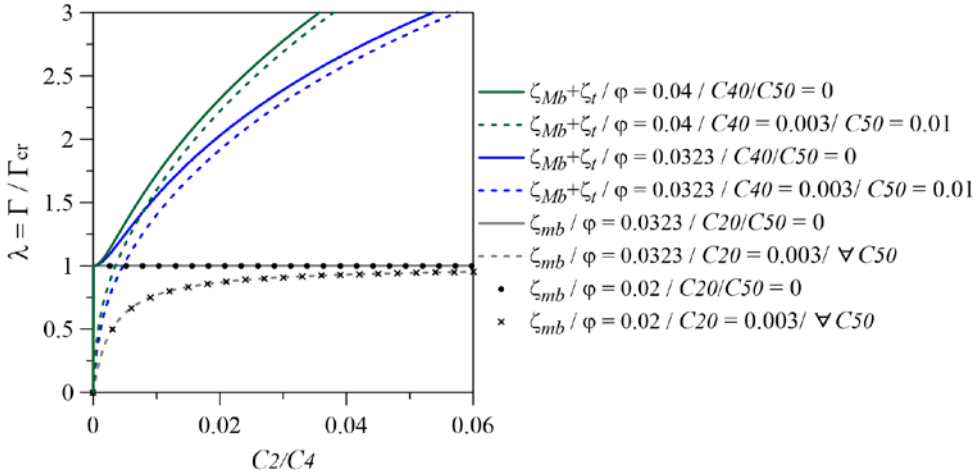

(c) Flexural plus torsional imperfections (C_{20}, C_{40}, $C_{50} \neq 0$)

Figure 6.17 - Influence of initial geometric imperfections on the nonlinear response of equal-leg angle section profiles (β = 1.0, ξ = 1/15) for selected values of φ (see Figure 6.8).

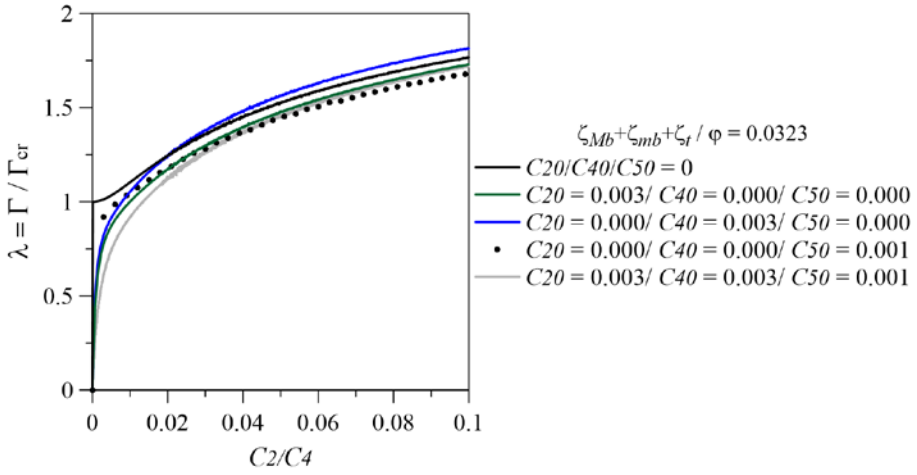

Figure 6.18 - Influence of initial geometric imperfections on the post-buckling paths for equal-leg angle section profiles at the modal transition point, considering the ($\zeta_{Mb}+\zeta_{mb}+\zeta_t$) ROM ($\beta$ = 1.0, φ = 0.0323, ξ = 1/15).

Similar to long equal-leg profiles, unequal-leg profiles exhibit significant bending amplitudes for small increases in load magnitude near the critical load, even for intermediate values of φ (see Figure 6.4). However, the characteristic model for unequal-leg profiles considers minor-axis flexural-torsional behavior, causing post-buckling paths to become sensitive to initial torsional geometric imperfections, unlike what is observed for the pure bending ROM. To illustrate these effects, Figure 6.19 presents the same post-buckling paths as in Figure 6.4 (β = 0.5, ξ = 1/15 and two values of φ), considering the suitable ($\zeta_{mb}+\zeta_t$) ROM, but now subject to initial geometric imperfections in the form of the minor-axis bending mode.

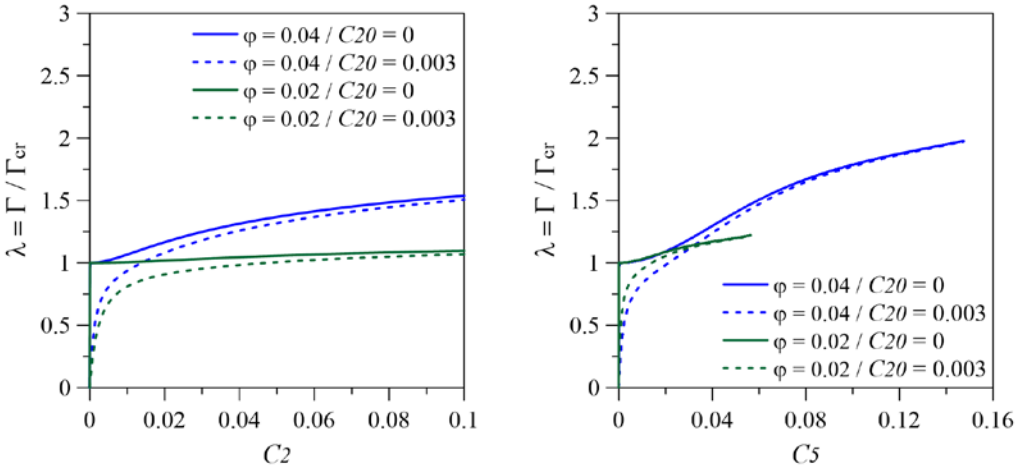

(a) λ x C_2 (b) λ x C_5

Figure 6.19 - Post-buckling paths for unequal-leg angle section profiles with varying wider plate aspect ratio and initial geometric imperfections in the form of the minor-axis bending mode ($C_{20} \neq 0$) ($\beta = 0.5$, $\xi = 1/15$).

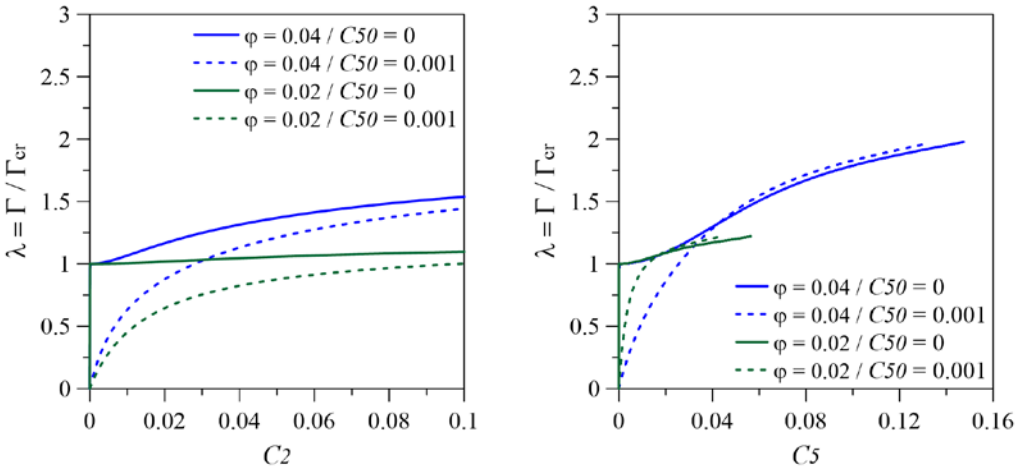

(a) λ x C_2 (b) λ x C_5

Figure 6.20 - Post-buckling paths for unequal-leg angle section profiles with varying wider plate aspect ratio and initial geometric imperfections in the form of the torsional mode ($C_{50} \neq 0$) ($\beta = 0.5$, $\xi = 1/15$).

As expected, the curves in Figure 6.19 exhibit the same behaviour as the ($\zeta_{Mb}+\zeta_t$) ROM (Figure 6.12 and Figure 6.17), where all imperfect paths lead to increasing strength values. The effect of initial imperfections in the form of the torsional mode is presented in Figure 6.20. It is observed that torsional imperfections have a greater influence than those in the form of the bending mode. Comparing Figure 6.20a and Figure 6.21, where both imperfection components are considered, a similarity of results is observed. All responses converge asymptotically from below to the response of the perfect column, showing higher

sensitivity to torsional imperfections, with imperfections in both modes showing the most deleterious influence on the load capacity (Figure 6.21). Due to the influence of minor axis bending, large bending displacements are observed in all cases.

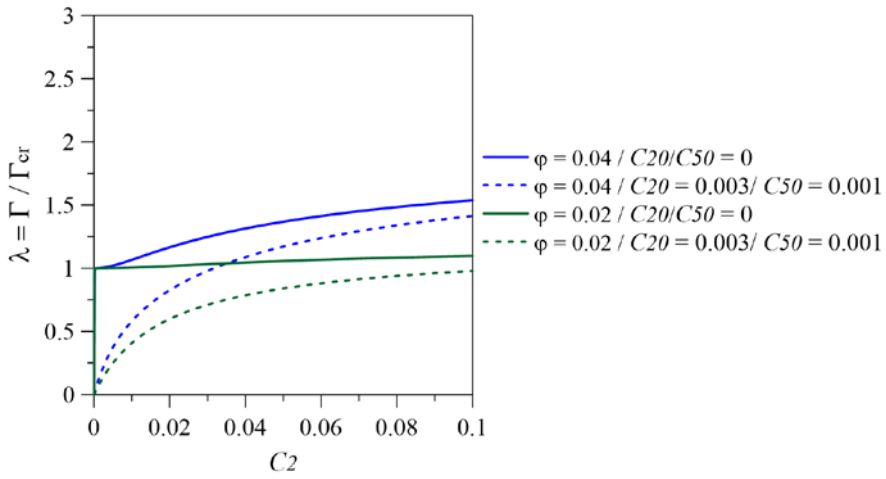

Figure 6.21 - Post-buckling paths for unequal-leg angle section profiles with varying wider plate aspect ratio and initial geometric imperfections with both flexural and torsional components (C_{20} and $C_{50} \neq 0$) ($\beta = 1.0$, $\xi = 1/15$).

7
Nonlinear Vibrations and Parametric Instability

This chapter presents the results of the nonlinear vibration analysis of parametrically excited pultruded angle section profiles. First, the type of nonlinearity of the frequency-amplitude relation for each ROM is identified. Subsequently, the stability of the column under harmonic axial loading is investigated. Parametric instability regions are determined as a function of the frequency and magnitude of the harmonic excitation. The influence of material, damping, and cross-sectional geometry on the parametric instability boundaries is examined. Bifurcation diagrams are obtained using the brute force method (Parker and Chua, 2012) and continuation techniques (Seydel, 1988) to identify the bifurcations associated with the parametric instability boundaries in the force control space, as well as the existence of coexisting solutions. Complementing the analysis, basins of attraction of coexisting solutions are obtained to assess the dynamic integrity of the desired stable solution (trivial solution).

7.1
Frequency-amplitude relations

The ROMs derived in Chapter 4 are now employed to determine the frequency-amplitude relation in each case. The amplitudes remain nondimensional, but now they are time dependent: amplitudes $C_2(\tau)$ and $C_4(\tau)$ are associated with bending and $C_5(\tau)$ is related to torsion, where $\tau = \omega_0 \bar{t}$ is a nondimensional time parameter and ω_0 is the lowest natural linear frequency. Initially, the nonlinear equations of motion of the unloaded and undamped system are numerically solved using the fourth-order Runge-Kutta method together with the shooting method to obtain the frequency-amplitude relation (Seydel, 1988; Del Prado, 2001). The shooting method transforms the initial value problem into a two-point boundary value problem, for the periodicity condition, and then it finds the initial conditions

which lead to periodic response for a given amplitude by employing the Newton-Raphson's method and continuation techniques, enabling the determination of frequency-amplitude relations. The free vibration frequency ratio is defined as:

$$\delta_n = \frac{\omega_n}{\omega_0} \tag{7.1}$$

where ω_n is the nonlinear amplitude dependent frequency obtained by the shooting method.

Figure 7.1 shows the nonlinear frequency–amplitude relation for the equal-leg angle section profile, with $\varphi = 0.04$ and $\xi = 1/30$. The pure torsional ROM (ζ_t) and the major flexural-torsional ROM ($\zeta_{Mb}+\zeta_t$) are considered, as both models exhibit good agreement with the linear results for the considered nondimensional parameters (Figure 5.10). It is observed that the equal-leg angle section column exhibits a nonlinear hardening behavior for both bending and torsional amplitudes, with increasing nonlinear stiffness as the vibration amplitudes increases. A slightly stronger hardening behavior is observed when only the torsional mode is considered, as shown in Figure 7.1b. This comparison shows that the torsion in the main responsible for the hardening effect.

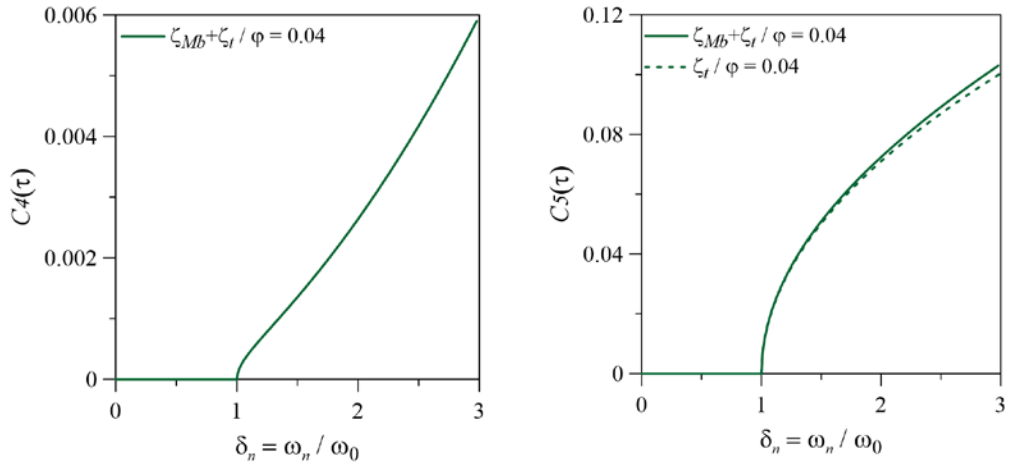

(a) $C_4(\tau)$ x δ_n (b) $C_5(\tau)$ x δ_n

Figure 7.1 - Frequency–amplitude relations for an equal-leg angle section profile considering pure torsional and the coupled ($\zeta_{Mb}+\zeta_t$) ROM ($\beta = 1.0$, $\varphi = 0.04$, $\xi = 1/30$).

Figure 7.2 presents the frequency-amplitude relations for an equal-leg angle profile with $\varphi = 0.02$ and $\xi = 1/15$, considering both the pure bending, (ζ_{mb}) ROM, and the flexural-torsional model with minor axis bending, ($\zeta_{mb}+\zeta_t$) ROM, as the two models exhibit good agreement with GBTuL in the linear analysis when the wider

plate aspect ratio reaches $\varphi = 0.02$ (Figure 5.14). As observed, the asymmetric angle section profile also exhibits a hardening nonlinearity when the coupled ROM is considered (Figure 7.2a). However, the observed stiffness gain is small, even for large vibration amplitudes. When torsional effects are disregarded, (ζ_{mb}) ROM, the frequency-amplitude relation is nearly linear, indicating a low stiffness gain, which is typical of columns. The proximity of both models for $\varphi = 0.02$ is confirmed when observing low values of torsional amplitude for the coupled ROM compared to the values of bending amplitude (Figure 7.2b). These results agree with the results of the post-critical paths, where significant displacements were observed for small increases in loading levels in models involving minor axis bending and low values of φ (Figure 6.4).

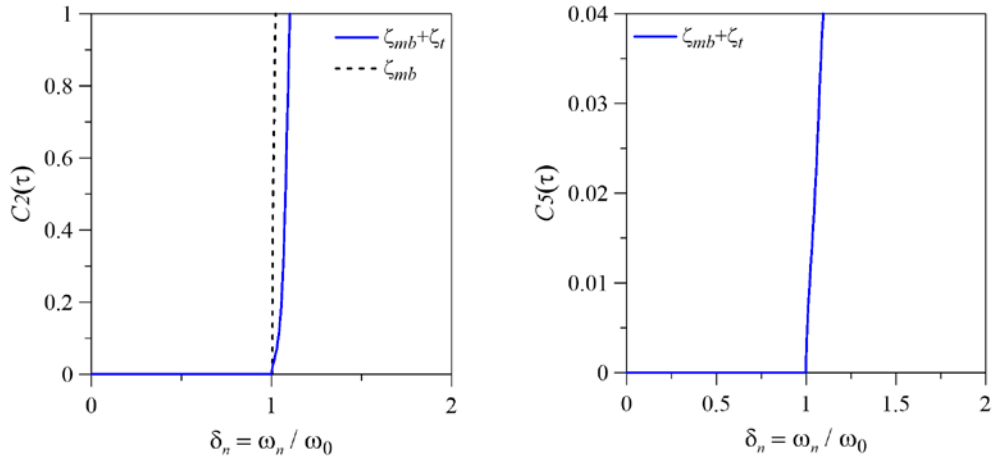

(a) $C_2(\tau)$ x δ_n (b) $C_5(\tau)$ x δ_n

Figure 7.2 - Frequency–amplitude relation for an equal-leg angle section profile considering pure bending and the coupled (ζ_{mb}+ζ_t) ROM ($\beta = 0.5$, $\varphi = 0.02$, $\xi = 1/15$).

7.2
Dynamical systems

Here basic concepts of nonlinear dynamical systems are summarized. Bifurcation diagrams of nonlinear dynamical systems illustrate how the fixed points of the Poincaré map evolve with a specific control parameter. Through a bifurcation diagram, one can identify equilibrium solutions, periodic orbits, quasi-periodic orbits, and chaotic solutions, as well as the values of the control parameter where qualitative changes in the system's behavior occur, known as bifurcation points. By varying one of the system's control parameters, a periodic solution may lose its

stability, and the type of the associated bifurcation depends on how the Floquet multipliers related to the fixed points of the Poincaré map leave the unit circle (Floquet, 1883; Teschl, 2012).

Here, bifurcation diagrams are obtained through a brute force approach (Parker and Chua, 2012) increasing and decreasing the control parameter to identify the dynamic jumps between coexisting stable equilibrium branches. In the brute force approach the first 700 forcing periods are discarded as transient, and the subsequent 200 periods are utilized for the diagram. To understand the connection between these stable branches the bifurcation diagrams are obtained by continuation techniques (Seydel, 1988; Del Prado, 2001), employing the Newton-Raphson method in conjunction with an arc-length continuation approach. This method enables to find both stable and unstable paths with low periodicity. The classification as stable or unstable is determined through the application of Floquet theory (Floquet, 1883; Teschl, 2012; Del Prado, 2001; Mailybaev, 2023). Thompson & Stewart (2002) present a comprehensive description of the Floquet theory.

Considering only the cases found in the present study, periodic solutions can exhibit bifurcation through symmetry-breaking (pitchfork), cyclic fold (saddle-node), and period-doubling bifurcation (flip). The pitchfork and saddle-node bifurcations occur when a real eigenvalue leaves the unit circle through the +1 point, as illustrated in Figure 7.3a. On the other hand, the flip bifurcation occurs when the real eigenvalue leaves the unit circle through the –1 point, as indicated in Figure 7.3b. Finally, a Hopf bifurcation, associated with the emergence of quasi-periodic solutions, is identified when a pair of complex eigenvalues crosses the unit circle, as illustrated in Figure 7.3c.

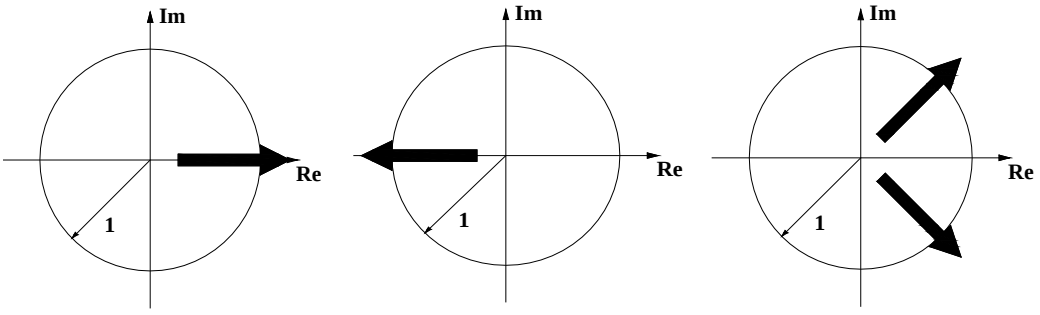

(a) +1 (b) -1 (c) Complex conjugate

Figure 7.3 - The way Floquet multipliers can surpass the unit circle (stability region) (Del Prado, 2001).

Both pitchfork and flip bifurcations can be divided into two groups: supercritical and subcritical (Figure 7.4). In either case, locally, there is a branch of stable fixed points (trivial solution in the parametrically excited system) that becomes unstable after the bifurcation point. In the supercritical case, after the bifurcation point, two branches of stable fixed points emerge in the pitchfork bifurcation, while in the flip bifurcation, only one branch of stable solutions arises, but with twice the period of the initial solution. In the subcritical case, there are locally two branches of unstable fixed points before the pitchfork bifurcation point and only one branch of unstable fixed points before the flip bifurcation, again with twice the period of the initial solution. Therefore, the pitchfork bifurcation, in both cases, gives rise to two distinct solutions and implies a symmetry-breaking in the response. Additionally, the supercritical bifurcation is characterized by being continuous, while the subcritical one is discontinuous or catastrophic (Thompson & Stewart, 2002).

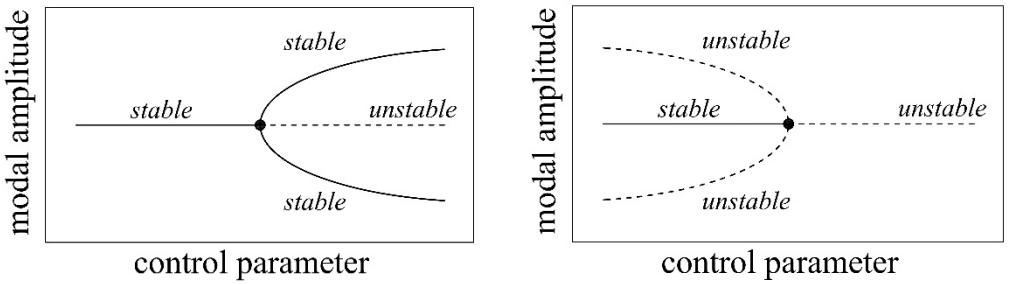

(a) Supercritical (a) Subcritical

Figure 7.4 - Pitchfork and flip bifurcations.

For the saddle-node bifurcation, the branch of stable periodic solutions and the branch of unstable periodic solutions are created or annihilated simultaneously at the bifurcation point, as shown in Figure 7.5.

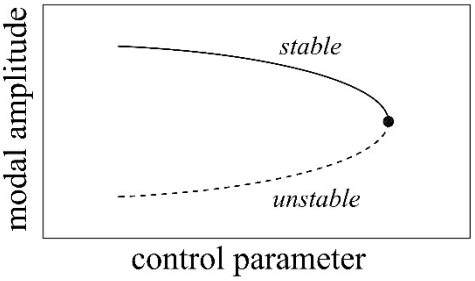

Figure 7.5 - Saddle-node bifurcation.

The bifurcation diagrams are obtained to investigate the type of bifurcation that occurs when the trivial solution becomes unstable and to identify regions where coexisting stable solutions arises. In such cases, basins of attraction are generated to clarify how the attractors of the stable solution evolve as the control parameter increases. They are obtained by employing the cell-to-cell method developed by Hsu (Hsu, 2013; Del Prado, 2001). Also, the bifurcation diagrams illustrate the sequence of bifurcations within the unstable region of the Ince-Strutt diagrams also called Mathieu stability charts (Bolotin, 1964; Xie, 2006).

7.3
Parametric instability analysis

The dynamic stability of the column is analyzed considering a harmonic axial excitation in the form:

$$\bar{N}(t) = N\cos(\omega\bar{t}) \tag{7.2}$$

where N is the magnitude of the forcing harmonic excitation and ω is the forcing frequency. Dividing the applied load by the static critical axial load, N_{cr}, and considering again the nondimensional time $\tau = \omega_0\bar{t}$, the nondimensional axial excitation takes the form:

$$\bar{Q}(\tau) = \lambda\cos(\delta\tau) \tag{7.3}$$

where λ is the nondimensional axial load parameter, as defined in eq. 6.1 and δ is the nondimensional frequency ratio, written as:

$$\delta = \frac{\omega}{\omega_0} = \frac{\Omega}{\Omega_0} \tag{7.4}$$

where Ω_0 is the fundamental frequency parameter, as defined in eq. 5.20, and Ω is the nondimensional forcing frequency parameter, given by:

$$\Omega^2 = \frac{\omega^2 \rho L^2 \left(1 - \nu_{12}\nu_{21}\right)}{\pi^2 E_1} \tag{7.5}$$

Thus, the forcing control space is defined as (λ, δ). Additionally, in the following analysis, Ξ is the dimensionless viscous damping parameter, adopted as Ξ = 1%, except when studying the influence of different values.

This leads to differential equations of motion of the Mathieu-Hill type with time varying coefficients. The Mathieu equation has two types of solutions - stable and unstable, depending only on two parameters. In structural systems under periodic axial loads the initial membrane state, i.e., the trivial solution, becomes unstable, leading to flexural motions, the so-called parametric instability (Sugiyama et al., 2019). Each Mathieu instability region is constituted by two transition curves called a tongue for the undamped case with the minimum value corresponding to a critical load equal to zero. These minima occur at the natural frequency and its multiples and submultiples ($n\omega_0/m$, n, m = 1, 2, 3…), being the most important region at $2\omega_0$. Kovacic et al. (2018) presented recently a detailed analysis of Mathieu's equation and its generalizations together with an overview of stability charts and their features. The parametric instability of axially loaded columns and plates has been for many years an important research topic in nonlinear dynamics (Xie, 2006; Nayfeh & Mook, 2008; Mailybaev, 2023). A stability chart of classical Mathieu's equation can be analytically obtained by various perturbation methods or harmonic balancing or by using numerical integration in conjunction with Floquet theory. The latter approach is adopted here.

The parametric stability boundary corresponds to the maximum axial load parameter where the trivial solution is stable, that is, after this point the column begins to exhibit nontrivial lateral vibrations. These boundaries are obtained by solving the nonlinear equations of motion for the damped system using the brute force method and continuation techniques across a wide range of frequency ratios. The time responses are obtained by the fourth-order Runge-Kutta method with a

constant time step and a time increment of 1/400 of the period of the harmonic force. The axial load parameter is gradually increased while maintaining constant the frequency ratio until non-trivial solutions emerge.

Figure 7.6 shows the parametric stability boundary of the trivial solution in the forcing control space (λ, δ) for the equal-leg angle section profile, with $\varphi = b/L = 0.02$ and $\xi = t/b = 1/30$, using the adequate ($\zeta_{Mb}+\zeta_t$) ROM. The chart exhibits two instability regions (valleys). The deeper valley, in the neighborhood of $\delta = 2.0$, is associated with the principal parametric resonance region, while the second instability region is found to the left ($\delta = 1.0$) and referred to as fundamental resonance region. These two regions are typically considered the most important in structural dynamics, as the other instability regions to the left correspond to higher-order resonances ($\delta = 2/3, 1/2\ldots$). It is observed that in both instability regions that the boundary is well below $\lambda = 1$, indicating that the column becomes unstable under dynamic axial load magnitudes considerably lower than the static buckling load. Between the instability regions, on the other hand, the parametric instability loads can assume values reasonably higher than the static critical load. These results underscore the dangerous implications of parametric instability in structural systems with low levels of damping.

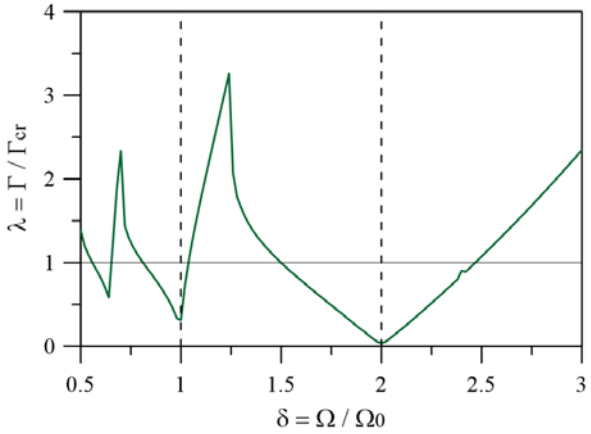

Figure 7.6 - Parametric stability boundary in the forcing control space (λ, δ) for the equal-leg angle section profile ($\beta = 1.0$, $\xi = 1/30$, $\varphi = 0.02$).

Figure 7.7 shows the bifurcation diagrams of the Poincaré map for bending and torsional vibration amplitudes, having as control parameter the axial load parameter and considering the frequency ratio $\delta = 0.9$. These bifurcation diagrams are associated with the left transition curve of the fundamental resonance region in the stability chart (Figure 7.6). As observed, the angle profile undergoes at $\lambda = 0.71$

a supercritical pitchfork bifurcation, giving rise to two stable new branches of solution with period one. Figure 7.8 shows the projections of phase-portraits for $\lambda = 1$, where it is possible to observe the two coexisting period one stable solutions. Both solutions are observed to lack symmetry. The dots indicate the fixed points of the Poincaré map, which are the same as those used to trace the bifurcation diagrams. The Poincaré map represents a mapping obtained by following intersections of the spatial dynamic response in a subspace defined by surfaces of section. Thus, closed orbits in the dynamical system correspond to fixed points in the Poincaré map.

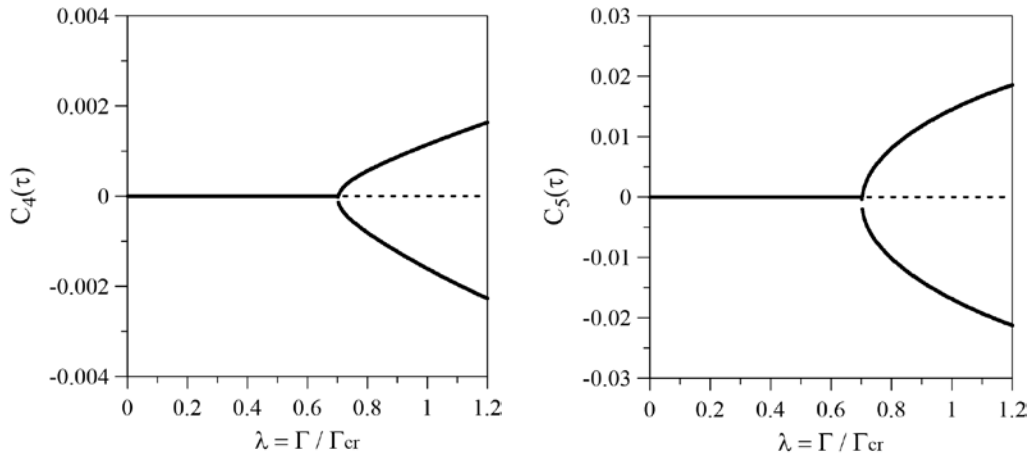

(a) $C_2(\tau)$ x λ (b) $C_3(\tau)$ x λ

Figure 7.7 - Bifurcation diagrams for the frequency ratio $\delta = 0.9$ ($\beta = 1.0$, $\xi = 1/30$, $\varphi = 0.02$).

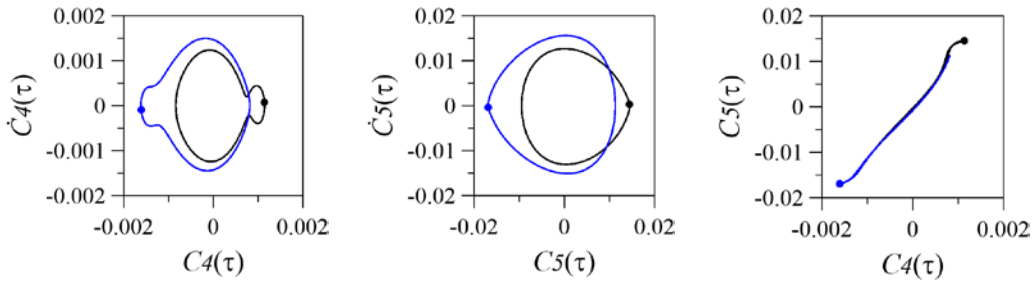

(a) $\dot{C}_4(\tau)$ x $C_4(\tau)$ (b) $\dot{C}_5(\tau)$ x $C_5(\tau)$ (c) $C_5(\tau)$ x $C_4(\tau)$

Figure 7.8 - Phase-plane projections and fixed points of the Poincaré map for $\delta = 0.9$ and $\lambda = 1.0$.

Figure 7.9 shows the bifurcation diagrams for bending and torsional vibration amplitudes, considering the frequency ratio $\delta = 1.05$. Here, the trivial solution becomes unstable due to a subcritical pitchfork bifurcation at $\lambda = 1.17$, originating two unstable period one solutions that evolve, as the control parameter decreases,

up to a saddle-node bifurcation around $\lambda = 0.34$ (see the non-symmetry of the solution branches). After the saddle point, the two solutions become stable, thus two non-trivial solutions coexist with the stable trivial solution in the interval $0.34 \leq \lambda \leq 1.17$. Figure 7.10 shows the projections of the response for $\lambda = 1$, where it is observed the three coexisting stable solutions: the trivial solution and the two non-trivial period one solutions, a typical response of the right transition curve of the fundamental parametric resonance region.

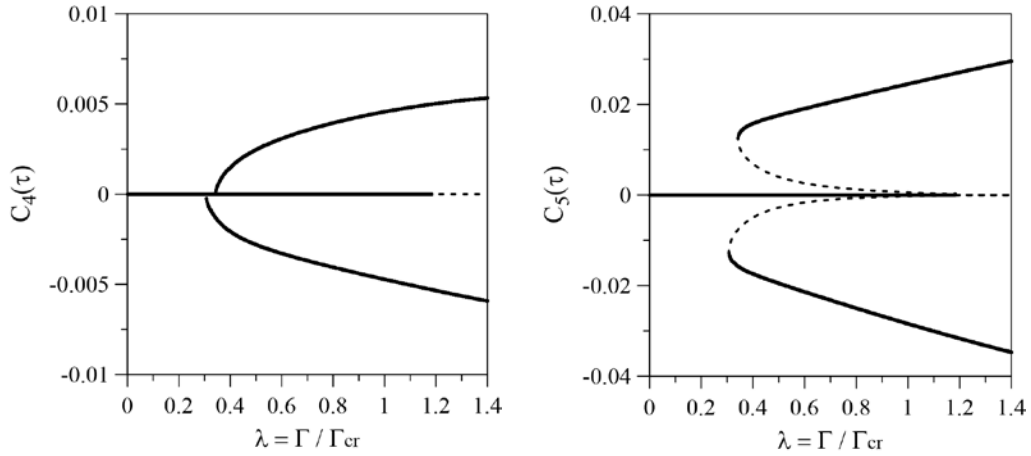

(a) $C_4(\tau)$ x λ (b) $C_5(\tau)$ x λ

Figure 7.9 - Bifurcation diagrams for the frequency ratio $\delta = 1.05$ ($\beta = 1.0$, $\xi = 1/30$, $\varphi = 0.02$).

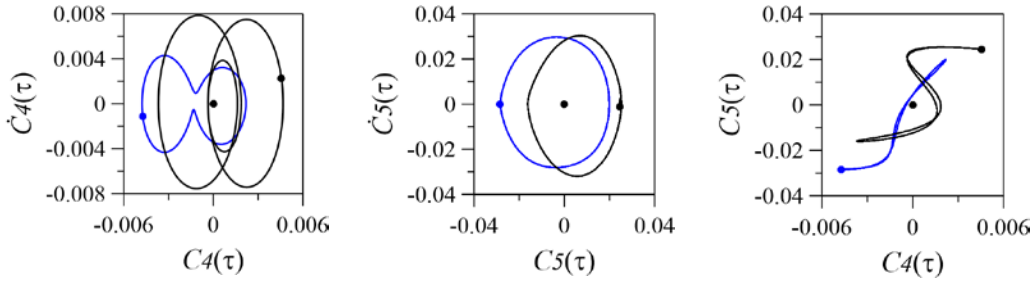

(a) $\dot{C}_4(\tau)$ x $C_4(\tau)$ (b) $\dot{C}_5(\tau)$ x $C_5(\tau)$ (c) $C_5(\tau)$ x $C_4(\tau)$

Figure 7.10 - Phase-plane projections and fixed points of the Poincaré map for $\delta = 1.05$ and $\lambda = 1.0$.

Figure 7.11 shows the time response of the bending and torsional amplitudes corresponding to the black orbit in Figure 7.10 ($\delta = 1.05$, $\lambda = 1.0$). The response considers the last four oscillations of the periodic solution in the steady-state regime ($\tau = \omega_0 t > 1975$). The period of the solution (T_s) is given by $T_s = 2\pi/\delta \cong 6.0$.

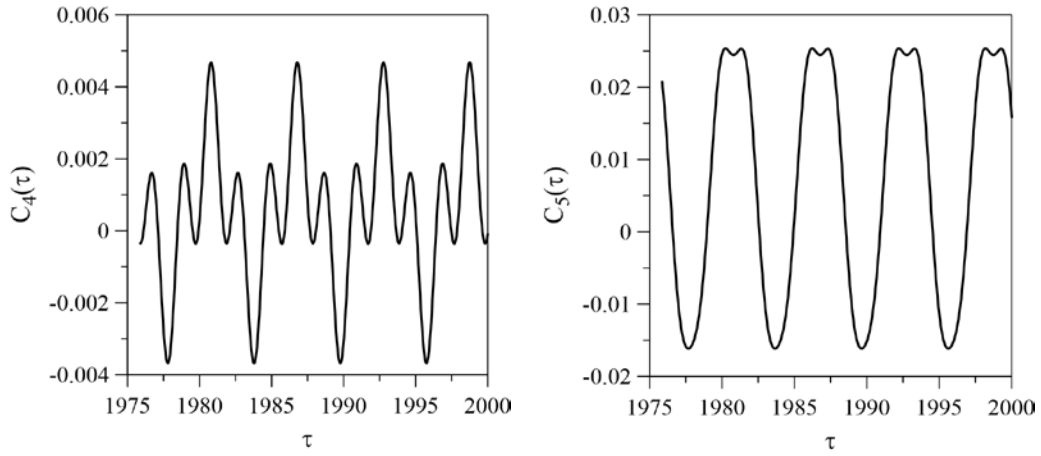

(a) $C_4(\tau)$ x τ (b) $C_3(\tau)$ x τ

Figure 7.11 - Time response of bending and torsional amplitudes at $\delta = 1.05$ and $\lambda = 1.0$ (black orbit in Figure 7.10).

Figure 7.12 shows the bifurcation diagrams considering the frequency ratio $\delta = 1.8$. The trivial solution becomes unstable due to a supercritical flip (period doubling) bifurcation, that remains stable for increasing forcing magnitudes over a large region of the parameter λ. Figure 7.13 shows the projections of phase-portraits for $\lambda = 1$, depicting the 2T periodic stable solution that arise after the bifurcation point (in the present work the notation kT is adopted to label a periodic solution with a period equal to k times the forcing period).

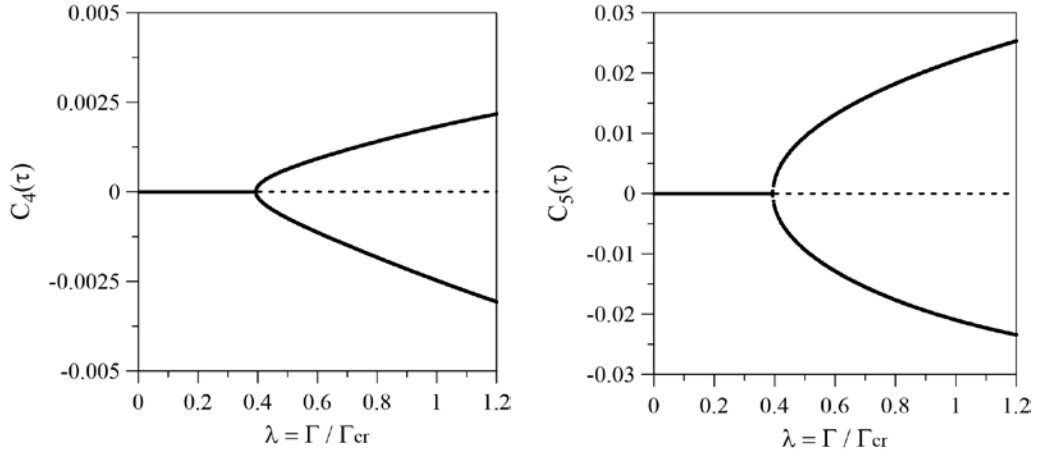

(a) $C_4(\tau)$ x λ (b) $C_5(\tau)$ x λ

Figure 7.12 - Bifurcation diagrams for the frequency ratio $\delta = 1.8$ ($\beta = 1.0$, $\xi = 1/30$, $\varphi = 0.02$).

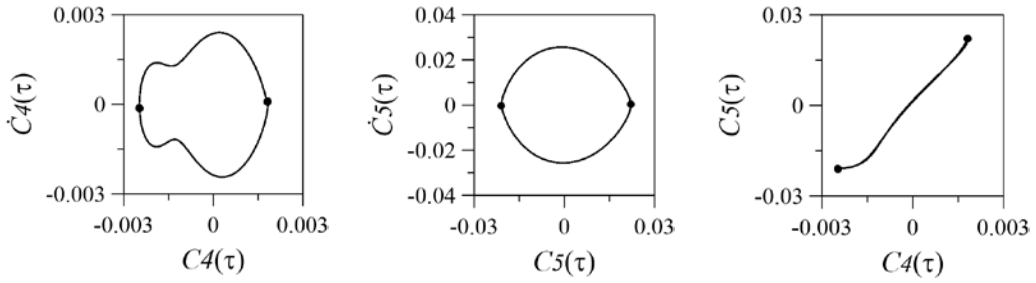

(a) $\dot{C}_4(\tau)$ x $C_4(\tau)$ (b) $\dot{C}_5(\tau)$ x $C_5(\tau)$ (c) $C_5(\tau)$ x $C_4(\tau)$

Figure 7.13 - Phase-plane projections and fixed points of the Poincaré map for $\delta = 1.8$ and $\lambda = 1.0$.

For $\delta = 2.2$ (Figure 7.14), corresponding to the right transition curve of the principal parametric resonance region, the trivial solution undergoes a subcritical flip bifurcation at $\lambda = 0.41$. The nontrivial stable solution starts at $\lambda = 0.13$, displaying a large number of fixed points of the Poincaré map. This solution undergoes a bifurcation at $\lambda = 0.21$, giving rise to a stable 2T solution. Figure 7.15a-c shows the projections of phase-portraits for $\lambda = 0.3$, where it is possible to observe the two coexisting stable solutions: the trivial solution and the non-trivial 2T solution, a typical response in the principal parametric resonance region (2:1 resonant response).

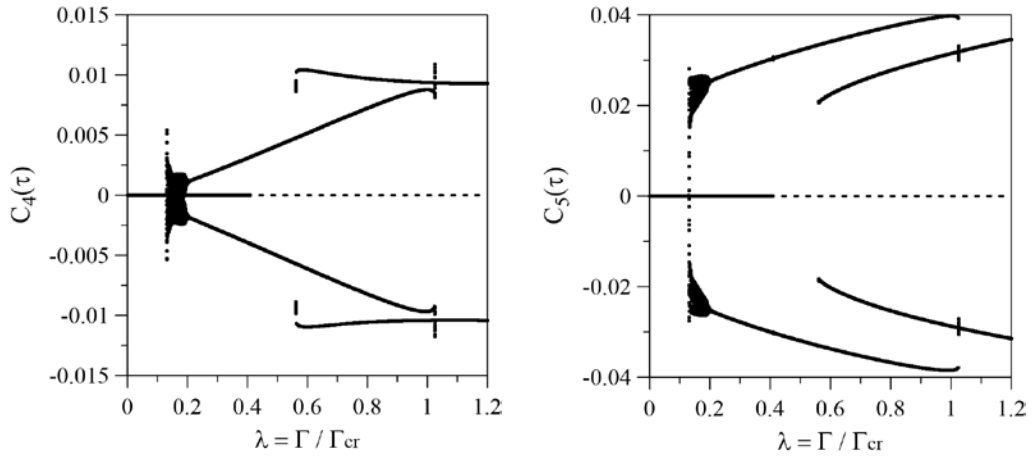

(a) $C_2(\tau)$ x λ (b) $C_5(\tau)$ x λ

Figure 7.14 - Bifurcation diagrams for the frequency ratio $\delta = 2.2$ ($\beta = 1.0$, $\xi = 1/30$, $\varphi = 0.02$).

For higher values of the load parameter λ, the emergence of a second non-trivial 2T stable solution, with larger bending amplitudes and lower torsional amplitudes (Figure 7.14), is observed. This new solution is depicted in blue on the

phase-planes shown in Figure 7.15d-f, and its time steady response is illustrated in Figure 7.16. The period of the solution is given by $T_s = 2\pi/\delta \cong 2.9$. The time response displays four complete oscillation cycles, with two periods required to complete each cycle ($2T_s$), illustrating the period-doubling bifurcation.

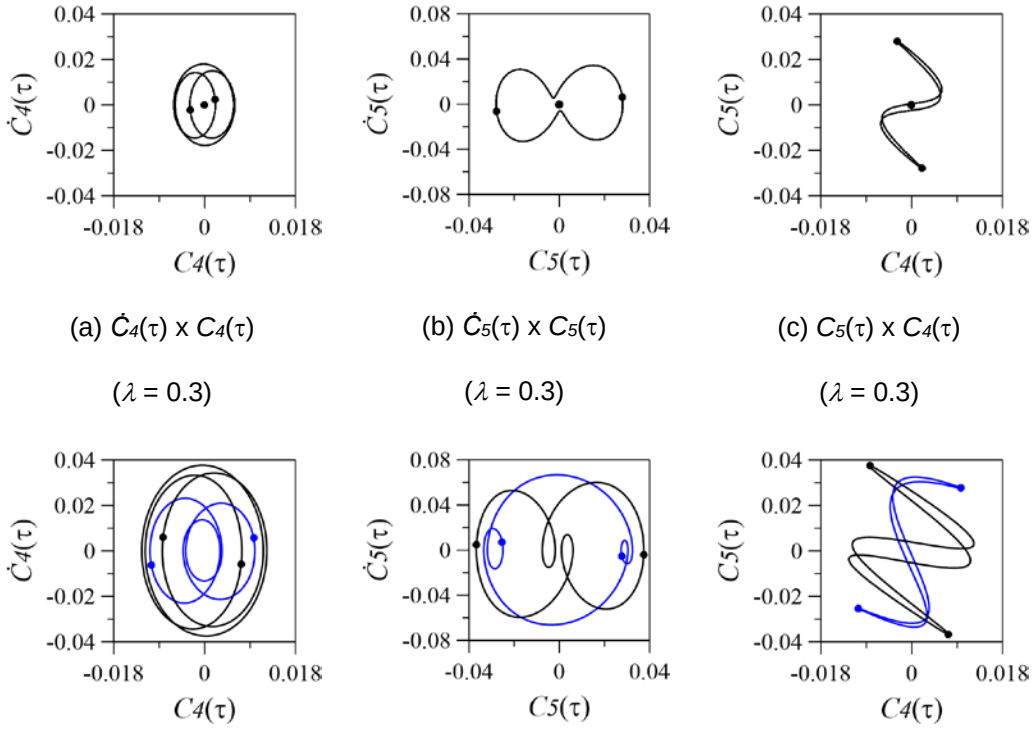

(a) $\dot{C}_4(\tau)$ x $C_4(\tau)$ (λ = 0.3)

(b) $\dot{C}_5(\tau)$ x $C_5(\tau)$ (λ = 0.3)

(c) $C_5(\tau)$ x $C_4(\tau)$ (λ = 0.3)

(d) $\dot{C}_4(\tau)$ x $C_4(\tau)$ (λ = 0.8)

(e) $\dot{C}_5(\tau)$ x $C_5(\tau)$ (λ = 0.8)

(f) $C_5(\tau)$ x $C_4(\tau)$ (λ = 0.8)

Figure 7.15 - Phase-plane projections and fixed points of the Poincaré map for δ = 2.2 and selected values of λ.

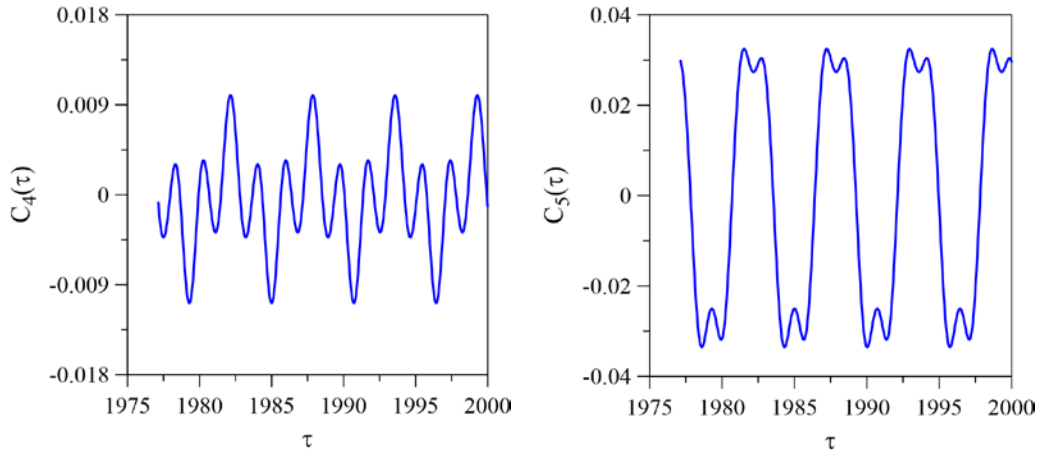

(a) $C_4(\tau)$ x τ (b) $C_5(\tau)$ x τ

Figure 7.16 - Time response of bending and torsional amplitudes at $\delta = 2.2$ and $\lambda = 0.8$ (blue orbit in Figure 7.15d-f).

In Figure 7.14, the Poincaré map is rather complex after $\lambda = 0.13$. In order to investigate this region, Figure 7.17a and c provide a zoom chart of the interval $0.1 \leq \lambda \leq 0.2$. Figure 7.17b and d display the phase-plane projections for $\lambda = 0.16$, where it is possible to observe that the fixed points of the Poincaré map is characteristic of a quasi-periodic solution. The phenomenon of quasi-periodicity in deterministic dynamical systems describes stationary solutions that neither exhibit a finite period length nor are chaotic.

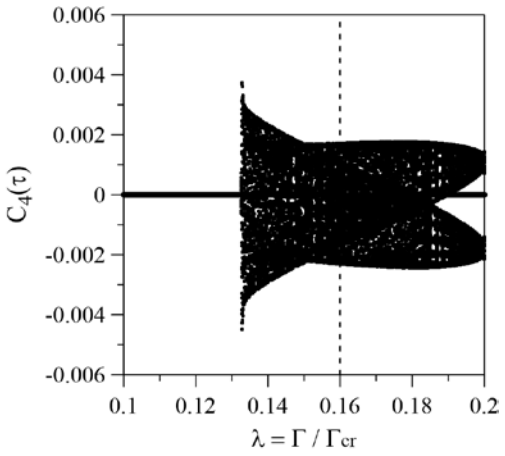

(a) $C_4(\tau)$ x λ

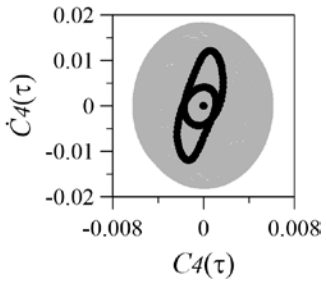

(b) $\dot{C}_4(\tau)$ x $C_4(\tau)$ (λ = 0.16)

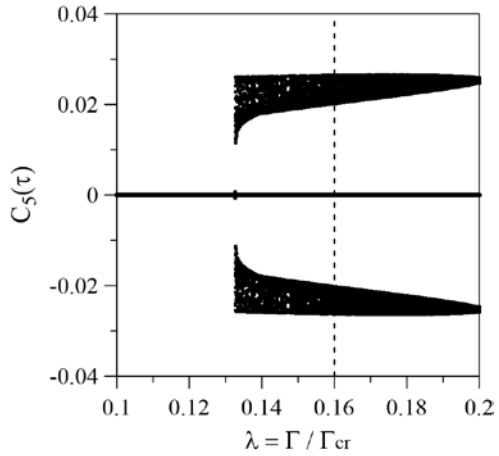

(c) $C_5(\tau)$ x λ

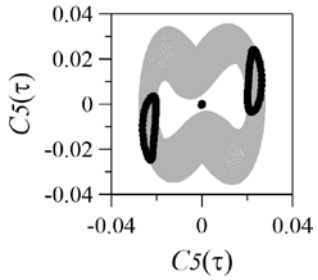

(d) $\dot{C}_5(\tau)$ x $C_5(\tau)$ (λ = 0.16)

Figure 7.17 - Quasi-periodic solutions in the bifurcation diagrams for the frequency ratio δ = 2.2 (0.1 ≤ λ ≤ 0.2).

In Figure 7.18, the time responses of the bending and torsional amplitudes corresponding to the quasi-periodic solution at λ = 0.16 are shown.

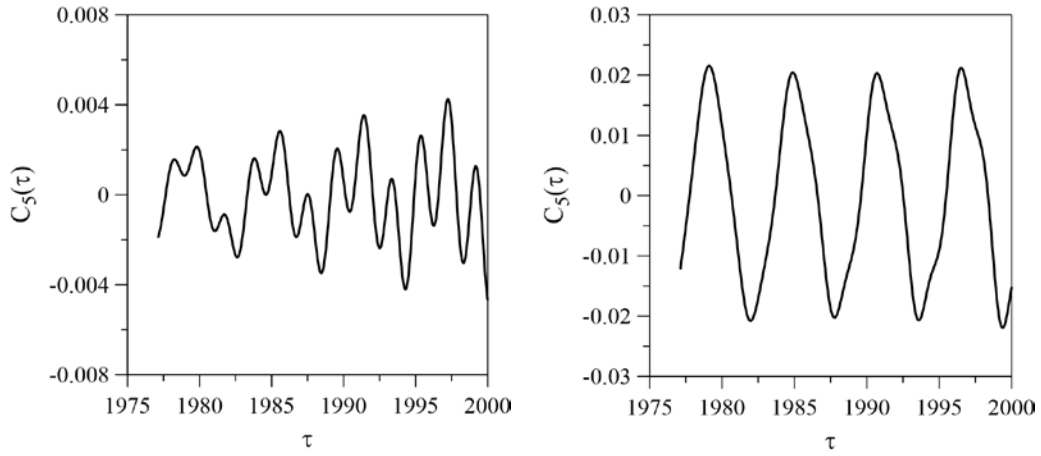

(a) $C_5(\tau)$ x τ (b) $C_5(\tau)$ x τ

Figure 7.18 - Time response for bending and torsional amplitudes at δ = 2.2 and λ = 0.16.

In practical terms, information on stability boundaries alone is not sufficient for evaluating the safety of a given structure. To assess the safety of a structure, the behavior of the basins of attraction of coexisting solutions should be analyzed. Figure 7.19 shows cross-sections of the basins of attraction, considering two values of the load parameter (λ = 0.3, 0.8) and δ = 2.2 (associated with the bifurcation diagrams in Figure 7.14). The basins of attraction are obtained discretizing the phase-plane of interest in a mesh of 200 x 200 cells, using the cell-to-cell mapping approach (Hsu, 2013; Del Prado, 2001).

In Figure 7.19a and c (load parameter equal to λ = 0.3), it is observed that the basin of attraction of the trivial stable solution (in gray) is much smaller than the basin of the 2T solution (in red). This means that although this load level is much smaller than the parametric instability load (λ = 0.41), small disturbances may lead to an escape to the non-trivial periodic solutions. The basin of the trivial solution decreases swiftly and is annihilated after the subcritical flip bifurcation point (λ = 0.41). This means that the profile in this region exhibits low dynamic integrity measures, a topic worth of investigation in future studies (Lenci et al., 2013; Thompson, 2019).

For higher load parameters (λ = 0.8), there are two coexisting 2T attractors. The original periodic attractor (basin in red) and the new periodic attractor (basin in blue), associated with the blue orbit in Figure 7.15d-f.

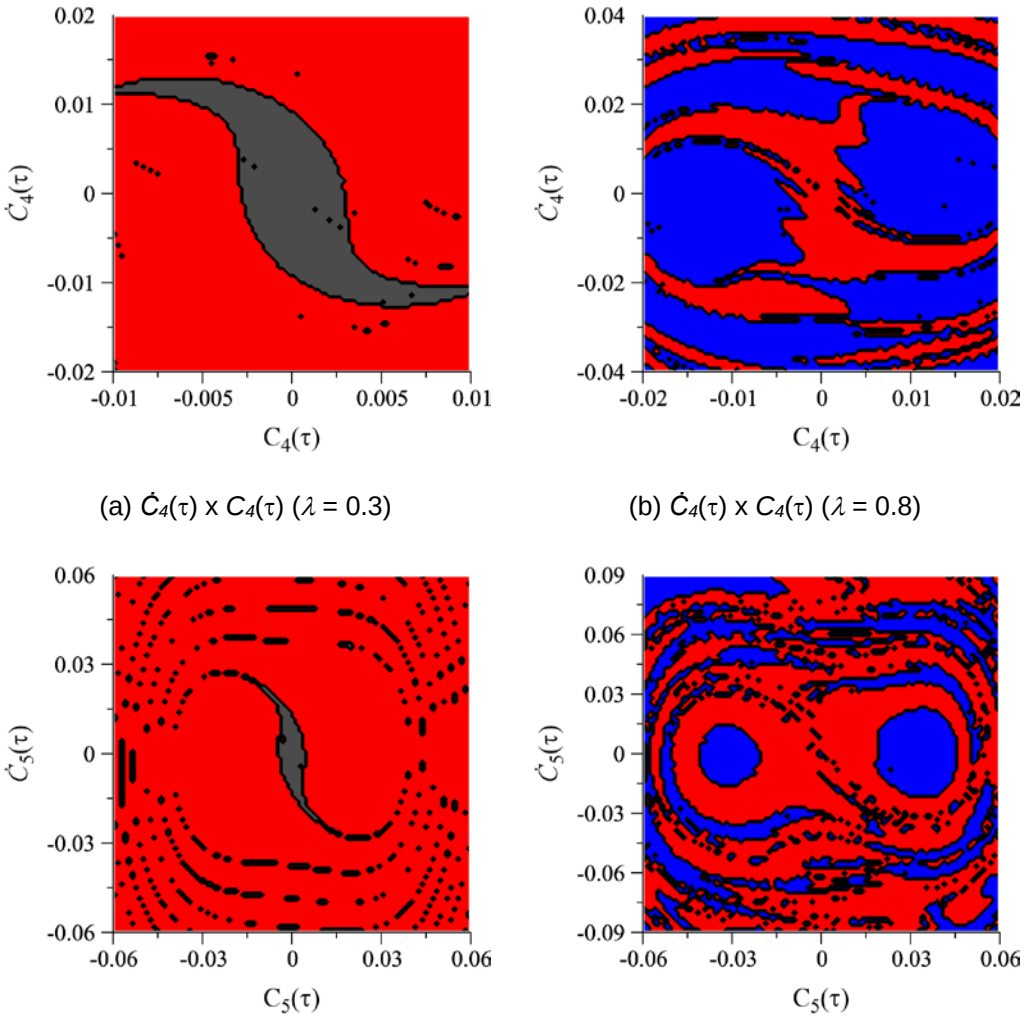

(a) $\dot{C}_4(\tau)$ x $C_4(\tau)$ (λ = 0.3)

(b) $\dot{C}_4(\tau)$ x $C_4(\tau)$ (λ = 0.8)

(c) $\dot{C}_5(\tau)$ x $C_5(\tau)$ (λ = 0.3)

(d) $\dot{C}_5(\tau)$ x $C_5(\tau)$ (λ = 0.8)

Figure 7.19 - Evolution of the basins of attraction (cross-sections) of the coexisting solutions for selected values of load parameter and δ = 2.2.

As observed, the results show that the principal parametric resonance region exhibits flip bifurcations, leading to period-doubling, while in the fundamental resonance region, pitchfork-type bifurcations are found, resulting in two distinct periodic solutions. These two bifurcation scenarios alternate as the frequency ratio δ increases, as shown in Figure 7.20. In each region the left-hand side transition curve is associated with a stable bifurcation of the trivial solution, while the right-hand side transition curve is associated with an unstable bifurcation. These bifurcation sequences are typical of hardening nonlinear structural systems, agreeing with the frequency-amplitude relations (Figure 7.1 and Figure 7.2).

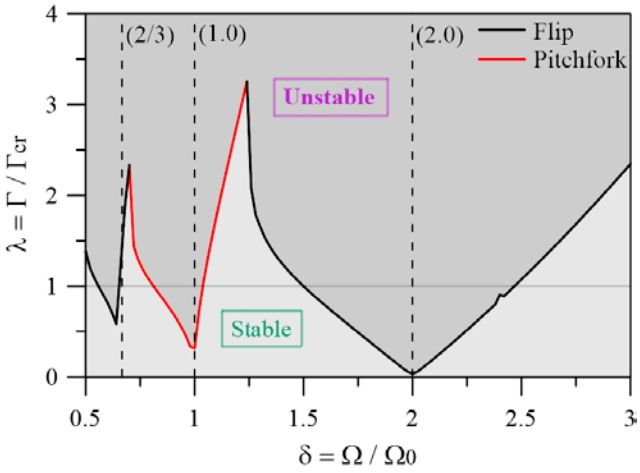

Figure 7.20 - Flip and Pitchfork bifurcations on the parametric stability boundary for the equal-leg angle section profile ($\beta = 1.0$, $\xi = 1/30$, $\varphi = 0.02$). Stability boundary obtained by using numerical integration in conjunction with Floquet theory: dark gray region unstable, light gray region stable.

The natural frequency results of the pure torsional and major-axis flexural-torsional ROMs exhibit significant agreement over a wide range of the plate aspect ratios $\varphi = b/L$ in equal-leg angle section profiles (Figure 5.10b). As previously discussed, this is explained by the dominant influence of torsion in the modal participation of short to intermediate-length equal-leg profiles. However, as φ decreases (for example, $\varphi = 0.02$), the pure torsional ROM leads to higher frequency values, given the increasing contribution of bending. To investigate the effects associated with bending in the nonlinear dynamic response of equal-leg section columns with low values of φ, Figure 7.21 depicts the parametric stability boundaries for both ROMs, pure torsional and major-axis flexural torsional, with $\xi = 1/30$ and $\varphi = 0.02$. It can be observed that, despite differences in linear results for the considered geometric parameters (Ω_0^2 = 11.90e-5 and Ω_0^2 = 11.06e-5 for (ζ_t) and ($\zeta_{Mb}+\zeta_t$) ROMs, respectively), the nondimensional parametric instability boundaries are practically coincident.

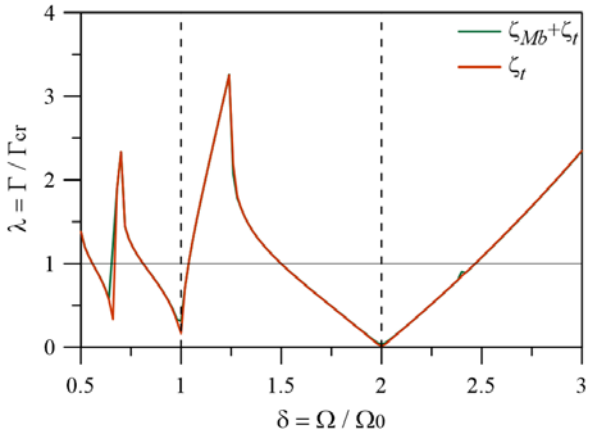

Figure 7.21 - Parametric stability boundaries for an equal-leg angle section profile considering pure torsional and flexural-torsional ROMs (β = 1.0, ξ = 1/30, φ = 0.02).

Figure 7.22 depicts the bifurcation diagrams for torsional amplitudes associated with the principal and fundamental resonance regions in Figure 7.21 (β = 1.0, ξ = 1/30, φ = 0.02), considering both the torsional and flexural-torsional ROMs. For δ = 0.9 and δ = 1.05, both ROMs lead to a pitchfork bifurcation (Figure 7.22a and b). They display a certain symmetry around the trivial solution. As the fixed points of the uncoupled ROM (ζ_t) are also the maximum amplitudes of their orbits, as shown in the phase-planes in Figure 7.23a-b, it can be observed that coupled vibration achieves slightly higher negative torsional amplitudes, while the uncoupled solution reaches greater positive amplitudes. These asymmetries are due to quadratic nonlinearities. The same is noted for δ = 1.8, where a stable flip bifurcation is observed. In contrast, the bifurcation diagram associated with the ascending branch of the right transition curve of the parametric resonance region (δ = 2.2, unstable flip bifurcation), shows a lack of agreement between the pure torsional ROM and the major-axis flexural-torsional ROM, despite the parametric stability curves of both ROMs being practically the same, see Figure 7.22d. First, it is observed that the saddle-node bifurcation of the uncoupled ROM occurs at a much lower value of axial load parameter (λ = 0.04 as opposed to λ = 0.13). This would lead to nontrivial solutions for the uncoupled ROM at very low load magnitudes. In addition, the coupled ($\zeta_{Mb}+\zeta_t$) ROM exhibits rather different branches of non-trivial solutions with two coexisting 2T periodic solutions for $\lambda \geq 0.56$, a phenomenon not observed in the pure torsional case. Additionally, the amplitudes of one of the attractors in the coupled ROM are always greater than the pure torsional amplitudes, as can be confirmed by comparing their respective phase-

planes (Figure 7.15b and e, Figure 7.23c-d). It must be pointed out that the coupled model naturally takes into account the torsional mode. Thus, the results for purely torsional mode are not expected, clarifying the influence of the modal coupling on the results.

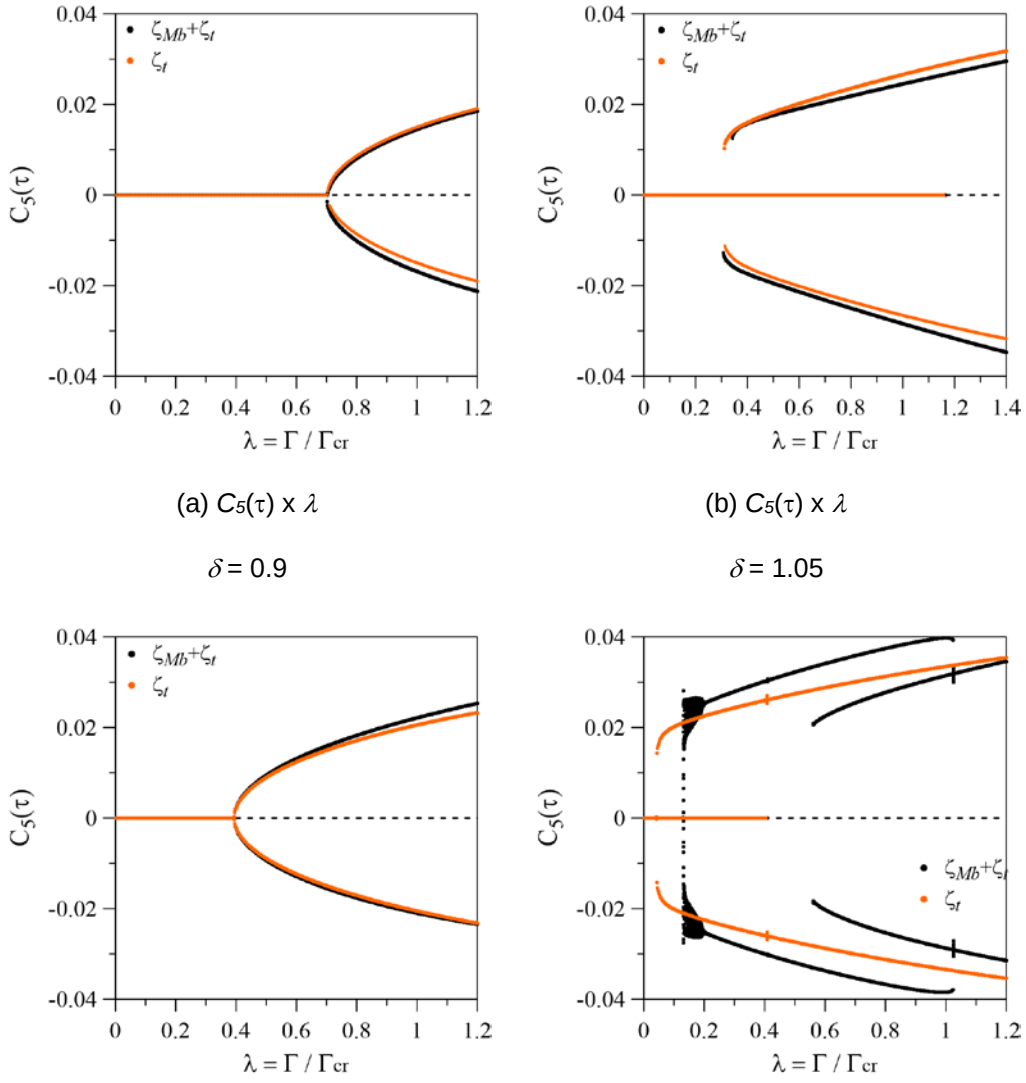

(a) $C_5(\tau)$ x λ

$\delta = 0.9$

(b) $C_5(\tau)$ x λ

$\delta = 1.05$

(c) $C_5(\tau)$ x λ

$\delta = 1.8$

(d) $C_5(\tau)$ x λ

$\delta = 2.2$

Figure 7.22 - Bifurcation diagrams for selected values of frequency ratio, considering pure torsional and flexural-torsional ROMs ($\beta = 1.0$, $\xi = 1/30$, $\varphi = 0.02$).

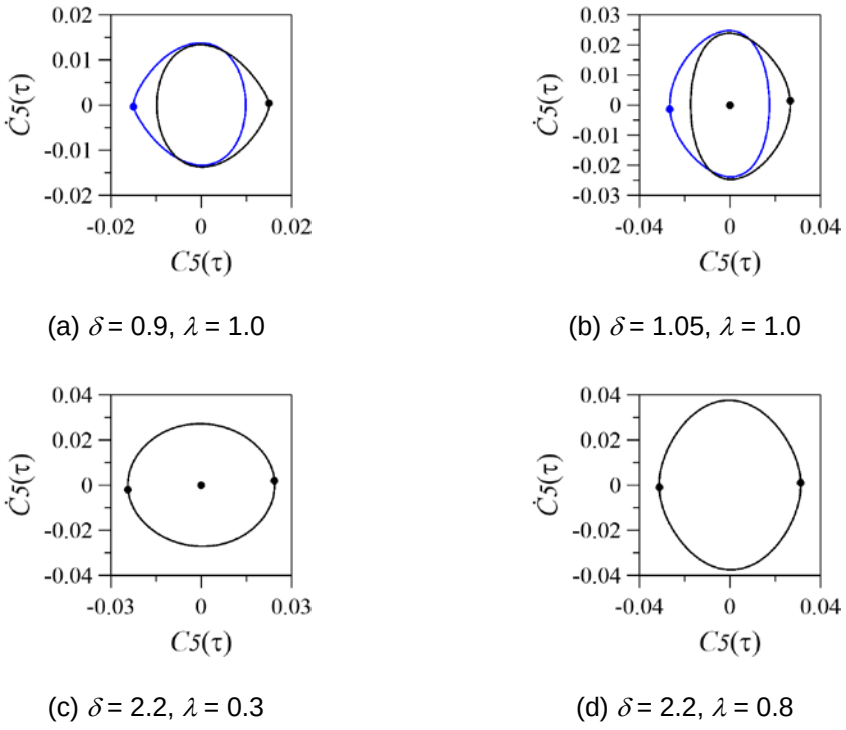

(a) $\delta = 0.9$, $\lambda = 1.0$ (b) $\delta = 1.05$, $\lambda = 1.0$

(c) $\delta = 2.2$, $\lambda = 0.3$ (d) $\delta = 2.2$, $\lambda = 0.8$

Figure 7.23 - Phase-plane projections and fixed points of the Poincaré map for selected values of δ and λ, considering pure torsional ROM (ζ_t).

Figure 7.24 shows the parametric stability boundaries for the equal-leg angle section profile, with $\xi = 1/30$, for selected values of plate aspect ratio, φ. The major-axis flexural-torsional ($\zeta_{Mb}+\zeta_t$) ROM is employed, consistent with the linear results for the considered geometric parameters (Figure 5.10b). One observes that significant differences are only observed in the vicinity of peaks where the dynamic buckling load attains a maximum much higher than the static buckling load. The transition curves are insensitive to the value of φ in the investigated range.

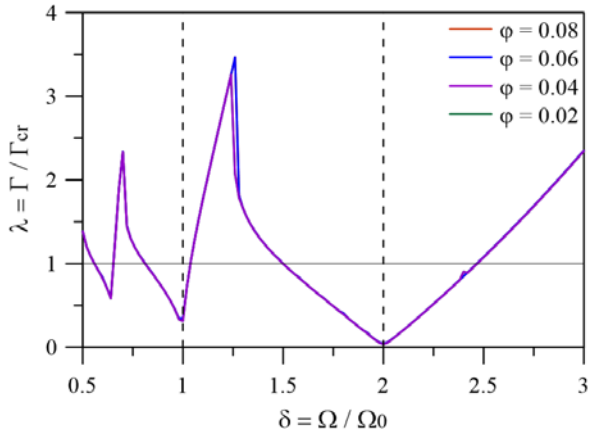

Figure 7.24 - Influence of the wider plate aspect ratio on the parametric stability boundaries for equal-leg angle section profiles ($\beta = 1.0$, $\xi = 1/30$).

Figure 7.25 shows the bifurcation diagrams for bending and torsional vibration amplitudes, considering the frequency ratio $\delta = 2.2$ and two values of wider plate aspect ratio ($\varphi = 0.02, 0.08$). One can observe the significant influence of the wider plate aspect ratio on the bifurcation diagrams of the angle section profiles. The bending vibration amplitudes for $\varphi = 0.08$ are much smaller than the amplitudes for $\varphi = 0.02$. The opposite is observed for torsional amplitudes, which are much greater when $\varphi = 0.08$ (the fixed points of the higher amplitude solution for $\varphi = 0.02$ are endpoints on the orbits, as shown in Figure 7.15b and e). This reinforces the fact that short and intermediate-length profiles are more prone to torsional effects, given their significant contribution to the modal participation of these profiles. It should be noted that for shorter profiles, the increase in torsional stiffness after the critical load is lower, favoring the emergence of higher torsional amplitudes, as shown in the post-critical results (Figure 6.2b). Furthermore, Figure 7.25 shows that there are no coexisting non-trivial solutions for the shorter profile ($\varphi = 0.08$), as is the case for the longer profile, which is more sensitive to bending effects. It is worth highlighting that the saddle-node for the shorter profile occurs at lower values of the axial load parameter, indicating that the trivial solution may lose stability at lower load levels.

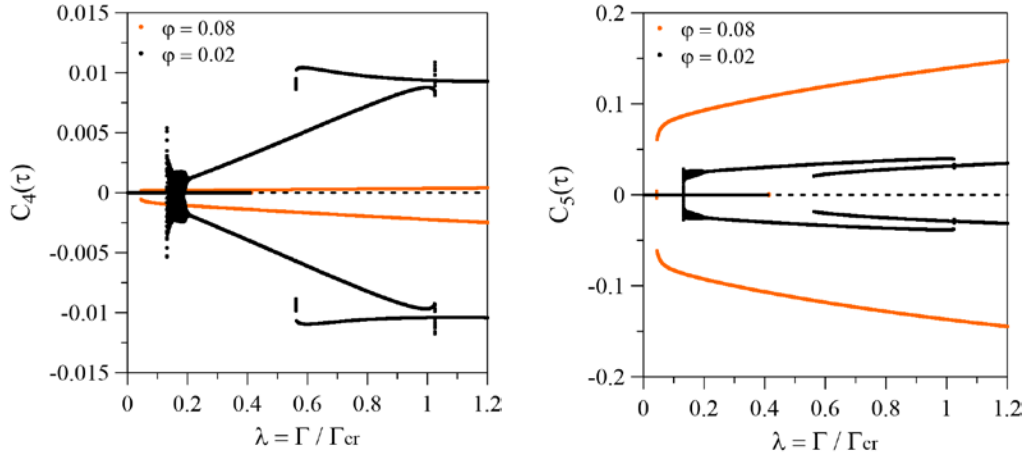

(a) $C_4(\tau)$ x λ (b) $C_5(\tau)$ x λ

Figure 7.25 - Bifurcation diagrams for the frequency ratio $\delta = 2.2$, considering two values of the wider plate aspect ratio ($\varphi = 0.02, 0.08$).

For unequal-leg profiles, the importance of the flexural-torsional ROM with minor-axis bending on the natural frequencies was observed (Figure 5.14b). For small values of φ (such as $\varphi = 0.02$, for example), torsional effects decrease

considerably, and the pure bending ROM (ζ_{mb}) results are quite close to the coupled model ($\zeta_{mb}+\zeta_t$). Figure 7.26 presents the parametric stability boundaries for both ROMs. A good agreement between the two boundaries can be observed, except in the region where the parametric instability loads reach their maximum values, leading to a significant discontinuity in the boundary of the coupled ROM, especially in the range $1.1 < \lambda < 1.3$. Other than that, for high values of the frequency parameter ($\delta > 2.5$), it is observed that the boundary of the coupled ROM stays slightly above the boundary of the uncoupled ROM. The principal and fundamental parametric resonance regions below the static critical load do not undergo significant changes from one model to another.

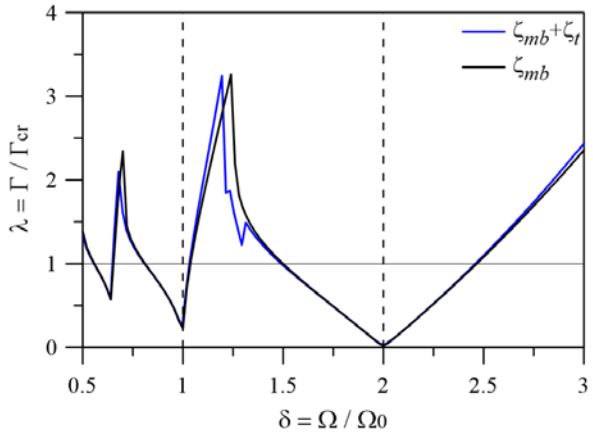

Figure 7.26 - Parametric stability boundaries for the unequal-leg angle section profile considering pure bending and flexural-torsional ROMs ($\beta = 0.5$, $\xi = 1/15$, $\varphi = 0.02$).

As observed in Figure 4.6 and Figure 5.11, there is an abrupt change in modal participation in equal-leg angle section profiles for a certain value of φ. For values of $\varphi > \varphi_t$, where φ_t is the transition aspect ratio, the torsional effects disappear, and the profile behavior is governed solely by the minor axis bending mode. To study the effects of the pure minor axis bending and major-axis flexural-torsional ROMs on nonlinear dynamic instability around the transition value, Figure 7.27 depicts the parametric stability boundaries of the trivial solutions for both ROMs, with $\xi = 1/15$ and $\varphi = 0.032$, in accordance with Figure 5.11b.

It is observed that the parameterized boundaries in Figure 7.27 are quite close, except for a distinct behavior in the region between the principal and fundamental resonance tongues. In this region, the pure bending (ζ_{mb}) ROM leads to higher the dynamic instability loads, while the flexural-torsional ($\zeta_{Mb}+\zeta_t$) ROM exhibits a

discontinuity, resulting in two smaller peaks and a reduction in the dynamic instability load at $\delta = 1.18$. Additionally, the ζ_{mb} stability boundary is slightly above the $\zeta_{Mb}+\zeta_t$ one along the ascending branch of the principal parametric resonance region.

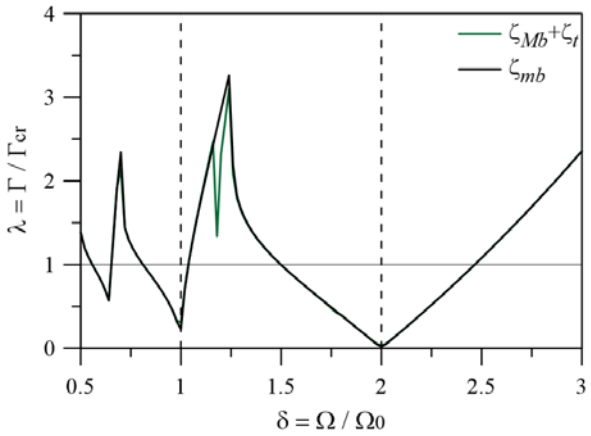

Figure 7.27 - Parametric stability boundaries at the transition value of modal participation, φ_t= 0.0322, considering pure bending and flexural-torsional ROMs ($\beta = 1.0$, $\xi = 1/15$).

Figure 7.28 and Figure 7.30 show the bifurcation diagrams associated with the left and right transition curves of the principal parametric resonance region in Figure 7.27. The two models lead to distinct bifurcation diagrams in both cases. For the ($\zeta_{Mb}+\zeta_t$) ROM, Figure 7.28a shows for $\delta = 1.8$ that after the supercritical bifurcation, the flexural amplitudes reach a maximum at $\lambda = 0.59$, decrease to a minimum at $\lambda = 0.69$, and then continuously increase again. The amplitudes of the (ζ_{mb}) ROM, Figure 7.28b, do not exhibit this behavior but rather a continuous increase after the flip bifurcation point. As expected, the vibration amplitudes of the pure bending ROM are significantly higher, indicative of the behavior of a slender column subjected to bending only and consistent with its low stiffness gain observed in the post-critical path in Figure 6.7 and Figure 6.8. Figure 7.29 depicts the evolution of the period-two orbits corresponding to the stable nontrivial solutions in Figure 7.28.

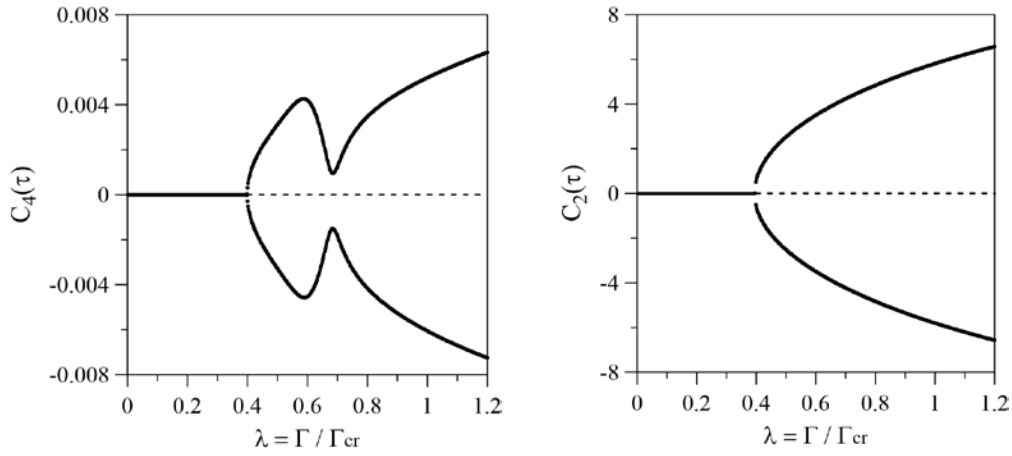

(a) (ζ_{Mb}+ζ_t) ROM (b) (ζ_{mb}) ROM

Figure 7.28 - Bifurcation diagrams for the transition aspect ratio φ_t= 0.0322 for the frequency ratio δ = 1.8, considering the pure bending and flexural-torsional ROMs (β = 1.0, ξ = 1/15).

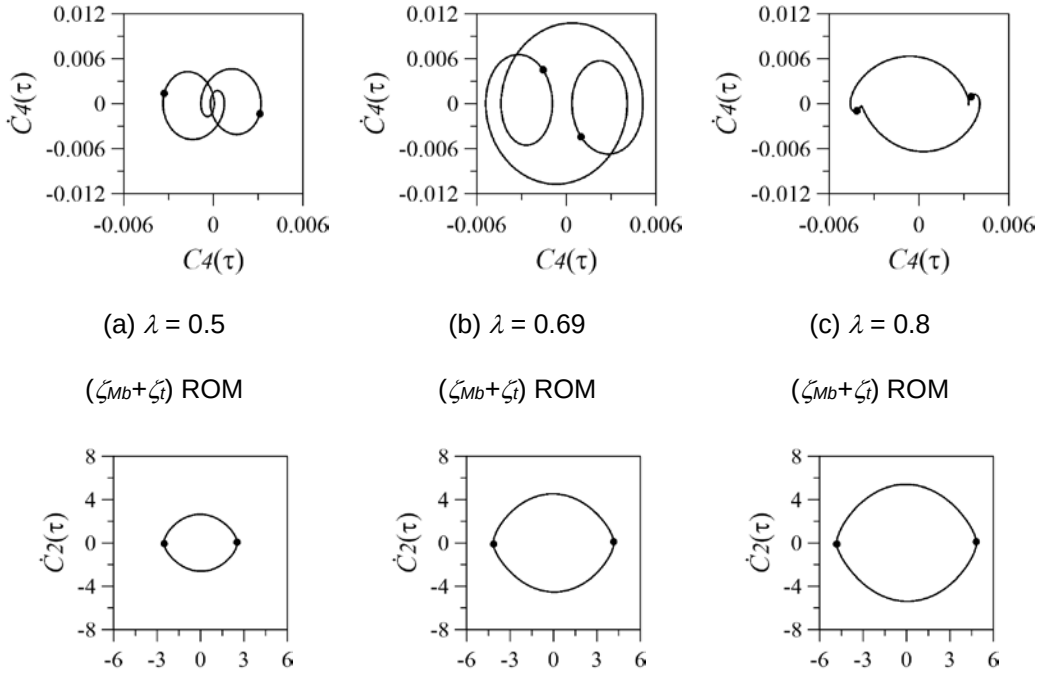

(a) λ = 0.5 (b) λ = 0.69 (c) λ = 0.8

(ζ_{Mb}+ζ_t) ROM (ζ_{Mb}+ζ_t) ROM (ζ_{Mb}+ζ_t) ROM

(a) λ = 0.5 (b) λ = 0.69 (c) λ = 0.8

(ζ_{mb}) ROM (ζ_{mb}) ROM (ζ_{mb}) ROM

Figure 7.29 - Phase-plane projections and fixed points of the Poincaré map for the transition aspect ratio φ_t = 0.0322, considering δ = 1.8 and selected values of λ.

On the right transition curve of the principal parametric resonance region, both the pure bending and major-axis flexural-torsional ROMs exhibit a similar behavior, see Figure 7.30 for δ = 2.2. The flip bifurcation point and the saddle-node

are practically coincident. However, the vibration amplitudes of the uncoupled ROM (ζ_{mb}) continue to be significantly larger than those of the coupled mode. This demonstrates that the angle section profile can display considerable vibration amplitudes, as long as the wider plate aspect ratio exceeds the transition limit value ($\varphi > \varphi_t$), resulting in vibrations governed solely by the pure bending mode.

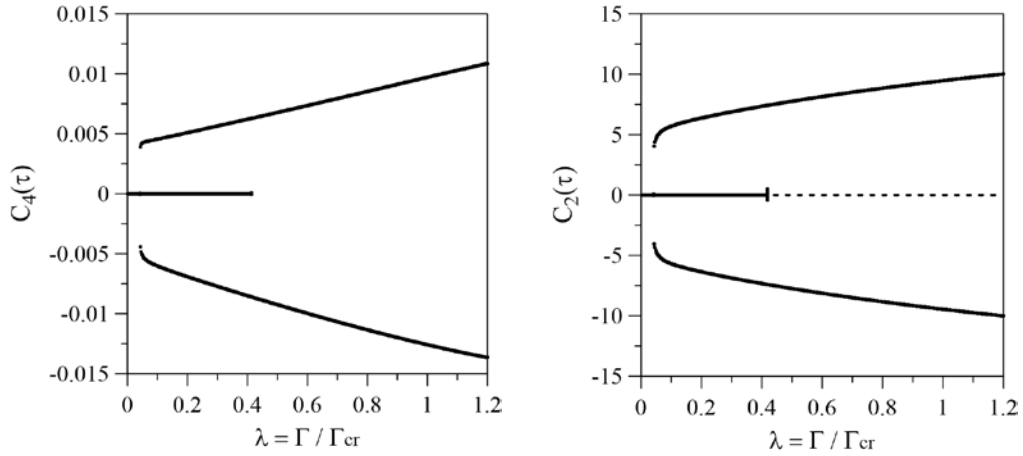

(a) ζ_{Mb}+ζ_t ROM (b) ζ_{mb} ROM

Figure 7.30 - Bifurcation diagrams on the transition wider plate aspect ratio (φ_t = 0.0322) for the frequency ratio δ = 2.2, considering pure bending and flexural-torsional ROMs (β = 1.0, ξ = 1/15).

In Figure 7.31, the influence of the nondimensional material parameter on the parametric stability boundaries of equal-leg angle section profiles is studied, while keeping the geometric parameters constant (ξ = 1/15, φ = 0.04). The material parameters considered are the same as those in Figure 5.18. It is observed that the boundaries are very close. Only for the material with intermediate parameter ψ = 0.1775, a distinct behavior is observed in the region between the principal and secondary parametric resonance valleys. However, the variation in the material parameter does not cause important effects on the transition curves of the principal and fundamental parametric resonance regions, although the natural frequencies for each case are quite different, as shown in Table 7.1, for comparison purposes. Furthermore, for the isotropic material profile (ψ = 0.3850), since its stability is governed by the minor-axis bending mode for the considered geometric parameters, its vibration amplitudes will be significantly higher compared to the other materials.

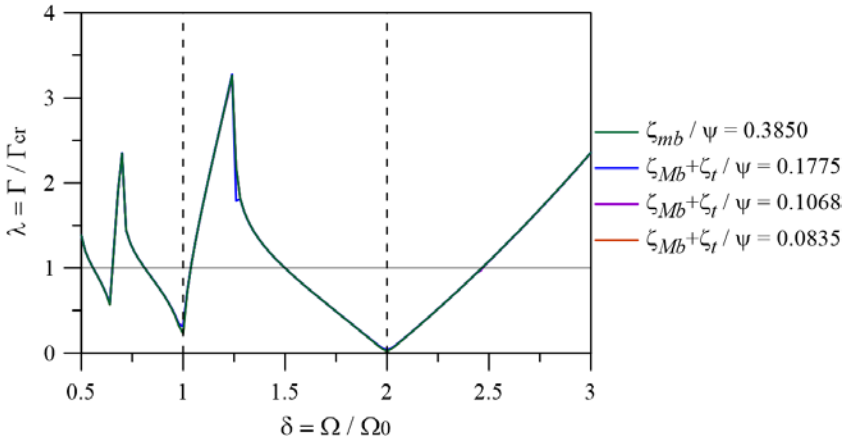

Figure 7.31 - Influence of the material parameter on the parametric stability boundaries for the equal-leg angle section profile ($\beta = 1.0$, $\xi = 1/15$, $\varphi = 0.05$).

Table 7.1 - Fundamental frequency parameters for selected values of ψ ($\beta = 1.0$, $\xi = 1/15$, $\varphi = 0.04$).

ψ	ROM	Ω_0^2 (x10-5)
0.0835	$\zeta_{Mb}+\zeta_t$	35.54
0.1068	$\zeta_{Mb}+\zeta_t$	44.54
0.1775	$\zeta_{Mb}+\zeta_t$	69.82
0.3850	ζ_{mb}	65.87

There is a lack of information on the damping characteristics of FRP profiles. The influence of damping on the parametric stability boundaries is now analyzed. Figure 7.32 shows the parametric stability boundaries for selected values of the linear viscous damping, Ξ, within a range of values compatible with the pultruded material (Boscato & Russo, 2009). An equal-leg angle section profile is considered ($\beta = 1.0$), with $\xi = 1/15$ and $\varphi = 0.04$. The impact of damping is evident in rising the transition curves, consequently increasing the parametric instability loads and marginally reducing the width of the instability regions. The effect is particularly pronounced in the valley bottoms, around the points where $\delta = 2/n$ ($n = 1, 2, 3...$), as can be more clearly seen in the zoom charts 1, 2 and 3 in Figure 7.33. Beyond these points, the effect of damping practically vanishes.

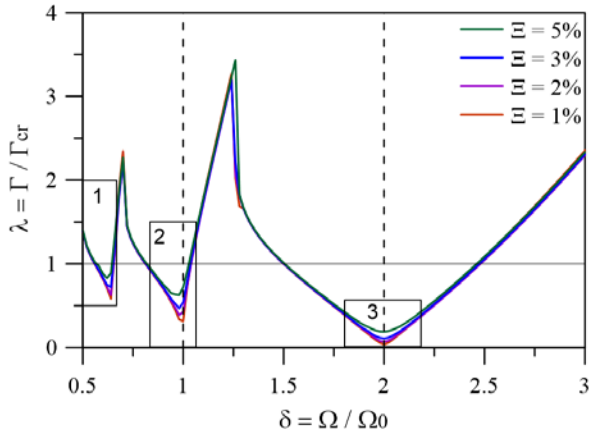

Figure 7.32 - Influence of the linear viscous damping parameter on the parametric stability boundaries of the equal-leg angle section profiles (β = 1.0, ξ = 1/15, φ = 0.04).

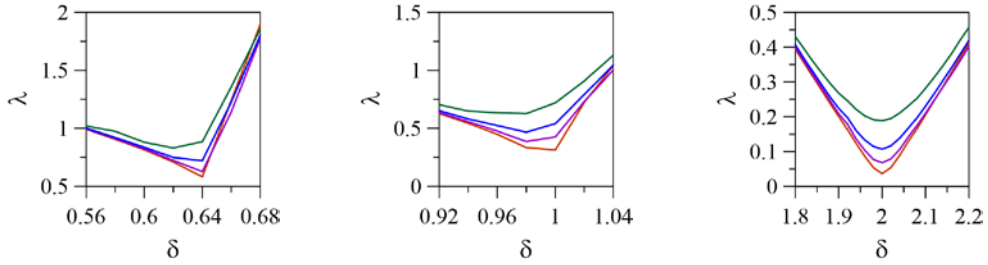

(a) Zoom chart 1 (b) Zoom chart 2 (c) Zoom chart 3

Figure 7.33 - Zoom charts on the parametric stability boundaries with varying viscous damping parameter.

The parametric instability loads are observed to be much lower than the critical static load (λ = 1) in the main resonance regions, around the points $\delta = 2/n$ (n = 1, 2, 3...), even when considering high damping values (Ξ = 5%). This is clearly shown in Table 7.2, which presents the minimum parametric instability loads for the selected damping parameters in the first three instability regions (δ = 2/3, 1, 2). In the parameterized form, the following functional relations can be established between the lowest parametric instability load and the damping parameter: $\lambda = 1.6187\Xi^{0.2297}$, for $\delta \cong 2/3$, $\lambda = 2.8589\Xi^{0.5096}$, for $\delta \cong 1$, and $\lambda = 6.4588\Xi^{1.1687}$, for $\delta \cong 2$. These power functions clarify that very large and uncommon damping values would be necessary to reach the static critical load in these resonance regions.

Table 7.2 - Variation of the minimum parametric instability load as a function of the damping parameter in the first three regions of parametric instability.

Ξ	$\delta \cong 2/3$	$\delta \cong 1$	$\delta \cong 2$
1%	0.57734	0.27578	0.02891
2%	0.62891	0.38828	0.06953
3%	0.72266	0.46953	0.10859
5%	0.83047	0.63047	0.18984

Figure 7.34 shows the bifurcation diagrams for bending and torsional vibration amplitudes, considering the frequency ratio $\delta = 2$ and two values of damping parameter (Ξ = 1%, 5%). As expected, it is observed that the supercritical flip bifurcation occurs for higher axial load parameters when the damping increases. This shows that the damping effect is beneficial for the structure, postponing the onset of nontrivial solutions.

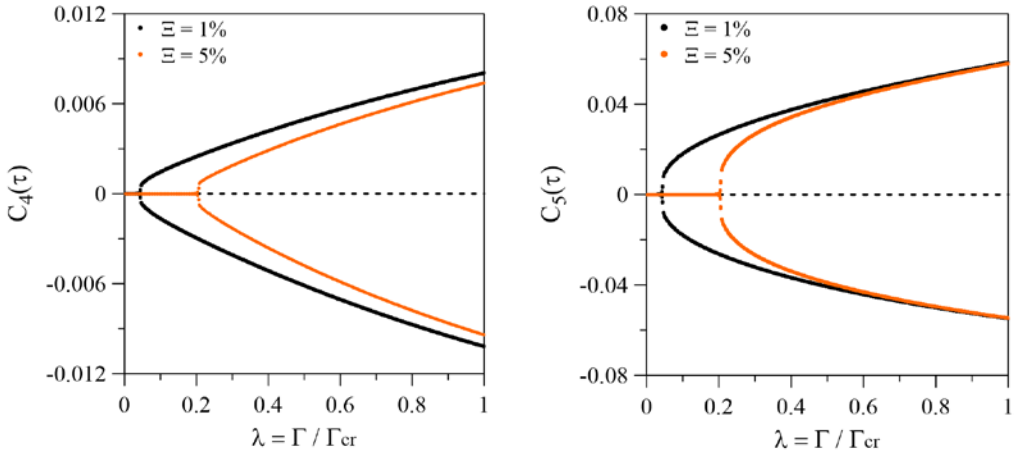

(a) $C_4(\tau)$ x λ (b) $C_5(\tau)$ x λ

Figure 7.34 - Bifurcation diagrams for the frequency ratio $\delta = 2$ and selected values of damping parameter ($\beta = 1.0$, $\xi = 1/15$, $\varphi = 0.04$).

8
Conclusions and Future Directions

8.1
Conclusions

The present study undertook a comprehensive investigation of the buckling and vibration of angle section FRP pultruded profiles, encompassing both equal and unequal-leg sections, and spanning from short to long columns. The angle section column was modeled as two individual orthotropic plates subjected to uniform axial in-plane loads. The plates were considered simply-supported at the loaded edges, with continuity conditions enforced along the common edge and the opposite edge left free. The simply supported columns were permitted to rotate about their principal axes. It is well-known that the critical buckling mode and fundamental vibration mode of angle sections are highly dependent upon geometric and material parameters, with flexural-torsional coupling being a common occurrence. In addressing this crucial aspect, reduced order models (ROMs) were initially derived based on the modal participation variation with the geometric and material parameters, identified through the utilization of GBTuL software. To achieve this, shape functions for in-plane and transversal plate displacements were analytically derived, encompassing major and minor axis bending as well as torsion. The examination of both uncoupled and coupled problems was conducted by employing the Ritz method and the von Kármán nonlinear plate theory. Hamilton's principle was applied to derive the nonlinear equations of motion. The linear solution thereof provided critical loads, natural frequencies, respective modes, and load-frequency relations, which were validated by favorably comparing them with the GBTuL results, employed here as a benchmark. Dimensionless geometric and physical parameters were introduced to generalize the conclusions. Three independent geometric parameters can effectively describe the column's geometry: the ratio of

shorter to longer leg width, the plate aspect ratio of the longer leg, and a slenderness parameter given by the thickness to the shorter leg width.

The influence of the aspect ratio for the leg widths plays a crucial role in distinguishing the behavior of equal and unequal-leg profiles. As this ratio increases from zero (representing a single plate) to 1.0 (indicating equal-leg profiles), the participation of the torsional mode steadily increases, approaching unity for short-to-intermediate length profiles, while the involvement of the minor axis bending mode diminishes to zero. Parallel, the participation of the major axis bending mode, although minimal, exhibits a gradual increase, potentially exerting a slight influence on long profiles. Consequently, the modal participation is markedly contingent on the aspect ratio of the angle section legs. Observations indicate that the flexural-torsional ROM, incorporating minor-axis bending, results in a lower bound of the results, whereas the flexural-torsional model considering major axis bending (in alignment with the torsional model) results in an upper bound. As the ratio increases, the results transition from the lower to the upper bound. This phenomenon has been consistently verified across a broad spectrum of nondimensional parameters.

In the case of equal-leg sections, it has been observed that for very slender sections - where the thickness to leg width ratio is small - the coupled flexural-torsional mode, considering major axis bending, yields outcomes akin to those obtained through GBTul. With major axis bending mode contributing minimally, results from pure torsion analysis are close to those provided by the coupled ROM for short-to-intermediate columns. However, as this ratio increases (either due to increased thickness or decrease of leg width), a sudden and discontinuous change in modal participation becomes apparent at a specific transition length, contingent upon material and geometric parameters. Prior to this transition length, the interplay between torsion and major axis bending governs the response. In longer profiles, however, minor axis bending assumes full responsibility for the linear behavior. Despite the abrupt and discontinuous variation in modal participation, the critical load and fundamental frequency exhibit smooth changes around the transition point. Additionally, as the leg width increases while other parameters remain constant, linear results increases until reaching a peak, where the curve slope abruptly shifts, leading to a subsequent decrease in outcomes. Consequently, for a given set of

parameters, an optimal leg width exists where the critical load and natural frequency reach their maximum. Before reaching the optimal width, the ROM considering only minor axis bending yields excellent results. Conversely, beyond the optimal width, the coupled flexural-torsional mode, considering major axis bending, governs the response. In unequal-leg profiles, a coupling between minor axis flexural and torsional modes is evident, where the influence of the torsional mode decreases while that of the minor axis flexural mode increases with the column's slenderness.

The material parameter also affects the transition point where the abrupt change in modal participation takes place. For the same section geometry, pultruded profiles have lower critical loads and natural frequencies, as well as a modal transition between the flexural-torsional and pure bending modes for longer profile lengths, compared to isotropic profiles, which are prone to pure minor axis bending at shorter lengths. The strong influence of nondimensional parameters for the pultruded orthotropic material on the outcomes, alongside its comparison with certain isotropic materials, underscores the importance of a precise FRP material characterization for ensuring reliable stability and vibration analyses. This highlights the necessity for continued research into FRP pultrude structural elements and other composite materials.

After being favorably compared with the GBTul results, the ROMs were used to explore the nonlinear post-buckling behavior and imperfection sensitivity of slender equal-leg and unequal-leg FRP angle section columns. The nonlinear equilibrium paths of the perfect and imperfect columns were obtained by the Newton-Raphson method.

The post-buckling response of equal-leg profiles is strongly influenced by modal participation. Columns of short-to-intermediate lengths demonstrate a significant reserve of post-buckling strength, akin to that of a plate. With major-axis bending contributing minimally, the post-buckling behavior obtained from the pure torsional ROM exhibits remarkable consistency. However, as the influence of the torsional mode decreases, the post-buckling strength decreases, making the column more prone to bending-induced deflections, which become increasingly pronounced. Beyond the modal participation transition point, the post-buckling path of equal-leg profiles becomes nearly flat, leading to large deflections similar to the

almost neutral path of the Euler column. Similar to the equal-leg profiles, a decrease in the post-buckling strength reserve is observed for unequal-leg profiles as the influence of torsion decreases. As the minor axis flexural mode becomes dominant, significant amplification of the column deflections are observed. It is important to state that the nonlinear models provide qualitatively correct results; however, additional modes due to quadratic and cubic nonlinearities must be included in the displacement fields to obtain quantitatively comparable results with experiments.

In all cases, a symmetric and stable pitchfork bifurcation is observed, with the nonlinear response of imperfect angles converging asymptotically to the perfect response at large modal amplitudes. However, imperfections in the form of torsional modes have a more significant influence on the nonlinear response, occasionally resulting in an increase in the strength reserve compared to the perfect case.

Profiles made of a stiffer material in the longitudinal direction demonstrate greater post-buckling strength reserve. Pultruded profiles with identical geometric parameters exhibit lower critical loads but higher post-buckling stiffness compared to isotropic profiles. This is because isotropic profiles have higher values of G_{12}/E_1 and are prone to minor-axis bending across a broader range of plate aspect ratios.

The time response of the dynamic system was computed using the fourth-order Runge-Kutta method. The parametric instability boundaries of the harmonically forced column in the forcing control space, along with their associated bifurcation diagrams, are determined by brute force and by continuation methods. The influence of material, damping, and cross-sectional geometry was examined, along with the identification of the types of bifurcation associated with different regions of the parametric instability boundaries. The frequency-amplitude relations demonstrate a hardening behavior, typical of structures such as columns and plates.

In the principal parametric resonance region, transitions from the trivial equilibrium to periodic solutions occur due to a flip bifurcation (2:1 resonance), whereas in the fundamental resonance region, the shift from trivial to non-trivial solutions arises from a pitchfork bifurcation (1:1 resonance), resulting in two competing attractors. As a result of the hardening-type nonlinearity, the left-hand side of each tongue represents the locus of stable bifurcations (supercritical), while the right-hand side denotes the locus of unstable bifurcations (subcritical). The

dynamic buckling load in the principal parametric and fundamental resonance regions is much lower than the static buckling load.

In equal-leg profiles, the wider plate aspect ratio has minimal influence on the parametric instability boundaries, unlike in bifurcation diagrams where lower aspect ratios correspond to higher torsional vibration amplitudes. This observation agrees with the increased contribution of torsion in modal participation as the column length becomes shorter. The pure torsional ROM offers a reasonable approximation for bifurcation diagrams, even for small wider plate aspect ratio values. In the modal transition point, the minor-axis bending model exhibits significant vibration amplitudes, contrasting with the coupled flexural-torsional model with major-axis bending, consistent with post-critical path results. Moreover, the material parameter demonstrates insignificant effects on the parametric instability boundaries, unlike variations in the damping ratio, where the tongues of each resonance region yield higher results for more damped systems.

The proposed reduced-order models (ROM) combined with plate theory has proven to be an efficient analysis tool, reducing computational complexity while maintaining the necessary fidelity to the expected response. These time-efficient and accurate analyses are well-suited for structural design processes, enabling straightforward assessment of the impact of geometric and physical parameters on linear and nonlinear results.

8.2
Suggestions for future work

Due to the complexity of the problem and the scarcity of nonlinear solutions available in the literature, the following topics are suggested for future work:

- Nonlinear stability analysis of angle profiles under different boundary conditions. In particular, columns with clamped boundaries and clamped-free columns fixed and free can provide, respectively, an upper and lower limit for buckling loads and natural frequencies. Additionally, the participation and transition of different deformation modes depend on the support conditions;

- Investigation of the linear and nonlinear behavior of angle section profiles made of other types of composites such as laminated and functionally graded materials;
- Experimental analysis of the dynamic instability of pultruded FRP columns. No experimental results were found in the literature on the parametric instability of these structures.

Bibliographic References

ÁDÁNY, S.; DÁVID, V. Global buckling of thin-walled simply supported columns: numerical studies. **Thin-Walled Structures**, v. 54, p. 82-93, 2012.

ALAM, M. I.; KANAGARAJAN, B.; JANA, P. Optimal design of thin-walled open cross-section column for maximum buckling load. **Thin-Walled Structures**, v. 141, p. 423-434, 2019.

ALLEN, H. G.; BULSON, P. S. **Background to Buckling**. McGraw Hill, London, 1980.

AMBROSINI, R. D.; RIERA, J. D.; DANESI, R. F. A modified Vlasov theory for dynamic analysis of thin-walled and variable open section beams. **Engineering Structures**, v. 22, n. 8, p. 890-900, 2000.

ANSYS, Inc. **ANSYS Fluent User's Guide**, 2024 R1 Release, 2024.

ASCIONE, F. et al. A closed-form equation for the local buckling moment of pultruded FRP I-beams in major-axis bending. **Composites Part B**, v. 97, p. 292-299, 2016.

ATTARD, M. M. Nonlinear theory of non-uniform torsion of thin-walled open beams. **Thin-walled Structures**, v. 4, n. 2, p. 101-134, 1986.

BAI, L.; YANG, J.; WADEE, M. A. Cellular buckling from nonlinear mode interaction in unequal-leg angle struts. **Thin-Walled Structures**, v. 132, p. 316-331, 2018.

BALAGOPAL, R.; PRASAD RAO, N.; ROKADE, R. P. Investigation on buckling behaviour of GFRP angle sections with bolted connections in lattice towers. **Journal of The Institution of Engineers (India): Series A**, v. 101, n. 2, p. 327-342, 2020.

BANAT, D.; KOLAKOWSKI, Z.; MANIA, R. J. Investigations of FML profile buckling and post-buckling behaviour under axial compression. **Thin-Walled Structure,** v. 107, p. 335-344, 2016.

BARBERO, E. J.; TROVILLION, J. Prediction and measurement of the post-buckling behavior of fiber-reinforced composite columns. **Composites Science and Technology**, v. 58, n. 8, p. 1335-1341, 1998.

BEBIANO, R.; CAMOTIM, D.; GONÇALVES, R. GBTul 2.0 - A second-generation code for the GBT-based buckling and vibration analysis of thin-walled members. **Thin-Walled Structures**, v. 124, p. 235–257, 2018.

BEBIANO, R. et al. GBTUL - buckling and vibration analysis of thin-walled members, DECivil/IST, Technical University of Lisbon, Lisbon (http://www.civil.ist.utl.pt/gbt), 2008a.

BEBIANO, R.; SILVESTRE, N.; CAMOTIM, D. Local and global vibration of thin-walled members subjected to compression and non-uniform bending. **Journal of sound and vibration**, v. 315, n. 3, p. 509-535, 2008b.

BEBIANO, R.; SILVESTRE, N.; CAMOTIM, D. GBTUL - a Code for the Buckling Analysis of Coldformed Steel Members. **International Specialty Conference on Cold-Formed Steel Structures**, 2008c.

BEBIANO, R.; GONÇALVES, R.; CAMOTIM, D. A cross-section analysis procedure to rationalise and automate the performance of GBT-based structural analyses. **Thin-Walled Structures**, v. 92, p. 29-47, 2015.

BEHZADI-SOFIANI, B.; GARDNER, L.; WADEE, M. A. Stability and design of fixed-ended stainless steel equal-leg angle section columns. **Engineering Structures**, v. 249, p. 113281, 2021.

BEHZADI-SOFIANI, B.; GARDNER, L.; WADEE, M. A. Testing, numerical analysis and design of stainless steel equal-leg angle section beams. **Structures**, v. 37, p. 977-1001, 2022.

BEHZADI-SOFIANI, B.; WADEE, M. A.; GARDNER, L. Major-axis buckling of pin-ended stainless steel equal- leg angle section members: FE modelling and design. **Ce/Papers**, v. 6, n. 3-4, p. 2625-2630, 2023.

BOLOTIN, V. V. **The dynamic stability of elastic systems**, 1964.

BOSCATO, G.; RUSSO, S. Free vibrations of pultruded FRP elements: Mechanical characterization, analysis, and applications. **Journal of Composites for Construction**, v. 13, n. 6, p. 565-574, 2009.

BRUSH, D. O.; ALMROTH, B. O. **Buckling of Bars, Plates, and Shells**. McGraw-Hill, New York, 1975.

CALLISTER, W. D.; RETHWISCH, D. G. **Materials Science and Engineering: an introduction**. 9. ed. John Wiley & Sons, 2013. 992 p.

CARDOSO, D. C. T.; HARRIES, K. A.; BATISTA, E. M. Closed-form equations for compressive local buckling of pultruded thin-walled sections. **Thin-Walled Structures**, v. 79, p. 16-22, 2014.

CARDOSO, D. C. et al. Explicit equations for distortional buckling of cold-formed steel lipped channel columns. **Thin-walled structures**, v. 119, n. 925-933, 2017.

CARDOSO, D. C. T.; TOGASHI, B. S. Experimental investigation on the flexural-torsional buckling behavior of pultruded GFRP angle columns. **Thin-Walled Structures**, v. 125, p. 269-280, 2018.

CARVALHO, E. C. Vibrações Não Lineares e Não Planares e Instabilidade Dinâmica de Barras Esbeltas. 2013. 228 f. Tese (Doutorado em Engenharia Civil) - Departamento de Engenharia Civil, Pontifícia Universidade Católica do Rio de Janeiro, Rio de Janeiro, 2013.

CARVALHO, E. C.; GONÇALVES, P. B.; REGA, G. Multiple Internal Resonances and Nonplanar Dynamics of a Cruciform Beam with Low Torsional Stiffness. **International Journal of Solids and Structures**, v. 121, p. 117-134, 2017.

CEN/TS 19101. **Design of Fibre-Polymer Composite Structures**. European Committee for Standardization (CEN), 2022.

CHIA, C. Y. **Nonlinear Analysis of Plates**. McGraw-Hill, New York, 1980.

CINTRA, G. G.; CARDOSO, D. C. T.; VIEIRA, J. D. Parameters affecting local buckling response of pultruded GFRP I-columns: Experimental and numerical investigation. **Composite Structures**, v. 222, p. 110897, 2019.

CLARKE, J. L. **Structural Design of Polymer Composites**: Eurocomp Design Code and Background Document. CRC Press, Boca Raton, 2014.

CNR (National Research Council). **Guide for the design and construction of structures made of FRP pultruded elements**. CNR DT 205/2007. Rome: CNR, 2008.

COAQUIRA, J. C. Oscilações Não Lineares e Instabilidade Dinâmica de Vigas de Seção Aberta e Paredes Delgadas. 2016. 134 f. Dissertação (Mestrado em Engenharia Civil) - Departamento de Engenharia Civil, Pontifícia Universidade Católica do Rio de Janeiro, Rio de Janeiro, 2016.

COAQUIRA, J. C.; GONÇALVES; P. B.; CARVALHO, E. C. Dynamic instability of cantilever beams with open cross-section. In: ASME 2016 **International Mechanical Engineering Congress and Exposition**. American Society of Mechanical Engineers Digital Collection, 2016.

COAQUIRA, J. C. Análise Não Linear da Instabilidade e Vibração de uma Coluna Pultrudada Reforçada com Fibras. 2020. 242 f. Tese (Doutorado em Engenharia Civil) - Departamento de Engenharia Civil, Pontifícia Universidade Católica do Rio de Janeiro, Rio de Janeiro, 2020.

COAQUIRA, J. C. **Nonlinear instability and vibration analysis of a pultruded fiber reinforced column under axial load**. 2020. 242 p. Doctoral thesis - Pontifical Catholic University of Rio de Janeiro, Rio de Janeiro, Brazil, 2020.

COAQUIRA, J. C. et al. Parametric instability and nonlinear oscillations of an FRP channel section column under axial load. **Nonlinear Dynamics**, v. 103, p. 3557-3580, 2021.

COAQUIRA, J. C. et al. Parametric Instability and Bifurcation of Thin-Walled Axially Compressed Long FRP Columns. **Nodycon Conference Proceedings Series**, p. 637-647, 2022.

CORREIA, J. R.; BAI, Y.; KELLER, T. A review of the fire behaviour of pultruded GFRP structural profiles for civil engineering applications. **Composite Structures**, v. 127, p. 267-287, 2015.

D'AGUIAR, S. C. M.; PARENTE JUNIOR, E. Local buckling and post-critical behavior of thin-walled composite channel section columns. **Latin American Journal of Solids and Structures**, v. 15, n. 7, e56, 2018.

DE CASTRO, C. H.; ORLANDO, D.; GONÇALVES, P. B. Static and dynamic nonlinear behavior of a multistable structural system consisting of two coupled von Mises trusses. **International Journal of Non-Linear Mechanics**, v. 156, p. 104510, 2023.

DEL PRADO, Z. J. G. N. **Acoplamento e interação modal na instabilidade dinâmica de cascas cilíndricas**. 2001. 119 f. Tese (Doutorado em Engenharia Civil) - Departamento de Engenharia Civil, Pontifícia Universidade Católica do Rio de Janeiro, Rio de Janeiro, 2001.

DINIS, P. B.; CAMOTIM, D.; SILVESTRE, N. (Eds.) Post-Buckling Behaviour and Strength of Angle Columns: SDSS'Rio 2010 Stability and Ductility of Steel Structures, 2010.

DINIS, P. B.; CAMOTIM, D.; SILVESTRE, N. On the mechanics of thin-walled angle column instability. **Thin-Walled Structure**, v. 52, p. 80-89, 2012.

DINIS, P. B.; CAMOTIM, D. A novel DSM-based approach for the rational design of fixedended and pin-ended short-to-intermediate thin-walled angle columns. **Thin-Walled Structures**, v. 87, p. 158-182, 2015.

DINIZ, A. C.; MALITE, M.; CARDOSO, D. C. Direct Strength Method-Based Approach for Strength Prediction of Pultruded GFRP Angle Columns. **Journal of Composites for Construction**, v. 27, n. 3, p. 04023019, 2023.

DUBINA, D.; UNGUREANU, V. Local/distortional and overall interactive buckling of thinwalled cold-formed steel columns with open cross-section. **Thin-Walled Structures**, v. 182, p. 110172, 2023.

FANG, S. et al. Multistability phenomenon in signal processing, energy harvesting, composite structures, and metamaterials: A review. **Mechanical Systems and Signal Processing**, v. 166, p. 108419, 2022.

FLOQUET, G. Sur les équations différentielles linéaires à coefficients périodiques (PDF), **Annales Scientifiques de l'École Normale Supérieure**, v. 12, p. 47-88.

GARDNER, L. Stability and design of stainless steel structures - review and outlook. **Thin-Walled Structures**, v. 141, p. 208-216, 2019.

GASPAR, C. M. R.; CARDOSO, D. C. T. Investigation of Global and Local Free Vibration of Slender FRP Beams. **Journal of Composites for Construction**, v. 27, n. 3, p. 04023025, 2023.

GIONCU, V. General theory of coupled instabilities. **Thin-Walled Structures**, v. 19, n. 2-4, p. 81-127, 1994.

GONÇALVES, R. et al. Latest developments on the analysis of thin-walled structures using Generalised Beam Theory (GBT). **Journal of Constructional Steel Research**, v. 204, p. 107858, 2023.

GONÇALVES, R.; RITTO-CORRÊA, M.; CAMOTIM, D. A new approach to the calculation of cross-section deformation modes in the framework of generalized beam theory. **Computational Mechanics**, v. 46, p. 759-781, 2010.

HADANE, A. et al. CFD wind tunnel investigation for wind loading on angle members in lattice tower structures. **Journal of Wind Engineering and Industrial Aerodynamics**, v. 236, p. 105397, 2023.

HANCOCK, G. J. Coupled Instabilities in Metal Structures (CIMS) - What have we learned and where are we going?. **Thin-Walled Structures**, v. 128, n. 2-11, 2018.

HASAN, S. A.; BARR, A. D. S. Linear vibration of thin-walled beams of equal angle section. **Journal of Sound and Vibration**, v. 32, n. 1, p. 3-23, 1974.

HE, Z. et al. Design recommendation of cold formed steel built-up sections under concentric and eccentric compression. **Journal of Constructional Steel Research**, v. 212, p. 108255, 2024.

HOLLAWAY, L. C.; CHRYSSANTHOPOULOS, M. K.; MOY, S. S. (Eds.). Advanced polymer composites for structural applications in construction: ACIC 2004. Woodhead publishing, 2004.

HSU, C. S. Cell-to-cell mapping: a method of global analysis for nonlinear systems (v. 64). Springer Science & Business Media, 2013.

HU, N.; BURGUEÑO, R. Buckling-induced smart applications: recent advances and trends. **Smart Materials and Structures**, v. 24, p. 063001, 2015.

JONES, R. M. **Mechanics of Composite Materials**. 2. ed. CRC Press, 1998. 538 p.

KAR, K. K. (Ed.). Composite materials: processing, applications, characterizations. Springer, 2016.

KOVACIC, I.; RAND, R.; MOHAMED SAH, S. Mathieu's equation and its generalizations: overview of stability charts and their features. **Applied Mechanics Reviews**, v. 70, n. 2, p. 020802, 2018.

KRISHNAN, A.; SINGH, V. K. Some studies on vibration of thin-walled open sections. **Journal of sound and vibration**, v. 149, n. 2, p. 297-310, 1991.

KUBIAK, T. Estimation of dynamic buckling for composite columns with open cross-section. **Computers & Structures**, v. 89, n. 21, p. 2001-2009, 2011.

LANDESMANN, A. et al. Short-to-intermediate slender pin-ended cold-formed steel equal-leg angle columns: experimental investigation, numerical simulations and DSM design. **Engineering Structure**, v. 132, p. 471-493, 2017.

LARACUENTE, M. E.; SIPPEL, E. J.; BLUM, H. B. Experimental investigation of fixed-ended hot-rolled austenitic stainless-steel unequal-leg angles under compression. **Structures**, v. 59, p. 105585, 2024.

LEISSA, A. W. The historical bases of the Rayleigh and Ritz methods. **Journal of Sound and Vibration**, v. 287, n. 4-5, p. 961-978, 2005.

LENCI, S.; REGA, G.; RUZZICONI, L. The dynamical integrity concept for interpreting/predicting experimental behaviour: from macro-to nano-mechanics. **Philosophical Transactions of the Royal Society A**: Mathematical, Physical and Engineering Sciences, v. 371, n. 1993, p. 20120423, 2013.

LEVIEN, R. The **elastica: a mathematical history**. Tech. Rep. UCB/EECS-2008-103, University of California, Berkeley, 2008.

LIANG, K.; YANG, C.; SUN, Q. A smeared stiffener based reduced-order modelling method for buckling analysis of isogrid-stiffened cylinder. **Applied Mathematical Modelling**, v. 77, p. 756-772, 2020.

LIU, Y.; CHANTEL, S. Experimental study of steel single unequal-leg angles under eccentric compression. **Journal of Constructional Steel Research**, v. 67, n. 6, p. 919-928, 2011.

LOPES, B. L. S. **Polímeros Reforçados por Fibras Vegetais**: um resumo sobre esses compósitos. São Paulo: Blucher, 2017. 44 p.

MACHADO, S. P.; FILIPICH, C. P.; CORTÍNEZ, V. H.: Parametric vibration of thin-walled composite beams with shear deformation. **Journal of Sound and Vibration**, v. 305, n. 4-5, p. 563-581, 2007.

MAGISANO, D.; GARCEA, G. Increasing the buckling capacity with modal geometric “imperfections” designed by a reduced order model. **Thin-Walled Structures**, v. 178, p. 109529, 2022.

MAILYBAEV, A. A. Brief Introduction to the Theory of Parametric Resonance. In **Lectures on Nonlinear Dynamics**, p. 1-25. Cham: Springer Nature Switzerland, 2023.

MAJI, A. K.; ACREE, R.; SATPATHI, D.; DONNELLY, K. Evaluation of pultruded FRP composites for structural applications. **Journal of materials in civil engineering**, v. 9, n. 3, p. 154-158, 1997.

MANCILLA, R. C. Vibrações Não Lineares e Estabilidade de Barras Esbeltas de Seção Aberta. 2014. 135 f. Dissertação (Mestrado em Engenharia Civil) - Departamento de Engenharia Civil, Pontifícia Universidade Católica do Rio de Janeiro, Rio de Janeiro, 2014.

MANCILLA, R. C.; GONÇALVES, P. B.; CARVALHO, E. C. Non-linear dynamics analysis and stability of thin-walled beams with monosymetric channel-section. In: ICASS 2015 **Eighth International Conference on Advanced in Steel Structures**, Lisbon, 2015.

MAZZILLI, C. E.; GONÇALVES, P. B.; FRANZINI, G. R. Reduced-order modelling based on non-linear modes. **International Journal of Mechanical Sciences**, v. 214, p. 106915, 2022.

MESACASA, E. et al. Mode interaction in thin-walled equal-leg angle columns. **Thin-Walled Structures**, v. 81, p. 138-149, 2014.

MINCHENKOV, K. et al. Thermoplastic Pultrusion: A Review. **Polymers**, v. 13, n. 2, 180, 2021.

MITURA, A. et al. Experimental nonlinear dynamic regimes for energy harvesting from cantilever bistable shells. **Mechanical Systems and Signal Processing**, v. 206, p. 110890, 2024.

MOHRI, F.; AZRAR, L.; POTIER-FERRY, M. Flexural-torsional post-buckling analysis of thinwalled elements with open sections. **Thin-Walled Structures**, v. 39, n. 11, p. 907-938, 2001.

MONTEIRO, A. C.; MALITE, M. Behavior and design of concentric and eccentrically loaded pultruded GFRP angle columns. **Thin-Walled Structures**, v. 161, p. 107428, 2021.

MUSMAR, M. A. Structural performance of steel plates. **Frontiers in Built Environment**, v. 8, p. 991061, 2022.

NAYFEH, A. H.; MOOK, D. T. **Nonlinear oscillations**. John Wiley & Sons, 2008.

NGUYEN, V. V.; HANCOCK, G. J.; PHAM, C. H. Development of the Thin-Wall-2 Program for buckling analysis of thin-walled sections under generalised loading. International Conference on Advances in Steel Structures, 8, 2015, Lisboa, Portugal. **Proceedings** [...]. Lisboa: ICASS, 2015.

PARKER, T. S.; CHUA, L. **Practical numerical algorithms for chaotic systems**. Springer Science & Business Media, 2012.

PAVLOVIĆ, R. et al. Dynamic stability of a thin-walled beam subjected to axial loads and end moments. **Journal of Sound and Vibration**, v. 301, n. 3-5, p. 690-700, 2007.

PHAM, N. H.; PHAM, C. H.; RASMUSSEN, K. J. Global buckling capacity of cold-rolled aluminium alloy channel section beams. **Journal of Constructional Steel Research**, v. 179, p. 106521, 2021.

PICCARDO, G.; FERRAROTTI, A.; LUONGO, A. Nonlinear generalized beam theory for open thin-walled members. **Mathematics and Mechanics of Solids**, v. 22, n. 10, p. 1907-1921, 2017.

PIGNATARO M.; RIZZI N.; LUONGO A. **Stability, Bifurcation, and Postcritical Behaviour of Elastic Structures**, Elsevier, Amsterdam, 1991.

PROKIĆ, A. Effect of bracing on linear free vibration characteristics of thin-walled beams with open cross section. **Journal of engineering mechanics**, v. 136, n. 3, p. 282-289, 2010.

QIAO, P.; DAVALOS, J. F.; WANG, J. Local buckling of composite FRP shapes by discrete plate analysis. **Journal of Structural Engineering**, v. 127, n. 3, p. 245-255, 2001.

RASMUSSEN, K. J. R.; HANCOCK, G. J. Geometric imperfections in plated structures subject to interaction between buckling modes. **Thin-walled structures**, v. 6, n. 6, p. 433-452, 1988.

RIBEIRO, J. L. P.; GREGORI, M. L.; PARDINI, L. C. Predição das propriedades elásticas de compósitos termoestruturais com reforço multidirecional. **Matéria (Rio de Janeiro)**, v. 13, n. 1, p. 33-48, 2008.

ROZYLO, P. et al. Experimental and numerical study of the buckling of composite profiles with open cross section under axial compression. **Applied Composite Materials**, v. 24, p. 1251-1264, 2017.

SARQUIS, F. R. et al. Experimental and numerical investigation of hot-rolled stainless steel equal leg angles under compression. **Thin-Walled Structures**, v. 151, p. 106742, 2020.

SCHAFER, B. W. CUFSM 5.04 - Cross-Section Elastic Buckling Analysis: constrained and unconstrained finite strip method, 2020. Available at: https://www.ce.jhu.edu/cufsm/downloads/

SCHARDT, R. Generalized beam theory - an adequate method for coupled stability problems. **Thin-walled structures**, v. 19, n. 2-4, p. 161-180, 1994.

SEYDEL, R. **From Equilibrium to Chaos. Practical Bifurcation and Stability Analysis**. New York etc., 1988. 367 p.

SHIFFERAW, Y.; SCHAFER, B. W. Cold-formed steel lipped and plain angle columns with fixed ends. **Thin-Walled Structure**, v. 80, p. 142-152, 2014.

SILVA, N. M. F.; SILVESTRE, N.; CAMOTIM, D. GBT formulation to analyse the buckling behaviour of FRP composite open-section thin-walled columns. **Composite Structures**, v. 93, n. 1, p. 79-92, 2010.

SILVESTRE, N.; CAMOTIM, D. First-order generalised beam theory for arbitrary orthotropic materials. **Thin-Walled Structures**, v. 40, n. 9, p. 755-789, 2002a.

SILVESTRE, N.; CAMOTIM, D. Second-order generalised beam theory for arbitrary orthotropic materials. **Thin-Walled Structures**, v. 40, n. 9, p. 791-820, 2002b.

SIMULIA. **Abaqus Documentations**. Dassault Systems, 2024.

SIRAJUDEEN, R. S.; SEKAR, R. Buckling analysis of pultruded glass fiber reinforced polymer (GFRP) angle sections. **Polymers**, v. 12, n. 11, p. 2532, 2020.

SIRQUEIRA, A. S. et al. Experimental assessment of stainless steel hot-rolled equal legs angles in compression. **Journal of Constructional Steel Research**, v. 169, p. 106069, 2020.

SLATER, J. E. **Aeroelastic instability of a structural angle section**. Doctoral dissertation, University of British Columbia, 1969.

SUGIYAMA, Y.; LANGTHJEM, M. A.; KATAYAMA, K. Parametric Resonances of Columns with Damping. **Dynamic Stability of Columns under Nonconservative Forces**: Theory and Experiment, p. 199-206, 2019.

SUN, Y. et al. Experimental and numerical investigations of hotrolled austenitic stainless steel equal-leg angle sections. **Thin-Walled Structures**, v. 144, p. 106225, 2019.

SZAK, P. J. et al. The clear creek hybrid composite I-girder pedestrian bridge. **Journal of Composites for Construction**, v. 3, n. 2, p. 101-104, 1999.

TETER, A. Dynamic, multimode buckling of thin-walled columns subjected to in-plane pulse loading. **International Journal of Non-Linear Mechanics**, v. 45, n. 3, p. 207-218, 2010.

TESCHL, G. **Ordinary differential equations and dynamical systems**. American Mathematical Soc, 2012.

THOMPSON, J. M. T.; STEWART, H. B. **Nonlinear Dynamics and Chaos**. John Wiley and Sons, Hoboken, 2002.

TRAHAIR, N. S. **Flexural-torsional buckling of structures**. London: Chapman and Hall, 1993.

THUMRONGVUT, J.; PAKWAN, N.; KRATHUMKLANG, S. Flexural-Torsional Buckling of Pultruded Fiber-Reinforced Polymer Angle Beams under Eccentric Loading. **Materials Science Forum**, v. 982, p. 201-206, 2020.

THOMPSON, J. M. T.; HUNT, G. W. **A General Theory of Elastic Stability**. Wiley, London, 1973.

THOMPSON, J. M. T. Dynamical integrity: three decades of progress from macro to nanomechanics. In **Global Nonlinear Dynamics for Engineering Design and System Safety**, v. 588, p. 1-26. Springer International Publishing, 2019.

URBANIAK, M.; TETER, A; KUBIAK, T. Influence of boundary conditions on the critical and failure load in the GFPR channel cross-section columns subjected to compression. **Composite Structures**, v. 134, p. 199-208, 2015.

VAYAS, I. et al. Telecommunication and transmission lattice towers from angle sections-the ANGELHY project. **Ce/Papers**, v. 4, n. 2-4, p. 210-217, 2021.

VEDERNIKOV, A. et al. Pultruded materials and structures: A review. **Journal of Composite Materials**, v. 54, n. 26, p. 4081-4117, 2020.

VLASOV, V. **Thin-walled elastic beams**. (2nd ed.). Israel Program for Scientific Translations, Jerusalem, 1963.

VOLK, M. et al. Costefficient, automated, and sustainable composite profile manufacture: A review of the state of the art, innovations, and future of pultrusion technologies. **Composites Part B**, v. 246, p. 110135, 2022.

WANG, B. et al. Free vibration analysis of beam-type structures based on novel reduced-order model. **AIAA Journal**, v. 55, n. 9, p. 1-10, 2017.

WANG, C. M.; REDDY, J. N.; LEE, K. H. **Shear deformable beams and plates**: Relationships with classical solutions. 1. ed. Elsevier, 2000. 312 p.

WEI, X. et al. Measured dynamic properties for FRP footbridges and their critical comparison against structures made of conventional construction materials. **Composite Structures**, v. 223, p. 110956, 2019.

XIE, W. C. **Dynamic stability of structures**. Cambridge University Press, 2006.

YADAV, A.; PANDA, S. K.; DEY, T. Non-linear dynamic instability analysis of mono-symmetric thin walled columns with various boundary conditions. **International Journal of Mechanical Sciences**, v. 126, p. 242-254, 2017.

ZHANG, Y. et al. Study of flexural-torsional buckling behaviour of 6061-T6 aluminium alloy unequal-leg angle columns. **Thin-Walled Structures**, v. 164, p. 107821, 2021.

ZHANG, L.; LIANG, Y.; ZHAO, O. Laboratory testing and numerical modelling of pin-ended hot-rolled stainless steel angle section columns failing by flexural-torsional buckling. **Thin-Walled Structures**, v. 161, p. 107395, 2021.